

# The Distribution of Thermal Pressures in the Diffuse, Cold Neutral Medium of our Galaxy. II. An Expanded Survey of Interstellar C I Fine-Structure Excitations

Edward B. Jenkins  
*Princeton University Observatory*  
*Princeton, NJ 08544-1001*  
 ebj@astro.princeton.edu  
 and

Todd M. Tripp  
*Department of Astronomy*  
*University of Massachusetts*  
*710 North Pleasant Street*  
*Amherst, MA 01003-9305*  
 tripp@astro.umass.edu

## ABSTRACT

We analyzed absorption features arising from interstellar neutral carbon that appeared in the UV spectra of 89 stars recorded in the highest resolution echelle modes of the *Space Telescope Imaging Spectrograph* on *HST* so that we could determine the relative populations of collisionally excited fine-structure levels in the atom's electronic ground state. From this information, in combination with molecular hydrogen rotation temperatures, we derive the distribution of thermal pressures in the diffuse, cold neutral medium. We find a lognormal pressure distribution (weighted by mass) with a mean in  $\log(p/k)$  equal to 3.58 and an rms dispersion of at least 0.175 dex that plausibly arises from turbulence with a characteristic Mach number in the range  $1 < M < 4$ . The extreme tails in the distribution are above the lognormal function however. Overall, pressures are well correlated with local starlight intensities and extreme kinematics, and they show some anticorrelation with kinetic temperatures. A subsample restricted to low ambient UV intensities reveals a mode in the distribution of  $\log(p/k)$  that is nearly the same as the complete sample, but with a strong negative skewness created by a near absence of a tail at high pressures. Approximately 23% of this gas is at a pressure that is below that allowed for a static cold neutral medium. Accompanying nearly all of the gas is a small fraction ( $\sim 0.05\%$ ) that has an extraordinarily large pressure,  $\log(p/k) > 5.5$ , and this condition is more prevalent at high velocities or for regions with enhanced starlight densities. This survey suggests that the dispersion of thermal pressures in the cold, neutral ISM is predominantly governed by microscopic turbulence driven by star-forming regions, with some additional effects from macroscopic events (e.g., SN explosions), and these measurements provide constraints for future studies of the broader impact of turbulence on the ISM and star formation.

*Subject headings:* ISM: atoms – ISM: kinematics and dynamics – ISM: lines and bands – techniques: spectroscopic – turbulence – ultraviolet: ISM

## 1. Introduction

In his commentary on the classic paper by Chandrasekhar & Münch (1952) on brightness fluctuations in the Milky Way, Scalo (1999) presented an insightful discussion of a dichotomy in our perception of the structure of the diffuse interstellar medium (ISM) of our Galaxy. On the one hand, we might view the ISM in terms of a collection of isolated, dense clouds enveloped in a more tenuous medium, a concept that has directed our thinking on the establishment of discrete “phases” of the ISM with well established spatial domains and vastly different properties that can be justified on some fundamental physical grounds (Field et al. 1969; McKee & Ostriker 1977; Burkert & Lin 2000; Vázquez-Semadeni et al. 2000; Brandenburg et al. 2007). On the other hand, much of the ISM can be viewed as a continuous fluid medium containing a texture of seemingly random fluctuations in density, velocity and temperature. Adherents to this second picture [e.g., Ballesteros-Paredes et al. (1999)] view clouds as an illusion created by the most extreme fluctuations in a turbulent medium having an extraordinarily high Reynolds number. While this is undoubtedly true, we must also acknowledge the presence of nearly static, sharp boundaries between different media, as revealed by dark clouds with well defined edges that have been sculpted by ionization, dissociation, and evaporation/condensation fronts. Both pictures have their utility in exploring important issues on the multitude of processes that can occur within the ISM.

As we switch our perspective from morphological to dynamical properties of the ISM, we find that over macroscopic scales the motions of gases in our Galaxy can be governed by the injection and dissipation of mechanical energy from a wide range of energy sources that include supernova explosions (McKee & Ostriker 1977; McCray & Snow 1979; Mac Low et al. 1989; Kim et al. 2001; de Avillez & Breitschwerdt 2005a), disturbances from newly formed H II regions (Lasker 1967; Tenorio-Tagle 1979; Rodríguez-Gaspar & Tenorio-Tagle 1998; Peters et al. 2008), stellar mass loss (Abbott 1982; McKee et al. 1984; Owocki 1999), infalling gas clouds from the Galactic halo (Wakker & van Woerden 1997; Santillán et al. 1999, 2007), bipolar jets from star forming regions (Bally 2007),

shocks in spiral arm density waves (Roberts et al. 1975), and the magnetorotational instability driven by differential galactic rotation (Pinotek & Ostriker 2004). These processes play a strong role in creating recognizable, discrete structures and flows of material in the ISM, but ultimately some of the energy from the resulting compressions and vorticity will also be transformed into random turbulent motions. Transient structures of small sizes can arise from the cascade of larger turbulent cells into small ones or be created in the interface regions between colliding gas flows (Audit & Hennebelle 2005). Turbulence can also be fed by instabilities in phase transition layers (Inoue et al. 2006) or the weak driving forces that arise from the thermal instability of the ISM (Kritsuk & Norman 2002b; Koyama & Inutsuka 2006), the latter of which can be sustained by abrupt changes in the heating rate from UV radiation (Kritsuk & Norman 2002a).

Over the past several decades, much progress has been made in the study of magnetohydrodynamical (MHD) turbulence in the ISM. Our understanding of this phenomenon has been facilitated by the rapid emergence of powerful 3-dimensional computer simulations, and its existence is supported by observations of column density distributions, velocity statistics, cloud morphologies, deviations in magnetic fields, and various kinds of disturbances in the propagation of radio waves in ionized media [for a review, see Elmegreen & Scalo (2004)]. This phenomenon is influential on the heating, chemical mixing, radio wave propagation, and cosmic ray scattering in the ISM (Scalo & Elmegreen 2004). Within denser environments, turbulent processes are expected to have a strong influence on the fragmentation of density concentrations just before and during the earliest stages of gravitational collapse that leads to star formation (Mac Low & Klessen 2004; McKee & Ostriker 2007).

Both the coherent dynamical phenomena and the smaller scale turbulent motions have an influence on pressures in the ISM. These pressures appear in many forms: thermal, magnetic, dynamical, and the indirect effects of cosmic rays, and their collective magnitude amounts to about  $p/k = 2.5 \times 10^4 \text{cm}^{-3} \text{K}^1$  that is established by

---

<sup>1</sup>Throughout this paper, we quantify pressures in terms of

the hydrostatic equilibrium of gaseous material in the gravitational potential of the Galactic plane (Boulares & Cox 1990). Except for very hot media ( $T > 10^5$  K) that have been created by shock heating from supernova blast waves (Cox & Smith 1974; de Avillez & Breitschwerdt 2005b) or that reside within wind-blown bubbles around stars (Castor et al. 1975; Weaver et al. 1977), the thermal pressures of the ISM represent a small fraction (about one-tenth for  $T \sim 100$  K) of the total pressure (de Avillez & Breitschwerdt 2005a). While thermal pressures and their variability may seem unimportant in the dynamical development of the general ISM, they nevertheless can be influenced by stochastic dynamical effects and thus can provide us with useful information.

In this paper, we make use of the fact that the two upper fine-structure levels in the electronic ground state of the neutral carbon atom, with excitation energies  $E/k = 23.6$  and  $62.4$  K, are easily excited and de-excited by collisions with neutral and charged particles at typical densities and temperatures within the diffuse, cold gas in the Galactic plane. The balance between the effects of these collisions and spontaneous radiative decays (at wavelengths 609 and  $371 \mu\text{m}$ ) establishes fine-structure level population ratios that can serve as an indicator of the local density and temperature of the C I-bearing material. We sense these population ratios by observing the UV multiplets of C I that appear as foreground absorption features in the spectra of hot stars recorded at high spectral resolution.

The first widespread study of C I fine-structure excitations was carried out by Jenkins & Shaya (1979), who analyzed observations that came from the UV spectrograph on the *Copernicus* satellite. Those observations and a more comprehensive survey by Jenkins et al. (1983) were primitive by today's standards for observing C I features set by spectrographs on the *Hubble Space Telescope* (*HST*) (Smith et al. 1991; Jenkins et al. 1998; Jenkins 2002), but they nevertheless established an early framework for determining the average thermal pressures in the ISM and their variations from one location to the next. In addition to

---

$p/k$  in the units  $\text{cm}^{-3}$  K instead of simply  $p$  in the units of  $\text{dyne cm}^{-2}$  or  $\text{erg cm}^{-3}$ . Our representation facilitates comparisons with actual densities and temperatures in the ISM.

these general surveys, special studies sensed extreme positive deviations in pressure from the C I features in spectra of stars within and behind the Vela supernova remnant (Jenkins et al. 1981, 1984, 1998; Jenkins & Wallerstein 1995; Wallerstein et al. 1995; Nichols & Slavin 2004), indicating that the blast wave overtook and compressed<sup>2</sup> small clouds in the medium that surrounded the explosion site (Chevalier 1977).

A new advance in the study of C I excitation in the general ISM arose from the study by Jenkins & Tripp (2001) (hereafter JT01), who used the highest resolution configurations of the echelle spectrograph in the *Space Telescope Imaging Spectrograph* (STIS) (Kimble et al. 1998; Woodgate et al. 1998) to observe C I in the spectra of 21 stars. An important breakthrough in this work was to make use of the ability of STIS to record many different C I multiplets simultaneously, which allowed JT01 to benefit from a special analysis technique that they developed to unravel the blended absorption profiles arising from the three fine-structure levels.

The current study of thermal pressures expands on the work of JT01, once again using the analysis method employed earlier, but with some technical improvements outlined in Appendix A. In §2 we describe our new coverage of sightlines that significantly expands on the limited selection of stars that were studied by JT01, but we caution that one must be aware of a few, mostly unavoidable, selection biases in the sampling. In §3 we review the basic principles of the analysis, but leave it to the reader to consult JT01 for a more detailed description of the mathematical method. This section also introduces our fundamental approach to interpreting the population ratios in terms of the local density and temperature of the C I-bearing gas, a method originally developed by Jenkins & Shaya (1979). Table 2 in this section lists the 89 target stars whose spectra were analyzed in this study, along with some relevant information about the foreground regions probed by the sightlines. For each sightline, we show in Table 3 some composite interstellar conditions that we derived and some reflections on their significance in §7. In Table 4 we provide more detailed, machine-readable

---

<sup>2</sup>We note that Nichols & Slavin (2004) proposed some possible alternative explanations for producing an excess of excited C I.

information for each velocity bin in the entire survey. Section 4 describes a number of additional factors that require some consideration when the C I results are interpreted, including ways to estimate the total amount of gas that accompanies the C I (§4.1), the kinetic temperature of the gas (§4.2), the mix of particles that can excite the upper levels (§4.3), and the local intensity of starlight (§4.4). The starlight intensity must be known in order to correct for optical pumping of the fine-structure levels (as described in §6), and, as we demonstrate in §9.1, such intensities seem to be correlated with pressure.

Section 5 discusses how we interpret our finding that virtually all of the measurements do not agree with the expected fine-structure populations for collisional excitation for any uniform values of local density or temperature. Here, we introduce the idea that small admixtures of gas at extraordinarily high pressures accompany virtually all of the gas at normal pressures, and in §10.5.1 we examine (and ultimately reject) some alternative explanations of the observed deviations. Some discussions on the implications and possible origins of the high pressure component appear in §§10.5.2–10.5.4, and we show in §8 and §10.5.4 that the gas fractions at high pressures are accentuated in material that is moving rapidly or is exposed to a high intensity of starlight.

In §9 we derive the distribution function for the mass-weighted thermal pressures in the dominant low pressure regime for two samples: (1) all of the gas and (2) gas that is well removed from intense sources of UV radiation. For the convenience of those who wish to compare our results with computer simulations of turbulence based on volume-weighted distributions, we convert our mass-weighted sampling to a volume-weighted one in §9.2, but with the precarious assumption that the gas responds to pressure perturbations with a single polytropic index  $\gamma$  (which is left as a free parameter). In §9.3, we address the possibility that the width of the pressure distribution understates the true dispersion of pressures in the ISM, due to the fact that we view in each velocity bin the superposition of absorptions by gases with different pressures and thus only sense an average pressure in each case. In §10.1.3 we derive a range of possible characteristic turbulent Mach numbers for the C I-bearing gas

We explore in §10.2 some time constants for various physical processes that are relevant to our work. For instance, the excitation temperatures of the two lowest rotational levels of  $\text{H}_2$  play a role in many of our pressure determinations. In §10.3 we find that only on scales of order 100–1000 AU are lag times of any importance in weakening the coupling of  $\text{H}_2$  rotation temperatures to the local kinetic temperature. The same applies to the equilibrium between heating and cooling of the gas: compressions and decompressions of the gas should follow the equilibrium relationship except on the smallest scales where the behavior becomes more adiabatic in nature. The time scales for the equilibria of fine-structure populations and the balance between C I and C II are quite short and hence apply on all of the relevant size scales.

In a brief departure from the discussion of turbulence as a source of pressure deviations, we consider in §10.4 the possibility that the upper end of our pressure distribution function is consistent with random interceptions of supernova remnants in different stages of development. Finally, we summarize our conclusions in §11.

## 2. Observations

Our earlier survey (JT01) covered only 21 stars that were observed with the guaranteed observing time granted to the STIS instrument definition team. In order to maximize the observing efficiency, the target stars in this study were located within two Galactic longitude intervals, ones where the *HST* continuous viewing zones<sup>3</sup> intersected the Galactic plane ( $99^\circ < \ell < 138^\circ$ ,  $254^\circ < \ell < 313^\circ$ ). Many additional observations, most of which were performed after the study by JT01, were more broadly distributed in the sky and were taken before the 5-year hiatus of observing brought about by STIS instrument failure in August 2004. We downloaded from MAST (Multi-mission Archive at the Space Telescope Science Institute) virtually all of the observations performed at wavelengths that covered two or more C I transitions in the E140H and E230H modes. Once

<sup>3</sup>The continuous viewing zones (CVZs) are two declination bands centered on  $\delta = \pm 61^\circ 5'$  where observations can be performed with high efficiency because the targets are not occulted by the Earth as the satellite progresses along its orbit.

again, we made use of the broad wavelength coverage of STIS to examine as many multiplets as possible. These spectra had a resolving power in radial velocity equal to  $2.6 \text{ km s}^{-1}$  (or  $1.5 \text{ km s}^{-1}$  for the stars observed by JT01 because a narrower entrance slit was used) (Proffitt et al. 2010). Prominent among these observations were those performed by a SNAP (snapshot) program conducted by J. T. Lauroesch (program nr. 8241) in 1999 and 2000. In the current new study, we have also reanalyzed the data presented by JT01 because we have now adopted some new, more refined analysis procedures (see Appendix A). All of the data were processed in the manner described by JT01, except that for observations outside their survey we did not need to implement an intensity rebalancing between MAMA half pixels (see their §4.2 for details), since these half pixel intensities were binned together beforehand.

A small fraction of the observations had to be rejected because either (1) there was an insufficient amount of C I present to perform a meaningful analysis with the signal-to-noise ratio at hand, or (2) the projected rotational velocity of the star was so low that stellar features interfered with the interstellar ones or made the continua too difficult to model. These unsuitable sight lines are identified by their target star names in Table 1. We also rejected the central stars of planetary nebulae, since the interstellar components could be contaminated by contributions from gas in the nebular shell.

Initially, we had considered using observations recorded at lower resolution with the E140M mode of STIS to broaden the selection of targets, but a comparison of the results for a few stars that were also observed with the E140H mode indicated that unreliable results emerged from the lower resolution data as a result of improper treatments of unresolved, saturated profiles. (The correction scheme developed by Jenkins (1996) could not be used because various lines overlap each other, and the optical depths must go through a complicated transformation to obtain unique answers for the column densities of the three fine-structure levels, as described in §5.2.1 of JT01.)

Table 2 presents the information on the 89 sightlines included in the present study. They

Table 1: Rejected Sightlines

Insufficient C I	Stellar Line Confusion
BD+25D2534	CPD−64D481
BD−03D2179	HD 1909
HD 1999	HD 3175
HD 6456	HD 30122
HD 6457	HD 37367
HD 23873	HD 43819
HD 32039	HD 44743
HD 64109	HD 52329
HD 79931	HD 62714
HD 86360	HD 93237
HD 92536	HD 94144
HD 164340	HD 106943
HD 192273	HD 108610
HD 195455	HD 175756
HD 196867	
HD 201908	
HD 233622	

span path lengths that range from about 0.2 kpc to 6 kpc and have a median length of 1.9 kpc. We processed all of the data that we felt were acceptable, according to the principles outlined in the above two paragraphs. We made 2416 separate measurements, but since we oversampled the wavelength resolution of the spectrograph by a factor of 5.3, our determinations actually represent only about 460 independent samples in radial velocity.

We refrained from applying any special selection criteria to make our sampling of regions more evenhanded. For this reason, one must be aware of certain selection biases in the composite information presented in §3 below. The following are some noteworthy considerations about our sample:

1. All sightlines terminate at the location of a bright, early-type star. Thus, it is inevitable that we will be probing an environment near such a star, or in fact a location near a grouping of many such stars, since they tend to be strongly clustered in space. In a number of cases, strong elevations in thermal pressures seen in certain radial velocity channels probably arise from either the effects of stellar winds or rapidly expanding H II regions. As we will show in §9.1, a large portion of the C I that we observe re-

sides in regions with much higher than normal densities of starlight radiation. This is probably a consequence of the fact that the observations are biased toward a sampling of the progenitorial cloud complexes out of which the stars had formed.

2. Regions where the density is low enough (or the local temperature or radiation density high enough) to shift the ionization equilibrium of carbon atoms more strongly than usual to its ionized form are missed in our sample. As we show in Figure 1, practically all of what is classically known as the warm neutral medium (WNM, with  $T \sim 9000$  K) is invisible to us; our survey is restricted to the phase called the cold neutral medium (CNM, with  $T \sim 80$  K), with possibly some very limited sensitivity to gas in the thermally unstable intermediate temperatures. In addition, there are situations where C I is detected at certain velocities, but the quality of the data is insufficient to measure reliably the thermal pressures, as we discuss in some detail in §A.2. Hence, such regions are excluded.
3. Regions of moderate size that are very dense will have enough extinction in the UV to make stars behind them too faint to observe. This effect will result in our missing clouds that happen to be strongly compressed by turbulence or gravity. It is clear from the results shown in Column 5 of Table 2 that a cutoff of our sample corresponds to a  $B - V$  color excess of about 0.5, which in turn translates approximately to  $N(\text{H}) = 3 \times 10^{21} \text{cm}^{-2}$  if we use the standard relation between  $E(B - V)$  and  $N(\text{H})$  in the ISM (Bohlin et al. 1978; Rachford et al. 2009). Also, portions of some of our strongest C I absorption profiles were rejected from consideration because we sensed that they had velocity substructures that were saturated and not resolved by the instrument.
4. Stars in certain programs were selected by observers because they had interesting properties. Of special relevance to our thermal pressure outcomes would be the observations that were designed to probe regions that were known to be either disturbed (e.g., showing high velocity gas) or at higher

than normal densities (e.g., showing unusually strong molecular absorptions). Often, one can sense the characters of such selections by reading the abstracts of the programs that made the observations.<sup>4</sup>

---

<sup>4</sup>The archive root names listed in Column 9 of Table 2 can be used as a guide on the MAST *HST* search web page to find the Proposal ID and its abstract.

TABLE 2  
PROPERTIES OF THE SIGHTLINES

Target Star (1)	Galactic Coordinates (deg.)		Spectral Type (4)	$E(B - V)^a$ (5)	Distance <sup>a</sup> (kpc) (6)	$H_2 T_{01}^b$		Archive Exposure Root Name(s) (9)
	$\ell$ (2)	$b$ (3)				(K) (7)	Ref. <sup>c</sup> (8)	
CPD-59° 2603	287.590	-0.687	O5 V((f))	0.36	3.5	77	6	O40P01D6Q O4QX03010-30
HD 108	117.928	1.250	O6pe	0.42	3.8	...		O5LH01010-80
HD 1383	119.019	-0.893	B1 II	0.37	2.9	...		O5C07C010
HD 3827	120.788	-23.226	B0.7 Vn	0.05	1.8	...		O54309010-30 O54359010-30
HD 15137	137.462	-7.577	O9.5 II-III <sub>n</sub>	0.24	3.5	104	7	O5LH02010-80
HD 23478	160.765	-17.418	B3 IV	0.20	0.47	55	7	O6LJ01020
HD 24190	160.389	-15.184	B2 V <sub>n</sub>	0.23	0.82	66	7	O6LJ02020
HD 24534 (X Per)	163.083	-17.137	O9.5 III	0.31	2.1	57	6	O66P02010 O64813010-20 O66P01010-20
HD 27778 (62 Tau)	172.764	-17.393	B3 V	0.34	0.23	55	2	O59S01010-20
HD 32040	196.071	-22.605	B9 V <sub>n</sub>	0.00	0.16	...		O56L04010-30 O8MM02010-30
HD 36408	188.498	-8.885	B7 IV	0.11	0.19	...		O8MM04020-30
HD 37021 ( $\theta^1$ Ori B)	209.007	-19.384	B3 V	0.42	0.56	...		O59S02010
HD 37061 ( $\nu$ Ori)	208.926	-19.274	B0.5 V	0.44	0.64	...		O59S03010
HD 37903	206.853	-16.538	B1.5 V	0.29	0.83	68	8	O59S04010
HD 40893	180.086	4.336	B0 IV	0.31	3.1	78	8	O8NA02010-20
HD 43818 (11 Gem)	188.489	3.874	B0 II	0.45	1.9	...		O5C07I010
HD 44173	199.002	-1.316	B5 III	0.05	0.52	...		O5C020010
HD 52266	219.133	-0.680	O9.5 IV <sub>n</sub>	0.22	1.8	...		O5C027010
HD 69106	254.519	-1.331	B0.5 IV <sub>nn</sub>	0.14	1.5	80	10	O5LH03010-50
HD 71634	273.326	-11.524	B7 IV	0.09	0.32	...		O5C090010
HD 72754 (FY Vel)	266.828	-5.815	B2 I:pe	0.31	3.9	...		O5C03E010
HD 75309	265.857	-1.900	B1 II <sub>p</sub>	0.18	2.9	65	3	O5C05B010
HD 79186 (GX Vel)	267.366	2.252	B5 Ia	0.23	1.9	...		O5C092010
HD 88115	285.317	-5.530	B1.5 II <sub>n</sub>	0.12	3.7	145	3	O54305010-60
HD 91824	285.698	0.067	O7 V	0.22	3.0	61	6	O5C095010
HD 91983	285.877	0.053	B1 III	0.14	3.0	61	7	O5C08N010
HD 93205	287.568	-0.706	O3 Vf+	0.34	3.3	105	6	O4QX01010-40

TABLE 2—*Continued*

Target Star (1)	Galactic Coordinates (deg.)		Spectral Type (4)	$E(B - V)^a$ (5)	Distance <sup>a</sup> (kpc) (6)	$H_2 T_{01}^b$		Archive Exposure Root Name(s) (9)
	$\ell$ (2)	$b$ (3)				(K) (7)	Ref. <sup>c</sup> (8)	
HD 93222	287.738	-1.016	O7 IIIf	0.32	3.6	77	6	O4QX02010-40
HD 93843	288.243	-0.902	O5 IIIf	0.24	3.5	107	10	O5LH04010-40
HD 94454	295.693	-14.725	B8 III	0.19	0.30	74	7	O6LJ0H010
HD 94493	289.016	-1.177	B1 Ib	0.15	3.4	...		O54306010-20
HD 99857	294.779	-4.940	B0.5 Ib	0.27	3.5	83	10	O54301010-60 O54301020 O54301030 O54301040 O54301050 O54301060
HD 99872	296.692	-10.617	B3 V	0.29	0.24	66	7	O6LJ0I020
HD 102065	300.027	-17.996	B2 V	0.28	0.18	59	6	O4O001010-30
HD 103779	296.848	-1.023	B0.5 Iab	0.17	4.3	86	6	O54302010-20
HD 104705 (DF Cru)	297.456	-0.336	B0 Ib	0.17	5.0	92	6	O57R01010, 30
HD 106343 (DL Cru)	298.933	-1.825	B1.5 Ia	0.23	3.3	...		O54310010-20
HD 108002	300.158	-2.482	B2 Ia/Iab	0.18	4.2	77	7	O6LJ08020
HD 108639	300.218	1.950	B0.2 III	0.26	2.4	88	7	O6LJ0A020
HD 109399	301.716	-9.883	B0.7 II	0.19	2.9	...		O54303010-20
HD 111934 (BU Cru)	303.204	2.514	B1.5 Ib	0.32	2.3	...		O5C03N010
HD 112999	304.176	2.176	B6 Vn	0.17	0.45	96	7	O6LJ0C010-20
HD 114886	305.522	-0.826	O9 IIIIn	0.32	1.8	92	7	O6LJ0D020
HD 115071	305.766	0.153	B0.5 Vn	0.40	2.7	71	7	O6LJ0E010-20
HD 115455	306.063	0.216	O7.5 III	0.40	2.6	81	7	O6LJ0F010-20
HD 116781	307.053	-0.065	B0 IIIIne	0.31	2.2	...		O5LH05010-40
HD 116852	304.884	-16.131	O9 III	0.14	4.5	70	6	O5C01C010 O63571010 O8NA03010-20
HD 120086	329.611	57.505	B2 V	0.04	0.99	...		O5LH06010-50
HD 121968	333.976	55.840	B1 V	0.11	3.1	38	6	O57R02010-20
HD 122879	312.264	1.791	B0 Ia	0.29	3.3	90	7	O5C037010 O5LH07010-40 O6LZ57010

∞



TABLE 2—*Continued*

Target Star (1)	Galactic Coordinates (deg.)		Spectral Type (4)	$E(B - V)^a$ (5)	Distance <sup>a</sup> (kpc) (6)	$H_2 T_{01}^b$		Archive Exposure Root Name(s) (9)
	$\ell$ (2)	$b$ (3)				(K) (7)	Ref. <sup>c</sup> (8)	
HD 124314	312.667	-0.425	O6 Vnf	0.43	1.4	74	7	O54307010-20
HD 140037	340.151	18.042	B5 III	0.08	0.77	...		O6LJ04010
HD 142315	348.981	23.300	B9 V	0.10	0.15	...		O5C03Y010
HD 142763	31.616	46.960	B8 III	0.01	0.28	...		O5C040010
HD 144965	339.044	8.418	B2 Vne	0.27	0.51	70	7	O6LJ05010
HD 147683	344.858	10.089	B4 V+B4 V	0.28	0.37	58	7	O6LJ06020
HD 147888 ( $\rho$ Oph D)	353.648	17.710	B3 V	0.42	0.12	44	7	O59S05010
HD 148594	350.930	13.940	B8 Vnn	0.18	0.19	...		O5C04A010
HD 148937	336.368	-0.218	O6.5 I	0.55	2.2	...		O6F301010-20
HD 152590	344.842	1.830	O7 V	0.37	3.6	64	7	O5C08P010 O8NA04010-20
HD 156110	70.996	35.713	B3 Vn	0.03	0.62	...		O5C01K010
HD 157857	12.972	13.311	O6.5 IIIf	0.37	3.1	86	7	O5C04D010
HD 165246	6.400	-1.562	O8 Vn	0.33	1.9	...		O8NA05010-20
HD 175360	12.531	-11.289	B6 III	0.12	0.24	...		O5C047010
HD 177989	17.814	-11.881	B0 III	0.11	6.0	52	6	O57R04010-20 O57R03010-20
HD 185418	53.604	-2.171	B0.5 V	0.38	1.2	105	6	O5C01Q010
HD 192639	74.903	1.479	O7 Ibf	0.56	2.1	98	2	O5C08T010
HD 195965	85.707	4.995	B0 V	0.19	1.1	91	7	O6BG01010-20
HD 198478 (55 Cyg)	85.755	1.490	B3 Ia	0.43	1.3	...		O5C06J010
HD 198781	99.946	12.614	B0.5 V	0.26	0.69	65	7	O5C049010
HD 201345	78.438	-9.544	O9 V	0.14	2.2	147	6	O5C050010 O6359P010
HD 202347	88.225	-2.077	B1.5 V	0.11	0.95	116	3	O5G301010, 40-50
HD 203374	100.514	8.622	B2 Vn	0.43	0.34	87	10	O5LH08010-60
HD 203532	309.461	-31.739	B3 IV	0.24	0.22	49	6	O5C01S010
HD 206267	99.292	3.738	O6.5 V	0.45	0.86	65	2	O5LH09010-40
HD 206773	99.802	3.620	B0 V:nnep	0.39	0.82	94	4	O5C04T010
HD 207198	103.138	6.995	O9.5 Ib-II	0.47	1.3	66	2	O59S06010-20
HD 208440	104.031	6.439	B1 V	0.27	1.1	75	4	O5C06M010
HD 208947	106.550	8.996	B2 V	0.16	0.56	...		O5LH0A010-40

TABLE 2—*Continued*

Target Star (1)	Galactic Coordinates (deg.)		Spectral Type (4)	$E(B - V)^a$ (5)	Distance <sup>a</sup> (kpc) (6)	$H_2 T_{01}^b$		Archive Exposure Root Name(s) (9)
	$\ell$ (2)	$b$ (3)				(K) (7)	Ref. <sup>c</sup> (8)	
HD 209339	104.579	5.869	B0IV	0.24	1.2	90	4	O5LH0B010–40 O6LZ92010
HD 210809	99.849	−3.130	O9Iab	0.28	4.3	87	7	O5C01V010
HD 210839 ( $\lambda$ Cep)	103.829	2.611	O6Infp	0.49	1.1	72	2	O54304010–20
HD 212791	101.644	−4.303	B3ne	0.18	0.62	...		O5C04Q010
HD 218915	108.064	−6.893	O9.5Iabe	0.21	5.0	86	6	O57R05010, 30
HD 219188	83.031	−50.172	B0.5IIIIn	0.09	2.1	103	1	O6E701010 O8DP01010 O8SW01010
HD 220057	112.131	0.210	B3IV	0.17	0.77	65	7	O5C01X010
HD 224151	115.438	−4.644	B0.5II–III	0.34	1.3	252	10	O54308010–20
HDE 232522	130.701	−6.715	B1II	0.14	6.1	...		O5C08J010
HDE 303308	287.595	−0.613	O3Vf	0.33	3.8	86	6	O4QX04010–40

<sup>a</sup> $B - V$  color excesses and distances to the stars were either taken from listings of the same stars in Bowen et al (2008) or Jenkins (2009), or else they were computed by using the same procedures that they invoked.

<sup>b</sup>The molecular hydrogen rotational temperature from  $J = 0$  to 1 that was adopted as an indicator for the kinetic temperature of the intervening gas.

<sup>c</sup>Reference for the source of the  $T_{01}$  value given in the previous column: (1) Savage et al. (1977); (2) Rachford et al. (2002); (3) André et al. (2003); (4) Pan et al. (2005); (5) Lee et al. (2007); (6) Burgh et al. (2007); (7) Sheffer et al. (2008); (8) Rachford et al. (2009); (9) Burgh et al. (2010); (10) “J. M. Shull (2009) in preparation” listed in Burgh et al. (2010); (11) Jensen et al. (2010).

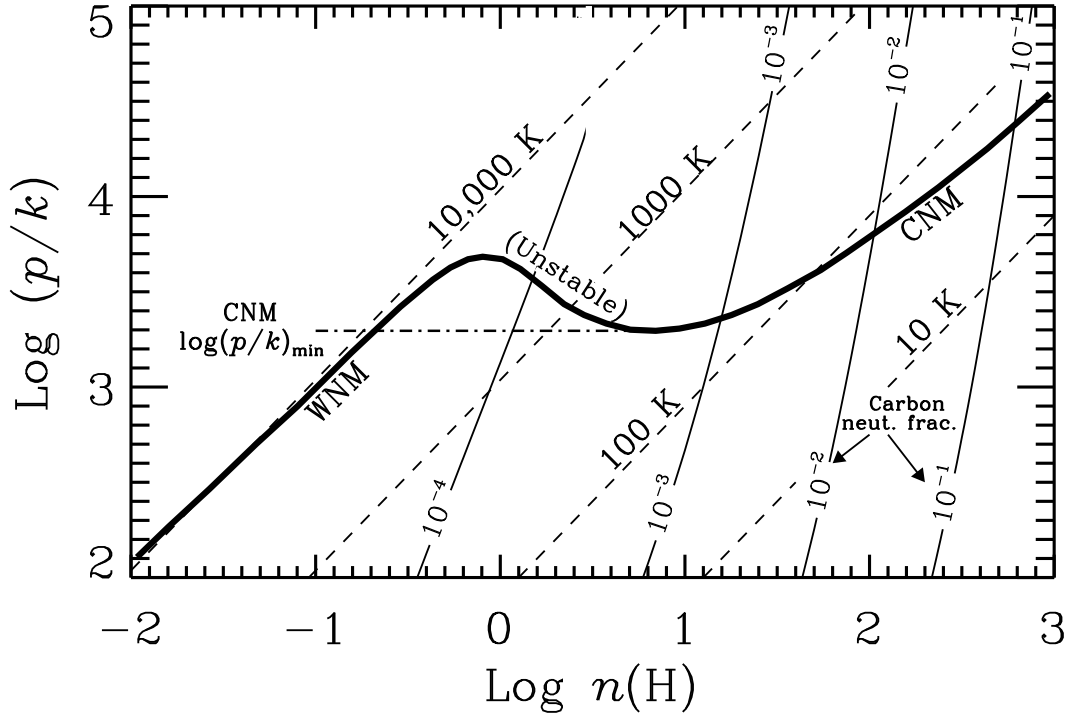


Fig. 1.— A plot of the thermal pressure,  $\log(p/k)$ , vs. the density of hydrogen nuclei,  $\log n(H)$ , showing the locations where heating equals cooling in the ISM near our part of the Galaxy (thick curve), according to the thermal equilibrium calculations by Wolfire et al. (2003) (their “standard model”; see their Fig. 8). Portions of this curve where the slopes are positive are thermally stable and form the distinct phases called the warm neutral medium (WNM) and cold neutral medium (CNM), as indicated. The portion of the curve that has a negative slope has a balance between heating and cooling, but is thermally unstable (Field 1965). In the absence of rapidly changing pressures and densities due to turbulence, the lowest allowable pressure for the CNM is at the horizontal dash dot line labeled “CNM  $\log(p/k)_{\min}$ .” Different temperatures in this diagram are revealed by the straight, dashed lines, constructed using the assumption that  $\text{He}/\text{H}=0.09$  and, for  $T < 1000$  K,  $f(\text{H}_2) = 0.6$  (see §4.3). The thin, gently curved lines show constant values for the expected values of  $\text{C I}_{\text{total}}/(\text{C II} + \text{C I}_{\text{total}})$ , as indicated, according to our equation for ionization equilibrium (see Eq. 1 in §4.4 and the accompanying text), under the assumption that the starlight intensity is equal to the average level  $I_0$  given by Mathis et al. (1983). These curves demonstrate that the WNM is virtually invisible in our survey of C I.

### 3. C I Results

Descriptions of our analysis and the mathematical details of the interpretation of the C I absorption multiplets covered by *HST* were presented by JT01. Except for some enhancements in technique and the use of more up to date atomic data discussed in Appendix A, we have implemented once again the methods of JT01.

Briefly, after we normalized the intensity profiles to an assumed continuum (that usually varies smoothly with wavelength), we converted them to apparent optical depths (Savage & Sembach 1991). For the average spread in radial velocity of the C I in a typical sightline, the individual lines in any given multiplet overlap each other. This introduces confusion in the interpretation of the optical depths. However, we can unravel this confusion by observing different multiplets, because the locations of different transitions with respect to each other change, thus allowing one to resolve ambiguous mixtures of opacities. JT01 devised a way to construct a system of linear equations that could be solved to reveal the apparent column densities  $N(\text{C I})$ ,  $N(\text{C I}^*)$ , and  $N(\text{C I}^{**})$  as a function of velocity.<sup>5</sup> Once this has been done, we can evaluate the quantities  $f1 \equiv N(\text{C I}^*)/N(\text{C I}_{\text{total}})$  and  $f2 \equiv N(\text{C I}^{**})/N(\text{C I}_{\text{total}})$ , which are useful representations of the excitation conditions when we want to understand not only the physical conditions in any given absorbing region, but also possible combinations of contributions from differing regions that overlap each other at a particular velocity.

As explained originally by Jenkins & Shaya (1979) and once again by JT01, the balance of collisional excitations (and de-excitations) against

<sup>5</sup>The notation adopted here is consistent with that of JT01:  $N(\text{C I})$  refers to the column density of atomic carbon in its  $^3P_0$  ground fine-structure state, while  $N(\text{C I}^*)$  and  $N(\text{C I}^{**})$  refer to the column densities of the excited  $^3P_1$  and  $^3P_2$  levels, respectively. The quantity  $N(\text{C I}_{\text{total}})$  equals the sum of the column densities in all three levels. Strictly speaking, we measure *apparent* column densities [ $N_a$  in the notation of Savage & Sembach (1991)], which differ from true column densities because the recorded intensities are smoothed by the instrumental line spread function. In the interest of simplicity, we will refer to such apparent column densities as simply  $N$  and treat them as if they were true column densities. Possible errors in this assumption and our avoidance of cases where they are large are discussed in §A.2.4.

the spontaneous radiative decay of the excited levels establishes an equilibrium value for the level populations that depends on the local density and temperature (and to a much lesser extent, the composition of the gas). As the densities increase at any given temperature, the locations of points on a diagram of  $f1$  vs.  $f2$  trace an upward arching curve (see Fig. 2) that stretches from the origin for low densities to a point at very high densities that approaches a Boltzmann distribution for the levels at the temperature in question.

When the absorptions from two or more regions are superposed at a single velocity, the outcome for  $f1$  and  $f2$  is at the “center of mass” for the values that apply to the individual contributors, with respective weights equal to their values of  $N(\text{C I}_{\text{total}})$ . This outcome is not without some ambiguity, since various combinations of conditions in any ensemble of different clouds can produce the same result. We will address this issue later in §5 when we make a simplifying assumption about such mixtures, and in §9.3 we will discuss the consequences of possible averaging effects that are difficult to recognize. Some additional complexity emerges when one considers the effects of optical pumping by starlight photons, which we will cover in §6.

Figure 2 shows the outcome for all of our measurements of  $(f1, f2)$  at each velocity interval that showed acceptable results, and for every star in the survey. The area of each dot in this diagram is proportional to  $N(\text{C I}_{\text{total}})$ . It is clear that practically all of the points fall above the equilibrium calculations for  $f1$  and  $f2$ , even for a 300 K temperature that is well above the nominal values for the CNM. From this we conclude that either there is always a mixture of two or more regions with vastly differing conditions for every velocity channel or that for some reason(s) the curves are incorrect or inappropriate (we will touch upon this issue later in §10.5.1). A generalized picture of how we interpret some plausible admixtures will be presented in §5.

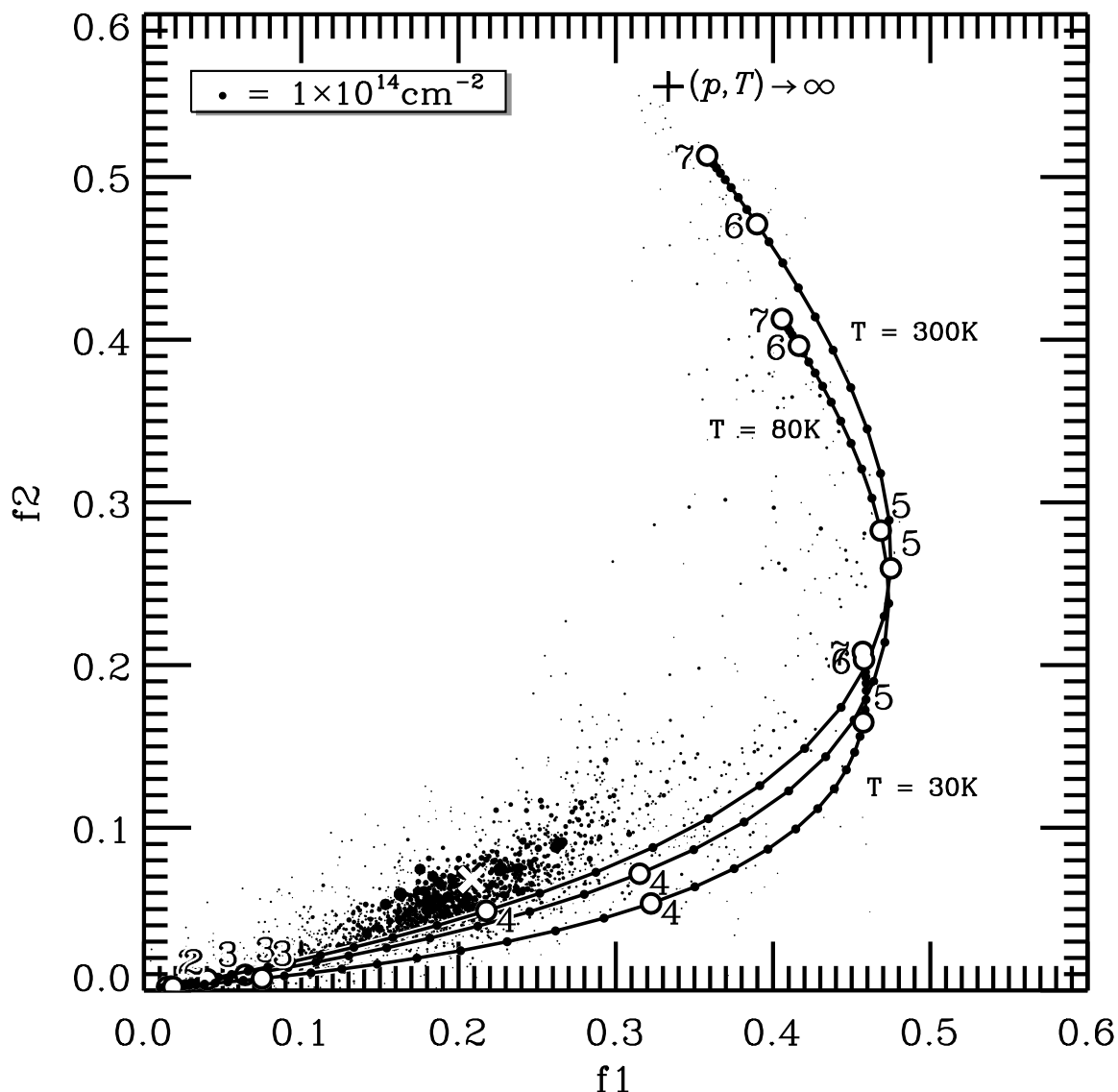


Fig. 2.— Measurements of  $f_1$  and  $f_2$  for all velocity bins, each having a width of  $0.5 \text{ km s}^{-1}$ , for the 89 stars in the survey that had uncertainties  $\sigma(f_1)$  and  $\sigma(f_2)$  less than 0.03. The area of each dot is proportional to the respective value of  $N(\text{C I}_{\text{total}})$ , with a normalization in size as shown in the box at the upper left portion of the plot. The white  $\times$  located at  $f_1 = 0.209$ ,  $f_2 = 0.068$  represents the “center of mass” of all of the dots. The curves indicate the expected level populations for three different temperatures, assuming the gas mixture as specified in §4.3, with different values of  $\log(p/k)$  indicated with dots (adjacent dots represent differences of 0.1 dex). The large open circles on the curves indicate integer values of  $\log(p/k)$  with accompanying numbers to indicate their values. Populations that are proportional to the degeneracies of the levels are indicated by the  $+$  sign labeled “ $(p, T) \rightarrow \infty$ .”

## 4. Properties of the C I-Bearing Gas

### 4.1. Corrections for the Ionization of Carbon

It is important to realize that C I in the gas that we observe is a minor constituent, since the ionization potential of neutral carbon (11.26 eV) is below that of neutral hydrogen (13.6 eV). Most of the carbon atoms in H I regions are singly ionized. The relative proportion of carbon in the neutral form can vary by enormous factors according to the local density of the gas and the strength of the local radiation field that is responsible for ionizing the atoms. As we attempt to derive an even-handed picture of the pressure distribution for the general neutral gas, rather than just a value that is weighted in proportion to the amount of C I that is present, we must devise a means for assessing how much C II accompanies the C I. In essence, we use C II as an indicator for the total amount of the neutral material.

Direct measures of  $N(\text{C II})$  are very difficult to carry out. The only available transition in the wavelength bands covered by our survey is the one at 1334.53 Å. This line is strongly saturated, and the only way to measure  $N(\text{C II})$  with this feature is by sensing the strength of its damping wings (Sofia et al. 2011). However, this measure applies to C II at all velocities, rather than at the velocities where we are able to make use of information from C I. While there exists a very weak intersystem transition at 2325.40 Å, this feature is outside the wavelength coverage of most of our observations and also requires a very high signal-to-noise ratio for a reliable detection (Sofia et al. 2004).

To overcome our inability to measure directly  $N(\text{C II})$  as a function of velocity, we instead used O I as a proxy for C II. The very weak O I intersystem line at 1356 Å is ideal for tracing all but the smallest column densities of material per unit velocity. For velocity intervals over which the C I absorptions could be measured reliably, we found that only on very rare occasions was the O I line too weak to measure. For such instances we had to use the weakest line of S II at 1250 Å as a substitute for O I.<sup>6</sup> For deriving  $N(\text{C II})$ ,

<sup>6</sup> Over very restricted velocity intervals there was an intermediate range of column densities per unit velocity where the O I line was too weak to observe (apparent optical

we assumed that C, O and S were depleted below their respective protosolar abundances (Lodders 2003) by amounts equal to  $-0.162$  dex,  $-0.123$  dex and  $-0.275$  dex, respectively, which corresponds to a moderate depletion strength ( $F_* = 0.5$ ) in the generalized representation of Jenkins (2009). The assumed abundance of O relative to C could be in error by about 0.05 dex if actual the depletion strength is either  $F_* = 0.0$  or 1.0 instead of 0.5. Also, a few new determinations of  $N(\text{C II})$  by Sofia et al. (2011) based on fitting the damping wings of the strong line at 1334.53 Å instead of using the weak intersystem line suggest that the abundances of C in the ISM may be about 0.3 dex lower than stated above, but this change would create a uniform offset that would apply to all of our cases.

One can imagine that some of the C II-bearing gas may be situated in fully ionized regions intersected by our sight lines, especially if most of the ionizing radiation in the ISM is below the ionization potential of singly ionized carbon (24.38 eV). At velocities where we rely on O I as a proxy, we are confident that our estimate for the amount of C II applies only to neutral gas, since H II regions are devoid of O I because the ionizations of O and H are strongly coupled by a charge exchange reaction with a large rate constant (Field & Steigman 1971; Chabaud et al. 1980; Stancil et al. 1999). The same is not true for S II; its behavior should be similar to that of C II (singly ionized S and C have ionization potentials within 1 eV of each other). However, we find that the continuity over velocity between the O I and S II profiles is usually good, which argues against the existence of much contamination from H II regions.

### 4.2. Kinetic Temperature of the C I-bearing Gas

The relationship between the thermal pressure and the fine-structure excitations has a weak dependence on temperature. Thus, even though this effect is small, we must still try to reduce the ambiguities in the measurement of  $p$  when either  $n(\text{H})$  or  $T$  is unknown. Fortunately, we can make use

---

depth  $\tau_a < 0.05$ ) and the S II line was badly saturated ( $\tau_a > 2.5$ ). In this range, we adopted a geometric mean as an approximate compromise between the respective upper and lower limits.

of the fact that molecular hydrogen usually accompanies C I and thus we can utilize measurements of the  $J = 0$  to 1 rotation temperature of  $\text{H}_2$  to indicate the most probable kinetic temperature of the material for which we are making pressure measurements. Columns (7) and (8) of Table 2 show the outcomes of such rotation temperature measurements,  $T_{01}$ , along with the sources in the literature where such measurements were listed. In cases where  $T_{01}$  was not measured, we had no alternative but to adopt an arbitrary number  $T = 80$  K, which is close to the median value of all of the measurements. However, variations in  $T_{01}$  from one sightline to the next have *rms* deviations of only 30 K, and deviations of this magnitude alter the outcome for  $\log(p/k)$  by only about 0.06 dex.

We acknowledge the presence of an unavoidable limitation that  $T_{01}$  shows simply an average over all velocities, and it is weighted in proportion to the local density of hydrogen molecules,  $n(\text{H}_2)$ , instead of  $n(\text{C I}_{\text{total}})$ . In some circumstances variations in temperature across different regions along our sightlines might compromise the accuracy of our results, but this is probably not a very important effect.

### 4.3. The Particle Mix

The composition of the gas has a small, but nonnegligible effect on the expected outcomes for  $f_1$  and  $f_2$ . For instance, for  $2.8 \lesssim \log(p/k) \lesssim 3.8$  the inferred pressure for a given ( $f_1, f_2$ ) for pure atomic hydrogen is about 0.1 dex lower than for the equivalent number density of pure  $\text{H}_2$  with  $T_{01} = 80$  K. Thus, in order to minimize the error in the interpretation of the measurements, it is good to adopt an estimate for the most probable mix of gas constituents. Any deviations in the true conditions from whatever we adopt for the molecular fraction,  $f(\text{H}_2) = 2n(\text{H}_2)/[2n(\text{H}_2) + n(\text{H I})]$ , will result in an error for  $\log(p/k)$  of less than 0.1 dex.

We estimate that approximately half of the material in our lines of sight arise from the WNM, which is free of  $\text{H}_2$ , while the remaining half (CNM) that we can see with C I has an appreciable molecular content. If we assume that the CNM has  $f(\text{H}_2) = 0.60$ , then an overall value  $f(\text{H}_2) = 0.42$  would apply to the entire sightline. The latter value is very close to the median outcome for  $f(\text{H}_2)$  found by Rachford et al. (2009)

in their *FUSE* survey of sightlines similar to the ones in the present study. We therefore adopt the assumption that  $f(\text{H}_2) = 0.60$  in our C I-bearing gas, and the mix of ortho- and para- $\text{H}_2$  is governed by the determination of  $T_{01}$  (which is set to 80 K if unknown). Another constituent is helium, whose ratio to hydrogen in atoms and molecules is assumed to be the protosolar value 0.094 given by Lodders (2003). In their normal concentrations in the CNM, electrons and protons have a negligible influence on  $f_1$  and  $f_2$ .

### 4.4. Local Starlight Intensity

In §4.1 we explained how we derive the amount of C II that accompanies the C I. This determination at any particular velocity in a given sightline has two applications. First, as we indicated earlier, it represents our best estimate for the total amount of neutral material associated with the C I. Second, the ratio of C II to C I allows us to estimate the local radiation density, which in turn will be useful for applying a correction to the equilibrium  $f_1$  and  $f_2$  values that allows for effects of optical pumping of the fine-structure levels (see §6.1 and §A.4 for details). As we will show later in §9.1 and §10.5.4, the radiation density outcomes are by themselves of special interest in our overall outlook on the distribution of thermal pressures.

The ionization balance of carbon atoms in the neutral ISM is given by the relation

$$n(\text{C I}_{\text{total}})(I/I_0)\Gamma_0(\text{C I}) = n(\text{C II})[\alpha_e(\text{C II}, T)n(e) + \alpha_g(\text{C II}, n(e), I, T)n(\text{H})] \quad (1)$$

where the photoionization rate  $\Gamma_0(\text{C I}) = 2.0 \times 10^{-10}\text{s}^{-1}$  (Weingartner & Draine 2001a) if the radiation field density  $I$  is equal to a value  $I_0$  specified by Mathis et al. (1983) for the average intensity of ultraviolet starlight in our part of the Galaxy,  $\alpha_e(\text{C II}, T)$  is the radiative plus dielectronic recombination coefficient of C II with free electrons as a function of temperature  $T$  (Shull & Van Steenberg 1982), and  $\alpha_g(\text{C II}, n(e), I, T)$  is the C II recombination rate due to collisions with dust grains (and subsequent transfer of an electron) normalized to the local hydrogen density (Weingartner & Draine 2001a).<sup>7</sup> To solve for

<sup>7</sup>In the notation of Weingartner & Draine (2001a), this electron transfer rate from grains is expressed as  $\alpha_g(\text{C}^+, \psi, T)$ ,

$n(e)$ , we assume that free electrons are created by both the photoionization of some heavy elements, amounting to  $2 \times 10^{-4}n(H)$ , supplemented by electrons liberated from the cosmic-ray ionization of hydrogen at a rate  $\zeta_{\text{CR}} = 2 \times 10^{-16}\text{s}^{-1}$  (Indriolo et al. 2007; Neufeld et al. 2010).<sup>8</sup> In order to estimate the density of electrons created by these cosmic-ray ionizations, one must calculate the balance between the creation of free protons with a density  $n(p)$  against their recombination with free electrons and also electrons on dust grains using an equation analogous to Eq. 1,

$$\zeta_{\text{CR}}n(\text{H}) = n(p)[\alpha_e(\text{H II}, T)n(e) + \alpha_g(\text{H II}, n(e), I, T)n(\text{H})]. \quad (2)$$

As with the case for C II, we obtain a formula for  $\alpha_g(\text{H II}, n(e), I, T)$  from Weingartner & Draine (2001a).

There may be some shortcomings in our simple formulation in Eq. 1. Welty et al. (1999) found inconsistencies in the determinations of electron densities using the ratios of neutral and ionized forms of different elements, and these problems are not resolved when the grain recombination processes are included (Weingartner & Draine 2001a). Either the rates incorporated into Eq. 1 are inaccurate or other kinds of reactions may be important, such as charge exchange with protons, or the formation and destruction of CO (van Dishoeck & Black 1988) or other C-bearing diatomic molecules (Prasad & Huntress 1980; van Dishoeck & Black 1986, 1989).

If we use our determination of  $N(\text{C II})$  discussed in §4.1, compare it with  $N(\text{C I}_{\text{total}})$ , and apply the equilibrium condition expressed by Eq. 1 to determine the local starlight density, we should obtain a reasonably accurate result for  $I/I_0$  provided that there is not a large amount of C II arising from the WNM at exactly the same velocity. If such an additional contribution is present, we will overestimate the radiation density. Likewise, this overestimate of  $N(\text{C II})$  accompanying the C I will give a disproportionately large figure for the total amount of neutral material for the

---

where  $\psi = GT^{\frac{1}{2}}n(e)^{-1}$  and  $G = 1.13$  for the interstellar radiation field of Mathis et al. (1983).

<sup>8</sup>For the column densities of hydrogen considered here, the average ionization from x-rays is almost negligible by comparison (Wolfire et al. 1995).

particular measurement at hand.

## 5. Admixtures of Different Kinds of Gas

It is clear that the 2-dimensional distribution of the points shown in Fig. 2 represents a complex mixture of high and low pressure gas. Some insight on the possible nature of this mixture may be gained by stripping away the information about the 2-dimensional scatter of the points and focusing on just a composite value of  $(f1, f2)$  for all of the measurements, that is, a single “center of mass” of all of the points in the diagram. The location of this value is shown by a white  $\times$  in the figure. The question we now ask is whether or not some simple, generalized distribution function for pressures can reproduce the observed composite  $(f1, f2)$  pair.

A very elementary but plausible pressure relationship to propose is a lognormal distribution, which is appropriate for situations where random pressure fluctuations arise from turbulence (Vázquez Semadeni 1994; Nordlund & Padoan 1999; Kritsuk et al. 2007) – see §9.1. Panels (a) through (c) in Figure 3 show reconstructions of the combinations of  $f1$  and  $f2$  for such a distribution for three different values for the width of the distribution in  $\log(p/k)$  and a single value for the location of the peak. One might initially suppose that the curvature of the high pressure tail in this distribution along an arc that traces the single-region  $(f1, f2)$  combinations could pull the distribution’s composite  $(f1, f2)$  to a location above the curve at low pressures. However, Figure 3 illustrates that this curvature appears to be insufficient to make our model lognormal composite values rise as high (in  $f2$ ) as the measured ones without passing beyond the composite measurement of  $f1$ . Instead, it appears that a more complex picture is called for, one that requires the use of a bimodal distribution of pressures. The simplest such model is to propose the existence of a separate, small contribution from material at pressures  $\log(p/k) > 5.5$  and a temperature  $T > 80$  K. Panel (d) of the figure shows that such a contribution can solve our problem with the elevated composite  $(f1, f2)$ . This high pressure contribution seems to be present in a majority of the sightlines, since most of the individual points that are shown in Fig. 2 are pulled above the curves.



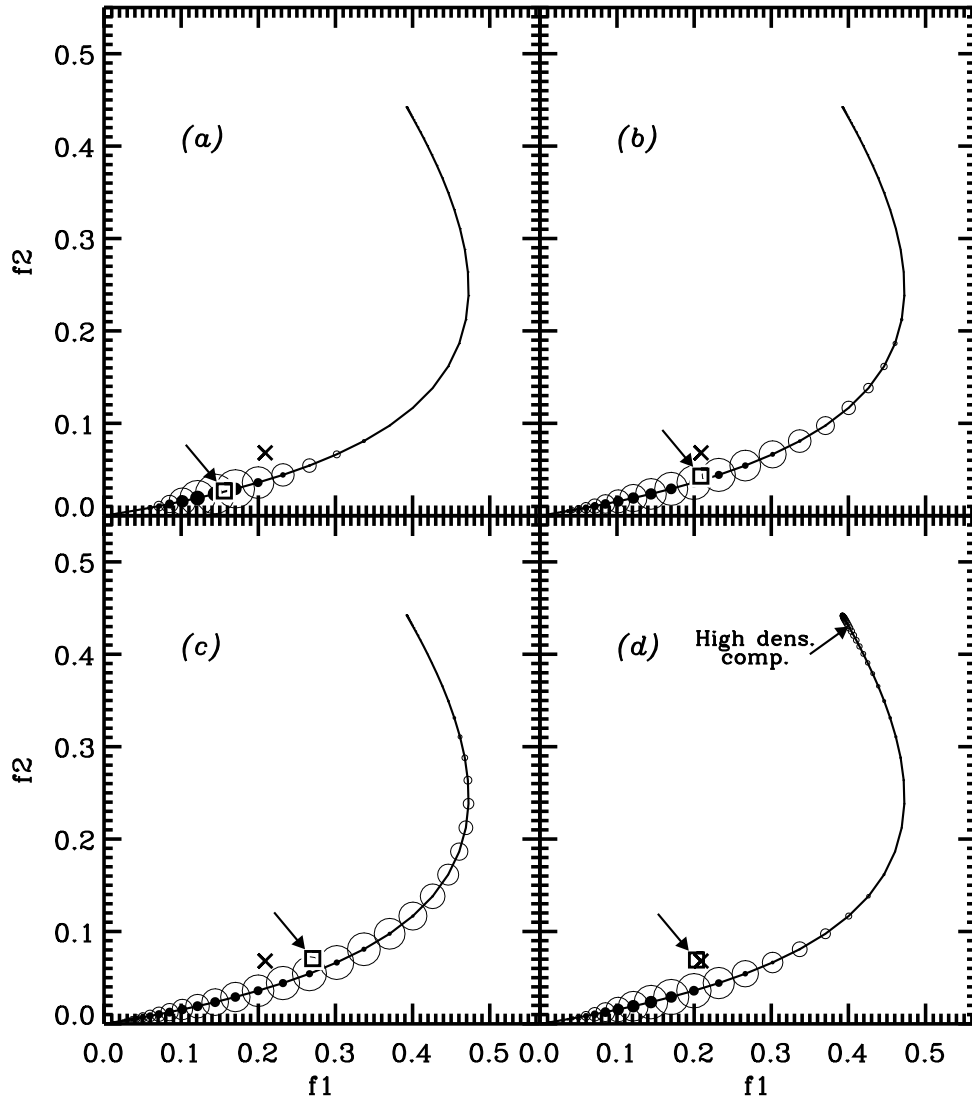


Fig. 3.— A schematic demonstration of the behavior of the composite values of  $f_1$  and  $f_2$  when the pressure distribution follows a simple lognormal behavior. The distribution is approximated by a discrete collection of H I packets spaced 0.1 dex apart in pressure, illustrated by black dots strung along the equilibrium curve, with the area of each dot indicating the amount of H I. After factoring in the ionization equilibrium equation for carbon atoms, the amounts of C I are strongly biased in favor of higher densities. The amounts of C I are indicated by the areas enclosed by open circles. The “center of mass” for the C I packets appears at the location of the square with an arrow pointing toward it, while the observed composite ( $f_1$ ,  $f_2$ ) shown in Fig. 2 is indicated with an  $\times$ . Panels (a) through (c) show lognormal distributions with 3 successively increasing values of  $\sigma$ , while panel (d) shows the outcome when a small, additional contribution of very high density gas is present (very small circles at the top of the equilibrium curve).

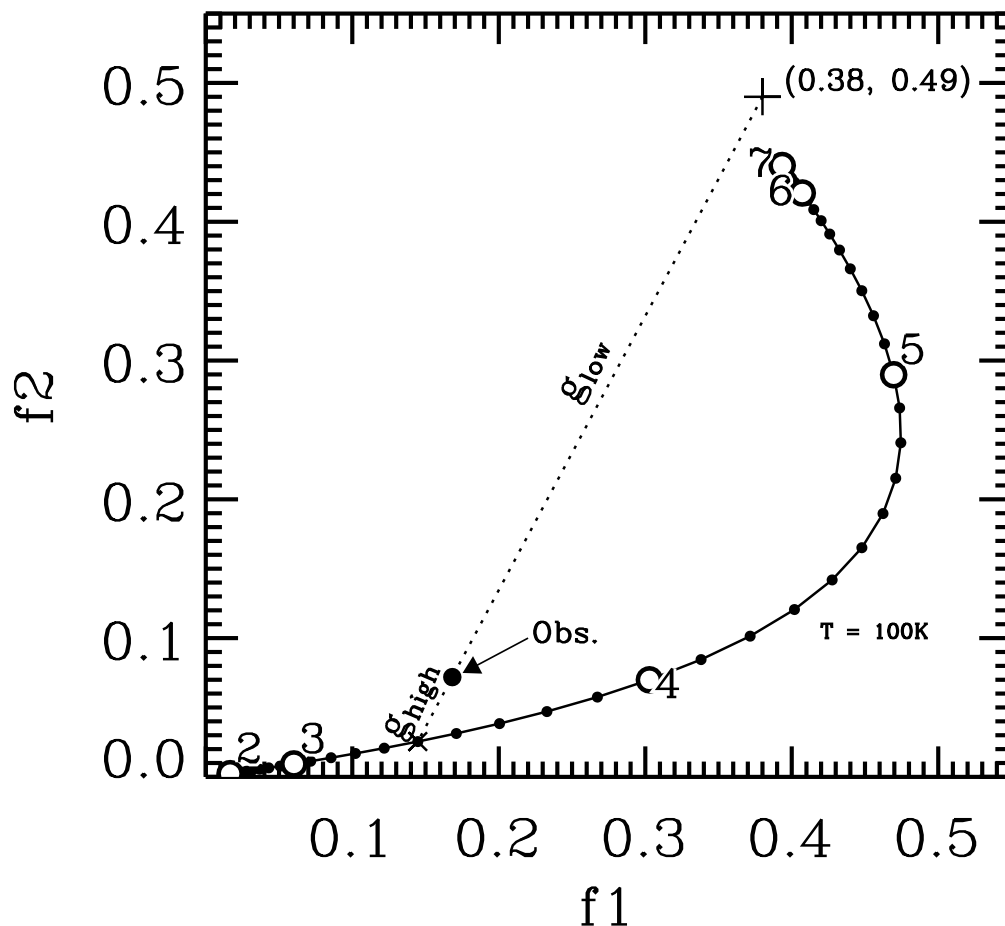


Fig. 4.— A demonstration of how an observed  $(f_1, f_2)$  at a given velocity is decomposed into a superposition of low and high pressure regions. As in Fig. 2, the equilibrium track is marked with a scale in  $\log(p/k)$ , with open circles and accompanying numbers showing integer values of this quantity. An assigned location of  $(0.38, 0.49)$  in this diagram applies to the high pressure component, and a line that projects from this point through the observed  $(f_1, f_2)$  intersects the equilibrium curve (for a given temperature) at a point  $\times$  that corresponds to the pressure of the low pressure component (in this case  $\log(p/k)_{\text{low}} = 3.5$ ). The relative distances along the projection line indicate fractions of C I in the two components: in this depiction, the length of the segment above “Obs.” indicates that fraction of gas at normal (low) pressures is  $g_{\text{low}} = 0.90$ , and the remaining fraction in the high pressure component is indicated by the length of the lower line segment, yielding  $g_{\text{high}} = 0.10$ .

The exact properties of the distribution of high pressure material is not known, but for ( $f1$ ,  $f2$ ) outcomes not far above the lower portions of the equilibrium curves, such details do not matter much for the low pressure gas. We need only to know the general vicinity in the upper portion of the diagram where such material resides. Henceforth, we adopt (0.38, 0.49) for a fiducial  $f1$  and  $f2$  for the high pressure component (which corresponds approximately to  $T = 300$  K,  $n(\text{H I}) = 4000 \text{ cm}^{-3}$ ), and consider that from one observation to the next, the relative proportion of this gas is some small fraction of the total that can vary from one case to the next. The consequences of the high-pressure reference point differing from reality will be discussed briefly in §7.

Figure 4 is a schematic illustration of how we geometrically decompose an observed combination of  $f1$  and  $f2$  into a superposition of the two proposed types of gas, one at a very high pressure (but with poorly known physical conditions) and the other at a normal, low pressure. The basic strategy is to find where a projection from the assumed high density locus (0.38, 0.49) through the observed combination of  $f1$  and  $f2$  extends to a specific point on the equilibrium curve drawn for an appropriate temperature, as defined by  $T_{01}$ , if available. We regard the pressure that corresponds to this intersection point to represent the proper result for the low density gas. The ratio of C I in the high pressure gas to the overall total is given by the quantity  $1 - g_{\text{low}}$  (or simply  $g_{\text{high}}$ ) shown in the diagram.

Two different considerations governed our choice of the fiducial high pressure ( $f1$ ,  $f2$ ) to be situated near the top of the points shown in Fig. 2. One is based on the plausibility that for most of the ordinary lines of sight the amount of this gas (in terms of the total gas, not just C I) is probably a small fraction of all of the gas. At the highest pressures, C I is more conspicuous (because of the shift in the ionization balance toward the neutral form of C), which in turn leads to a smaller quantity for the inferred amount of singly-ionized carbon. The other consideration is a practical one: the numerical results for the decompositions into low and high pressure gas are more stable when the high pressure point is well removed from the measured values of  $f1$  and  $f2$  – this becomes important for outcomes at moder-

ately high pressures above the main distribution of low pressures.

In the next several sections, we will concentrate on the measurements of the low pressure component, using the method just described. Later, in §10.5, we will turn our attention to the small amount of gas at high pressures and discuss its possible significance in our understanding of processes in the diffuse ISM.

## 6. Derivations of Thermal Pressures

### 6.1. Initial Estimates of Conditions

For each measurement of ( $f1$ ,  $f2$ ), we apply the construction demonstrated in Fig. 4 to determine the quantities  $\log(p/k)_{\text{low}}$  and  $g_{\text{low}}$ . This determination is based on the initial assumption that the radiation field intensity  $I(\lambda)$  in the gas in the low pressure regime is equal to the average Galactic value  $I_0(\lambda)$  (see §4.4). Any deviation of the true intensity from this relationship will result in an error in  $\log(p/k)$  because an incorrect calculation of the optical pumping rate was applied. (Different pumping rates have virtually no effect on the value of  $g_{\text{low}}$  since the equilibrium values of  $f1$  and  $f2$  simply shift along the curve that represents different pressures.)

In order to obtain a more accurate result, we must evaluate how much the true intensity  $I(\lambda)$  differs from  $I_0(\lambda)$ , so that our pumping correction will be more accurate. We make the simplifying assumption that the relative distribution of intensity over  $\lambda$  does not change appreciably from one location to the next, but that the overall level of radiation is a free parameter that can vary. We then estimate an initial approximation for the value of this parameter, which we call  $I/I_0$ . To derive this estimate we make use of the ionization equilibrium equation, Eq. 1, to solve for  $I/I_0$  for gas at any particular velocity increment, after replacing  $n(\text{C II})$  by  $N(\text{C II})$  (as determined according to the method described in §4.1),  $n(\text{C I}_{\text{total}})$  by  $g_{\text{low}}N(\text{C I}_{\text{total}})$  and  $n(\text{H})$  by our initial approximate value of  $p/(kT_{01})$ . In making the substitution for  $n(\text{C I}_{\text{total}})$ , we assume that it is safe to declare that virtually all of the C II is associated with the low pressure component of C I, but this condition could be violated if the radiation density experienced by the high pressure gas is many orders of magnitude higher than that of the gas at

ordinary pressures.

## 6.2. Convergence to Final Values

After evaluating the new radiation intensity level  $I/I_0$ , we are in a position to repeat the calculation of  $\log(p/k)_{\text{low}}$  using a better representation for the shifts in the expected values of  $f_1$  and  $f_2$  caused by optical pumping.<sup>9</sup> However, the new value for the pressure will have an impact on the density  $n(\text{H})$  used in the equation for the ionization equilibrium, hence the calculation of this balance must be repeated in order to derive a modified number for radiation enhancement factor  $I/I_0$ , one that is better suited for a more accurate derivation of the pressure. We cycle through the alternation between pressure and ionization calculations many times until the densities and intensities converge to stable solutions.

## 7. Overview of Sightlines

Table 3 presents a number of properties of the C I and (inferred) C II data that we obtained for the sightlines that were suitable for study. The numbers in this table give general indications integrated over velocity; they were not used in the analysis of the pressure distribution, which relied on the more detailed results that we obtained for the explicit velocity channels.

We show our estimates of the total column densities of C II in Column (3) of the table. They compare favorably with the few direct determinations reported in the literature (see note  $f$ ); rms deviations between our values and others amount to 0.22 dex. When we consider that the direct measurements of  $N(\text{C II})$  have quoted errors of order 0.1 dex, the magnitudes of the disagreements indicate that our values are probably uncertain by about 0.20 dex. The largest deviations seem to occur for cases where the other determinations are higher than ours, which may indicate that we are

not registering some C II in ionized gas because we are mostly using O I as an indicator (see §4.1).

The relative coverages of velocities where  $f_1$  and  $f_2$  could be measured, weighted by their respective values of  $N(\text{C II})$ , are given for each sightline in Column (4) of the table. These quantities vary by large factors from one case to the next. For the entire survey that spanned a total length of 180 kpc, the total  $N(\text{C II}) = 3.8 \times 10^{19} \text{cm}^{-2}$ , while that within our sampled velocity intervals represents  $N(\text{C II}) = 2.3 \times 10^{19} \text{cm}^{-2}$  (61%). It is difficult to gauge the real fraction of the gas for which our measurements apply (i.e., CNM vs. CNM + WNM) because some of the WNM material can overlap in velocity the CNM that we sampled. Based on approximate interpolations of the velocity profiles of gas that is relatively free of C I, we estimate the fraction to be in the general vicinity of 15%, which means that on average our determinations could be systematically low by about  $-0.07$  dex.

Uncertainties in  $g_{\text{low}}$  and  $\log(p/k)_{\text{low}}$  are probably dominated by deviations of the real high-pressure conditions from those that apply to our adopted location for  $f_1, f_2 = (0.38, 0.49)$ , as we outlined in §5. One can estimate the magnitudes of such deviations by examining plausible alternative geometrical constructions of the type depicted in Fig. 4. For example, if conditions in the high pressure gas are closer to  $T = 100$  K,  $\log(p/k) = 5.3$  and  $g_{\text{high}} \approx 0.1$  (i.e., twice the general average), an apparent value of  $\log(p/k)_{\text{low}} = 3.5$  may be 0.1 dex higher than the true value. The magnitude of this effect scales in proportion to  $g_{\text{high}}$ , and it is diminished for higher values of  $\log(p/k)_{\text{low}}$ .

In the light of our remarks about various forms of sampling bias in §2 (item 1), it should come as no surprise that values of  $\log(I/I_0)$  shown in Column (7) of the table are all greater than zero. This is a consequence of the CNM being preferentially located in the vicinity of hot stars, rather than in random locations in the Galactic disk. This preference seems to overcome the effects of attenuation of starlight by dust. However, to some limited extent our intensity outcomes could be elevated in a systematic fashion by the presence of unrelated WNM gas that is at the same velocity as the C I. This extra gas would mislead us into thinking the carbon atoms in the regions of interest are more ionized than in reality.

<sup>9</sup>The shift in the outcome for  $\log(p/k)$  depends not only on the strength of the pumping field intensity, but also on  $p/k$  itself. Figure 6 of Jenkins & Shaya (1979) shows the  $(f_1, f_2)$  equilibrium tracks for  $I/I_0 = 1$  and 10, but in terms of our revision of the pumping rates derived in §A.4, these tracks are equivalent to present-day values for  $I/I_0$  equal to about 1.5 and 15. Representative values for  $\log(p/k)$  and  $\log(I/I_0)$  are listed for each sight line in Columns (6) and (7) of Table 3.

TABLE 3  
OBSERVED AND CALCULATED QUANTITIES OVER ALL VELOCITIES IN THE SIGHTLINES

Target Star (1)	$\log N(\text{C I}_{\text{total}})^{\text{a}}$ ( $\text{cm}^{-2}$ ) (2)	Calc. $\log$ $N(\text{C II})^{\text{b}}$ ( $\text{cm}^{-2}$ ) (3)	Percent C II Observed <sup>c</sup> (4)	Weighted Averages <sup>d</sup>		Median $\log(I/I_0)^{\text{e}}$ (7)
				$g_{\text{low}}$ (5)	$\log(p/k)_{\text{low}}$ (6)	
CPD-59D2603 . . . . .	$\gtrsim 14.64$	17.87	25.4	0.92	3.63	0.31
HD 108 . . . . .	$\gtrsim 14.98$	17.81	64.4	0.95	3.82	0.30
HD 1383 . . . . .	$\gtrsim 14.80$	17.84	44.5	0.96	3.49	0.27
HD 3827 . . . . .	$13.57 \pm 0.07$	17.22	7.3	0.92	3.51	0.16
HD 15137 . . . . .	$14.62 \pm 0.01$	17.69	74.3	0.98	3.61	0.32
HD 23478 . . . . .	$> 14.75$	17.35	46.4	0.93	3.62	0.46
HD 24190 . . . . .	$14.45 \pm 0.01$	17.49	84.5	0.97	3.64	0.62
HD 24534 (X Per) . .	$> 14.81$	17.49 <sup>f</sup>	5.0	0.95	4.17	1.16
HD 27778 (62 Tau) . .	$> 14.98$	17.48 <sup>f</sup>	53.4	0.90	3.54	0.49
HD 32040 . . . . .	$13.26 \pm 0.03$	16.58	18.1	0.97	3.07	0.11
HD 36408 . . . . .	$\gtrsim 14.17$	17.33	54.5	0.93	3.82	0.81
HD 37021 ( $\theta^1$ Ori B)	$13.64 \pm 0.05$	17.78 <sup>f</sup>	67.5	0.39	3.83	1.83
HD 37061 ( $\nu$ Ori) . .	$13.97 \pm 0.03$	17.90 <sup>f</sup>	86.3	0.59	4.28	1.80
HD 37903 . . . . .	$14.24 \pm 0.05$	17.75	48.8	0.79	4.61	1.37
HD 40893 . . . . .	$14.67 \pm 0.01$	17.79	91.7	0.98	3.40	0.37
HD 43818 (11 Gem) . .	$14.76 \pm 0.01$	17.89	91.9	0.98	3.49	0.35
HD 44173 . . . . .	$13.66 \pm 0.05$	16.98	4.1	0.83	3.45	0.45
HD 52266 . . . . .	$14.34 \pm 0.01$	17.62	63.0	0.98	3.39	0.48
HD 69106 . . . . .	$14.30 \pm 0.01$	17.37	81.1	0.96	3.55	0.45
HD 71634 . . . . .	$14.13 \pm 0.02$	17.18	68.3	0.89	4.08	0.88
HD 72754 (FY Vel) . .	$\gtrsim 14.40$	17.54	37.0	0.89	3.86	0.83
HD 75309 . . . . .	$14.39 \pm 0.02$	17.51	74.3	0.97	3.41	0.46
HD 79186 (GX Vel) . .	$\gtrsim 14.57$	17.76	69.8	0.96	3.33	0.40
HD 88115 . . . . .	$14.03 \pm 0.05$	17.56	29.4	0.98	3.55	0.51
HD 91824 . . . . .	$\gtrsim 14.45$	17.49	63.6	0.93	3.62	0.78
HD 91983 . . . . .	$14.54 \pm 0.01$	17.55	76.3	0.96	3.53	0.51
HD 93205 . . . . .	$14.56 \pm 0.02$	17.83	51.5	... <sup>g</sup>	... <sup>g</sup>	0.58
HD 93222 . . . . .	$14.36 \pm 0.01$	17.82	72.6	0.95	4.41	0.82
HD 93843 . . . . .	$14.15 \pm 0.05$	17.67	12.8	0.88	4.13	0.66
HD 94454 . . . . .	$> 14.29$	17.50	30.5	0.93	3.60	0.68
HD 94493 . . . . .	$14.26 \pm 0.02$	17.51	59.1	0.97	3.53	0.49
HD 99857 . . . . .	$14.59 \pm 0.01$	17.71	69.9	0.94	3.65	0.55
HD 99872 . . . . .	$\gtrsim 14.41$	17.45	79.4	0.94	3.62	0.86
HD 102065 . . . . .	$\gtrsim 14.22$	17.40	53.9	0.96	3.62	0.61
HD 103779 . . . . .	$14.23 \pm 0.03$	17.60	44.8	1.00	3.29	0.33
HD 104705 (DF Cru)	$14.25 \pm 0.01$	17.58	66.7	0.98	3.48	0.53
HD 106343 (DL Cru)	$14.34 \pm 0.01$	17.62	58.1	0.96	3.51	0.49
HD 108002 . . . . .	$\gtrsim 14.45$	17.58	51.3	0.96	3.41	0.34
HD 108639 . . . . .	$14.31 \pm 0.01$	17.75	76.3	0.96	3.49	0.55
HD 109399 . . . . .	$14.27 \pm 0.02$	17.60	37.9	0.97	3.69	0.59
HD 111934 (BU Cru)	$\gtrsim 14.48$	17.70	43.5	0.99	3.71	0.63
HD 112999 . . . . .	$14.23 \pm 0.02$	17.42	82.7	0.97	3.61	0.53
HD 114886 . . . . .	$14.73 \pm 0.01$	17.75	66.5	0.95	3.62	0.37
HD 115071 . . . . .	$14.69 \pm 0.01$	17.87	74.3	0.94	3.64	0.74
HD 115455 . . . . .	$14.63 \pm 0.02$	17.85	61.3	0.97	3.52	0.58
HD 116781 . . . . .	$14.28 \pm 0.02$	17.75	32.2	0.98	3.42	0.47
HD 116852 . . . . .	$14.15 \pm 0.02$	17.45	66.0	0.95	3.72	0.80
HD 120086 . . . . .	$13.20 \pm 0.08$	16.98	3.6	0.99	3.72	0.50
HD 121968 . . . . .	$13.38 \pm 0.06$	16.87	47.0	0.95	3.81	1.27

TABLE 3—*Continued*

Target Star (1)	$\log N(\text{C I}_{\text{total}})^{\text{a}}$ ( $\text{cm}^{-2}$ ) (2)	Calc. $\log$ $N(\text{C II})^{\text{b}}$ ( $\text{cm}^{-2}$ ) (3)	Percent C II Observed <sup>c</sup> (4)	Weighted Averages <sup>d</sup>		Median $\log(I/I_0)^{\text{e}}$ (7)
				$g_{\text{low}}$ (5)	$\log(p/k)_{\text{low}}$ (6)	
HD 122879 .....	14.42±0.01	17.75	76.3	0.99	3.59	0.49
HD 124314 .....	≥14.66	17.85	66.0	0.97	3.54	0.58
HD 140037 .....	≈14.03	17.24	4.8	≈ 1.0	5.19	0.95
HD 142315 .....	13.78±0.06	17.33	7.3	0.93	3.38	0.50
HD 142763 .....	13.38±0.06	17.03	24.9	0.93	3.47	0.70
HD 144965 .....	>14.28	17.52	9.4	0.82	3.80	0.76
HD 147683 .....	≈14.80	17.64	39.7	0.89	3.89	0.57
HD 147888 ( $\rho$ Oph)	>14.51	17.80 <sup>f</sup>	26.9	0.68	3.98	1.20
HD 148594 .....	≈14.12	17.54	39.3	0.79	4.51	1.53
HD 148937 .....	≈14.87	17.96	90.6	0.95	3.84	0.67
HD 152590 .....	14.61±0.01	17.76 <sup>f</sup>	77.0	0.87	3.71	0.77
HD 156110 .....	13.88±0.04	17.08	45.6	0.99	3.83	0.57
HD 157857 .....	14.61±0.01	17.77	87.2	0.95	3.50	0.46
HD 165246 .....	≈14.33	17.73	59.4	0.94	3.58	0.79
HD 175360 .....	13.98±0.01	17.29	76.6	1.00	3.18	0.39
HD 177989 .....	≈14.66	17.44	72.5	0.96	3.59	0.35
HD 185418 .....	>14.72	17.71	66.8	0.97	3.41	0.23
HD 192639 .....	≈14.74	17.85	80.0	0.97	3.68	0.52
HD 195965 .....	≈14.48	17.42	60.2	0.96	3.56	0.32
HD 198478 (55 Cyg)	≈14.84	17.80	84.5	0.92	3.68	0.43
HD 198781 .....	≈14.56	17.57	32.0	0.92	3.49	0.37
HD 201345 .....	13.97±0.02	17.42	63.4	0.97	3.50	0.32
HD 202347 .....	14.61±0.01	17.33	79.5	0.95	3.76	0.20
HD 203374 .....	≈14.98	17.68	81.1	0.94	3.63	0.31
HD 203532 .....	>14.65	17.40	4.2	0.85	4.40	1.26
HD 206267 .....	≈15.29	17.85	72.4	0.93	3.64	0.30
HD 206773 .....	≈14.70	17.55	71.8	0.96	3.55	0.19
HD 207198 .....	≈15.24	17.81 <sup>f</sup>	87.6	0.94	3.63	0.20
HD 208440 .....	≈14.84	17.68	78.8	0.94	3.66	0.35
HD 208947 .....	≈14.63	17.36	53.2	0.97	3.60	0.33
HD 209339 .....	14.76±0.01	17.61	87.1	0.96	3.69	0.34
HD 210809 .....	≈14.70	17.69	36.8	0.94	3.66	0.29
HD 210839 ( $\lambda$ Cep)	≈14.95	17.79	63.8	0.86	4.16	0.47
HD 212791 .....	14.28±0.03	17.44	29.9	0.97	3.54	0.38
HD 218915 .....	14.56±0.01	17.59	68.9	0.97	3.58	0.33
HD 219188 .....	13.92±0.04	17.08	77.6	0.99	2.97	0.01
HD 220057 .....	>14.71	17.46	25.6	0.94	3.51	0.35
HD 224151 .....	≈14.62	17.80	56.1	0.97	3.80	0.16
HDE 232522 .....	≈14.60	17.66	58.5	0.97	3.53	0.35
HDE 303308 .....	14.69±0.00	17.83	72.9	... §	... §	0.59

<sup>a</sup>Integrated over all velocities where C I absorption seems to be visible (not just over the restricted regions where the lines are strong enough to yield good measurements of  $f_1$  and  $f_2$ ). Sometimes there was evidence that unresolved saturations were evident at certain velocities, as indicated by a test that is discussed in §A.2.4. When this occurred over very limited portions of the profile, we indicate a mild inequality with “≈.” When a substantial portion of the profile exhibited such behavior, we indicate a more severe inequality by “>.” When errors in the column densities are given, they indicate only the quantifiable errors arising from noise or uncertainties in the continuum levels. These errors indicate the relative quality of the measurements, but they are not fully realistic because they do not take into account uncertainties in our adopted  $f$ -values or occasional flaws in the MAMA detector used by STIS.

<sup>b</sup>The computed amount of C II at all velocities based on the absorption profiles of O I or S II; see §4.1 for

details. These amounts compare favorably with the observed amounts for a few stars in note *f*.

<sup>c</sup>The relative amount of C II, as represented by its proxy O I (and sometimes S II), within the velocity interval where determinations of *f*<sub>1</sub> and *f*<sub>2</sub> were good enough to be considered for pressure measurements, compared to the amount seen at all velocities, as shown in the previous column.

<sup>d</sup>Calculated according to the following:  $\frac{\sum [g_{\text{low}} N(\text{C I}_{\text{total}})]}{\sum N(\text{C I}_{\text{total}})}$  and  $\log \frac{\sum [(p/k)_{\text{low}} N(\text{C II})]}{\sum N(\text{C II})}$ .

<sup>e</sup>Our estimate for the local density of UV radiation from starlight that is more energetic than the ionization potential of neutral carbon, compared to an adopted standard *I*<sub>0</sub> based on a level specified by Mathis et al. (1983) for the average intensity of ultraviolet starlight in the Galactic plane at a Galactocentric distance of 10 kpc. This estimate is based on our evaluation of the ionization equilibrium of C, as expressed in Eq. 1.

<sup>f</sup>Compare with actual measurements of  $\log N(\text{C II})$  using the intersystem C II] line at 2325 Å: From Sofia et al. (1998) HD 24534: 17.51 (+0.11, -0.16). From Sofia et al. (2004) HD 2778: < 17.34; HD 37021: 17.82 (+0.12, -0.18); HD 37061: 18.13 (+0.04, -0.06); HD 147888: 18.00 (+0.07, -0.09); HD 152590: 18.21 (+0.08, -0.10); HD 207198: 17.98 (+0.11, -0.14). However, recent measurements of the damping wings for the allowed transition at 1334.53 Å reported by Sofia et al. (2011) indicate that these column densities may be too large by a factor of about 2.

<sup>g</sup>Gas within a component at large negative velocities has conditions very near the high pressure reference mark. Hence the projection onto the low pressure arc is meaningless.

Of particular interest are the characteristic sizes of the regions containing the C I that we are able to study. Within any velocity bin, we can determine a value for the local density of gas particles, composed of atomic hydrogen, helium atoms, and hydrogen molecules. Once again, if we assume that  $f(\text{H}_2) = 0.6$  (see §4.3) and  $\text{He}/\text{H} = 0.09$ , it follows that the local density of hydrogen nuclei is given by  $n(\text{H}) = p/(0.79kT)$ . The longitudinal thickness occupied by the gas is then equal to the column density of these nuclei,  $N(\text{H})$ , divided by  $n(\text{H})$ . We obtain  $N(\text{H})$  by multiplying the amount of carbon, measured by the methods outlined in §4.1, by the general expectation for  $(\text{H}/\text{C}) = 5040$  in the ISM. A sum over velocity of all of the length segments gives the overall thickness of the C I-bearing region(s) in any particular line of sight.

Figure 5 shows the distribution of region thicknesses for all of the lines of sight in our survey, which generally have dimensions of less than 20 pc. The occupation fractions are quite small, generally less than about 2%.

For the benefit of future investigations that may require more detailed information about individual sight lines, Table 4 provides a machine-readable summary that lists for each velocity channel the measured values of  $f_1$ ,  $f_2$ , and  $N(\text{C I}_{\text{total}})$ , along with the calculated values of  $N(\text{C II})$ ,  $g_{\text{low}}$ ,  $\log(p/k)_{\text{low}}$ , and  $\log(I/I_0)$ .

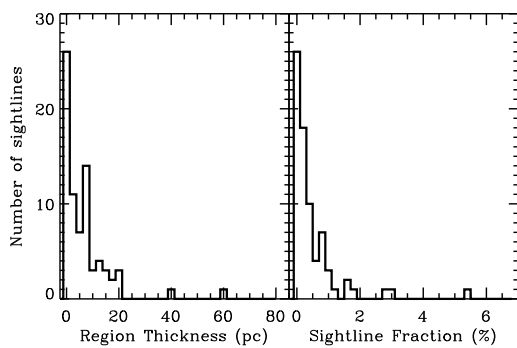


Fig. 5.— Histograms that show (*left*) the total thicknesses of the regions and (*right*) their relative occupation fractions in the sightlines that we are able to measure in the survey.

## 8. Behavior with Velocity

The radial velocities that we measure in the C I profiles arise from various kinematical phenomena, such as differential velocities caused by rotation or density waves in the Galaxy, coherent motions caused by discrete dynamical events such as supernova explosions, mass loss from stars, the collision of infalling halo gas with material in the Galactic plane, and random motions arising from turbulence. With the exception of differential Galactic rotation, all of these effects can transform some of their energy into an increase of the thermal pressures. In their limited sample of only 21 stars, JT01 found elevated pressures in gases whose velocities deviated away from the range that was expected for differential Galactic rotation. We now revisit this issue for our present, much larger sample of sightlines to further substantiate the evidence for a coupling between the thermal pressures and unusual dynamical properties of the gas.

Figure 6 shows the measurements of  $f_1$  and  $f_2$  at velocities that are either above or below the respective line-of-sight velocity ranges permitted by differential Galactic rotation, assuming that the rotation curve is flat at  $254 \text{ km s}^{-1}$  and the distance to the Galactic center is  $8.4 \text{ kpc}$  (Reid et al. 2009). An extra margin of  $5 \text{ km s}^{-1}$  is added to the exclusion zone for permitted velocities, so that we are more certain of showing material that genuinely disturbed in some manner. When we compare the results of Fig. 6 to those shown in Fig. 2, it is clear that gases at high velocity do not have nearly as strong a central concentration near  $f_1 \approx 0.2$  and  $f_2 \approx 0.07$ . The “center of mass” ( $f_1, f_2$ ) locations for all of the points shown in Fig. 6 are  $(0.265, 0.163)$  for negative velocities and  $(0.228, 0.078)$  for positive velocities. By comparison, for all measurements shown in Fig. 2, we found the balance point to be at  $(0.209, 0.068)$ . These differences are principally caused by a greater prominence of a more highly dispersed population of points in  $f_1$  and  $f_2$ , and they should come as no surprise since they demonstrate the expected coupling of the dynamics of the gas to the observed enhancements in the thermal pressures.



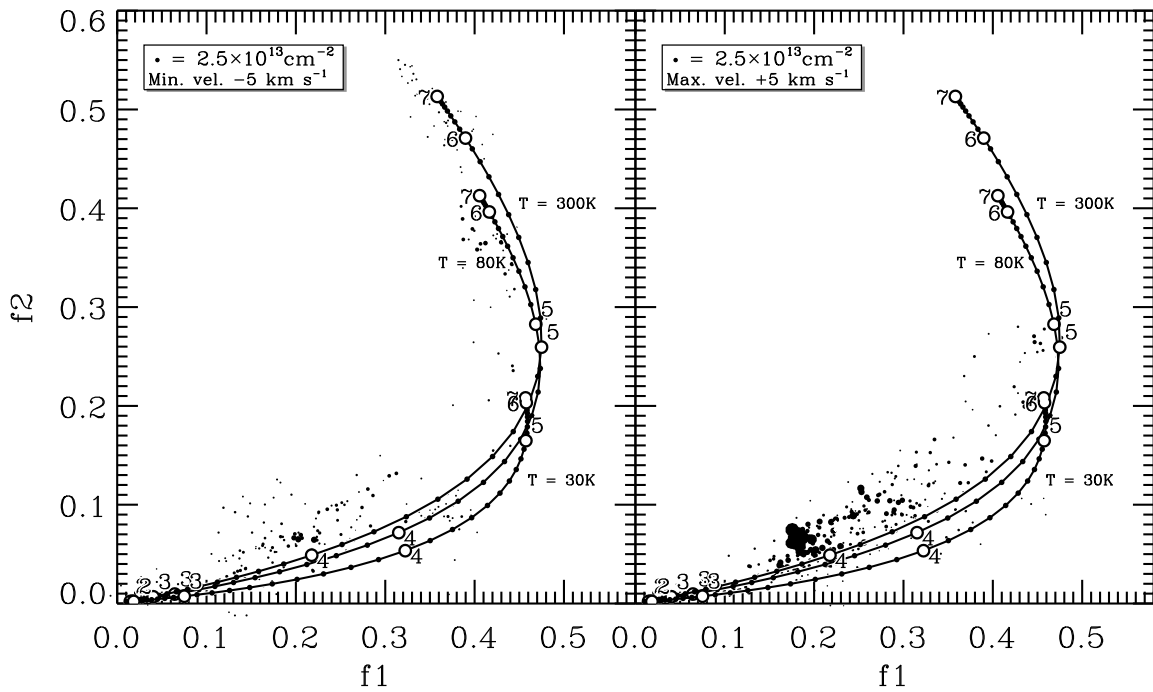


Fig. 6.— Presentations similar to Fig. 2, except that the measurements include velocities only below the minimum value permitted by differential Galactic rotation, but with an extra margin of  $5 \text{ km s}^{-1}$ , i.e.,  $v < \min(v_{\text{gr}}) - 5 \text{ km s}^{-1}$  (*left-hand panel*) or more than  $5 \text{ km s}^{-1}$  above the maximum permitted velocities, i.e.,  $v > \max(v_{\text{gr}}) + 5 \text{ km s}^{-1}$  (*right-hand panel*). The dot diameters in these diagrams are twice as large as those in Fig. 2 for a given column density of  $C \text{ I}_{\text{total}}$ .

TABLE 4  
OBSERVED AND CALCULATED QUANTITIES IN SPECIFIC VELOCITY CHANNELS

Target Star	Velocity (km s <sup>-1</sup> )	$f_1$	$f_1$ Error	$f_2$	$f_2$ Error	$N(\text{C I}_{\text{total}})$ (cm <sup>-2</sup> )	$N(\text{C II})$ (cm <sup>-2</sup> )	$g_{\text{low}}$	$\log(p/k)_{\text{low}}$	$\log(I/I_0)$
CPD-59D2603	4.0	0.213	0.016	0.068	0.026	2.13e+013	1.34e+016	0.930	3.63	0.37
CPD-59D2603	4.5	0.201	0.013	0.065	0.020	2.81e+013	1.44e+016	0.933	3.60	0.28
CPD-59D2603	5.0	0.200	0.011	0.065	0.017	3.33e+013	1.56e+016	0.934	3.60	0.25
CPD-59D2603	5.5	0.207	0.010	0.065	0.015	3.83e+013	1.76e+016	0.936	3.62	0.26
CPD-59D2603	6.0	0.218	0.009	0.064	0.013	4.46e+013	2.02e+016	0.945	3.67	0.29
CPD-59D2603	6.5	0.224	0.008	0.065	0.011	5.30e+013	2.46e+016	0.944	3.68	0.31
CPD-59D2603	7.0	0.227	0.008	0.066	0.009	6.26e+013	3.03e+016	0.943	3.69	0.33
CPD-59D2603	7.5	0.230	0.008	0.070	0.008	7.17e+013	3.80e+016	0.938	3.70	0.37
CPD-59D2603	8.0	0.233	0.008	0.074	0.007	7.88e+013	4.63e+016	0.931	3.70	0.41
CPD-59D2603	8.5	0.222	0.008	0.079	0.007	8.10e+013	5.13e+016	0.910	3.65	0.40
CPD-59D2603	9.0	0.200	0.007	0.081	0.007	7.65e+013	5.18e+016	0.894	3.56	0.35
CPD-59D2603	9.5	0.181	0.007	0.081	0.009	6.53e+013	4.85e+016	0.885	3.47	0.32
HD102065 ...	8.5	0.188	0.019	0.071	0.016	2.42e+012	5.98e+014	0.908	3.51	0.09
HD102065 ...	9.0	0.241	0.012	0.072	0.010	3.87e+012	6.54e+014	0.934	3.71	0.14
HD102065 ...	9.5	0.275	0.008	0.067	0.006	5.93e+012	7.52e+014	0.966	3.83	0.14
HD102065 ...	11.0	0.223	0.004	0.050	0.003	1.64e+013	1.56e+016	0.973	3.62	0.61
HD102065 ...	11.5	0.203	0.005	0.048	0.002	1.92e+013	1.99e+016	0.967	3.55	0.59
HD102065 ...	12.0	0.187	0.005	0.046	0.002	2.14e+013	2.40e+016	0.964	3.49	0.57
HD102065 ...	12.5	0.176	0.005	0.043	0.002	2.38e+013	2.83e+016	0.965	3.44	0.54
HD102065 ...	13.0	0.177	0.004	0.043	0.002	2.70e+013	3.13e+016	0.965	3.45	0.55
HD102065 ...	13.5	0.187	0.004	0.046	0.002	3.06e+013	3.67e+016	0.967	3.49	0.59
HD102065 ...	14.0	0.204	0.004	0.051	0.002	3.32e+013	4.35e+016	0.964	3.54	0.66
HD102065 ...	16.0	0.318	0.005	0.099	0.003	1.47e+013	2.83e+016	0.925	3.85	1.06
HD102065 ...	16.5	0.315	0.005	0.101	0.004	1.00e+013	1.87e+016	0.918	3.84	1.03
HD102065 ...	17.0	0.298	0.007	0.091	0.006	6.78e+012	1.05e+016	0.931	3.81	0.95
HD102065 ...	17.5	0.281	0.010	0.074	0.008	4.54e+012	3.97e+015	0.954	3.80	0.74
HD102065 ...	18.0	0.270	0.014	0.059	0.012	3.07e+012	2.74e+015	0.983	3.78	0.72
HD102065 ...	18.5	0.273	0.021	0.053	0.018	2.11e+012	2.55e+015	0.998	3.77	0.80
HD102065 ...	19.0	0.283	0.030	0.055	0.026	1.45e+012	2.15e+015	1.000	3.79	0.89

(This table is available in its entirety in a machine-readable form in the online journal. A portion is shown here for guidance regarding its form and content.)

Models of pressurized clouds behind weak shocks in the ISM computed by Bergin et al. (2004) reveal that the outcomes for  $(f1, f2)$  are centered on values of approximately  $(0.36, 0.18)$ ,  $(0.40, 0.25)$  and  $(0.37, 0.35)$  for the post-shock condensations behind shocks with velocities of 10, 20 and  $50 \text{ km s}^{-1}$ , respectively (see their Fig. 8; in these cases the resultant ram pressures were  $1.4 \times 10^4$ ,  $5.8 \times 10^4$  and  $3.6 \times 10^5 \text{ cm}^{-3} \text{ K}$  for a preshock density of  $1 \text{ cm}^{-3}$ ). These results for  $f1$  and  $f2$  are well removed from the densest clustering of measurements shown in Fig. 2, but they do seem consistent with the more sparse population of points having  $f2 > 0.15$ , which is more strongly emphasized in the unusual velocity ranges represented by the two panels of Fig. 6.

Figure 6 shows clearly that a moderate number of the measurements in the positive-velocity regime exhibit higher pressures than usual, but not to the great extremes revealed by the negative velocity gas. We offer a simple interpretation for why this happens. We propose that a significant fraction of the high pressure material arises from stellar mass-loss outflows that eventually collide with the ambient medium, creating dense, expanding shells that are at high pressures (Castor et al. 1975; Weaver et al. 1977). Another possibility is that small clouds surrounding the stars are pressurized and accelerated by either the momentum transfer arising from photoevaporation (Oort & Spitzer 1955; Kahn 1969; Bertoldi 1989) or the momentary surge in pressure of a newly developed H II region. These phenomena associated with our target stars should be visible to us if they contain C I. The shells should be intercepted by our sight lines regardless of whether they (or possibly small clouds inside them) are large and at moderately high pressures or very small and at much higher pressures. The foreground portions of such shells are responsible for the negative velocity gas that we can view in the star's spectrum. For positive velocity gas the situation is different. Here, we rely entirely on the random chance of seeing either one of the large-scale events (of non stellar origin) mentioned at the beginning of this section, or else the rear portion of some region or shell that is created by some foreground star or stellar association that is unrelated to the star that we are viewing. This being the case, there may be a vanishingly small chance that we will intercept

a highly pressurized shell with a small diameter, but the chances increase for larger shells that have lower pressures at their boundaries. This observational bias against small, high pressure events at positive velocities could explain why we see no points at  $\log(p/k) > 5$  in the right-hand panel of the figure.

In the next section (and in §10.5.4), we will reinforce the picture that high pressures arise from the increased dynamical activity near bright stars. We will show evidence that there is a strong correlation between pressures and the local intensities of ionizing radiation.

## 9. Interpretations of the Results

### 9.1. Basic Distribution Functions

After evaluating the conditions within each velocity interval for all of the lines of sight, we are in a position to look at the composite outcome of all of the results of the dominant low-pressure component. All of the presentations in this section will show distributions expressed in terms of the amount of hydrogen in a given condition. In order to do so, we must convert our original measurement weights based on  $N(\text{C I}_{\text{total}})$  into ones that account for the equivalent column densities of C II that we derived from our determinations of O I (and on rare occasions S II) at identical velocities, as discussed in §4.1. Once again, we convert from  $N(\text{C II})$  to  $N(\text{H})$  by multiplying the amount of carbon by  $(\text{H}/\text{C}) = 5040$  in the ISM. As we indicated earlier (§4.4), WNM material at the same velocity as the CNM will tend to inflate somewhat the derived value of  $N(\text{H})$  associated with the C I that is used for determining the pressure.

The histogram distributions shown in Fig. 7 reveal that the pressure distribution function is not strongly influenced by the temperature of the gas, as deduced from the measurements of  $T_{01}$  of  $\text{H}_2$ . Nevertheless, the evidence that we have suggests an inverse correlation of pressures with temperature, although the scatter in this relationship is large. For the points shown in the inset of the figure, the Spearman rank order correlation coefficient is  $-0.29$ . This determination is significantly different from a zero correlation for the population at the 97.5% confidence level for 58 pairs of measurements. The dispersion of the results is so large that it is difficult to assign a value for the

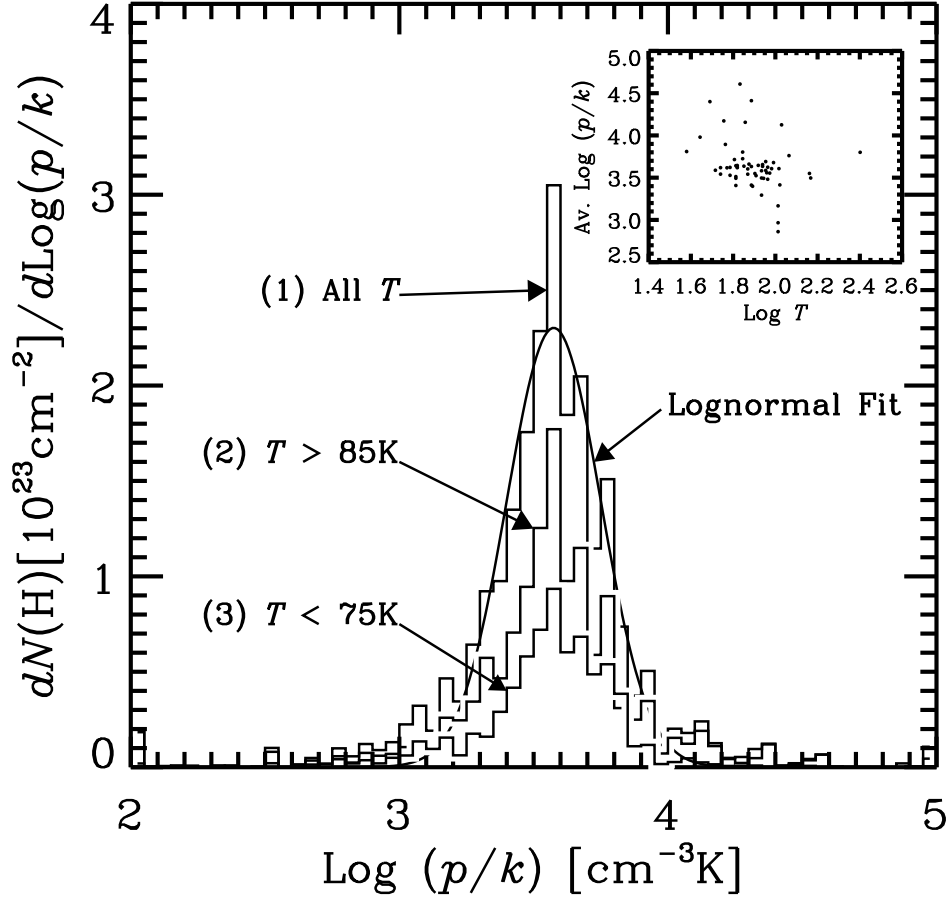


Fig. 7.— The distribution of thermal pressures, normalized to the estimated amount of hydrogen present, for three different temperature conditions, as indicated by the  $J = 0$  to 1 rotation temperatures of  $\text{H}_2$ : (1) all of the gas (tallest profile), (2) gas for which  $T_{01} > 85$  K (middle profile) and (3) gas for which  $T < 75$  K (shortest profile). The median temperature for all cases is 77 K, i.e., a value that is between the two limits. Sight lines where  $T_{01}$  measurements do not exist are included in condition (1) but excluded from conditions (2) and (3). A best-fit lognormal distribution for condition (1) is shown by the solid curve, and it is represented by Eq. 3. The inset shows a scatter plot of the C I weighted average  $\log(p/k)$  given in Column (6) of Table 3 vs.  $T_{01}$  (if known), as listed in Column (7) of Table 2.

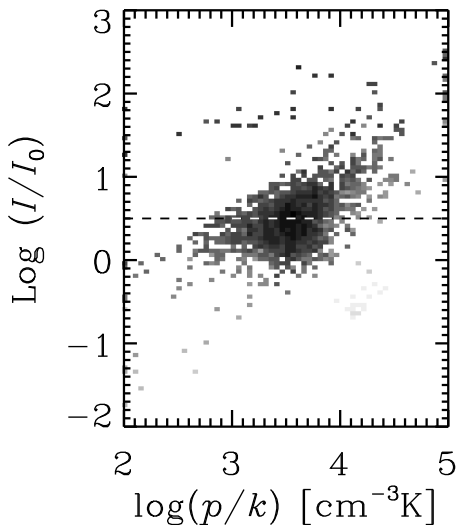


Fig. 8.— A gray-scale representation of the logarithm of the amount of H I gas that we found as a function of  $\log(I/I_0)$ , i.e., the logarithm of the enhancement of the starlight density above average, against the thermal pressure, expressed in terms of  $\log(p/k)$ . The dashed line shows the cutoff equal to  $\sqrt{10}$  times the average field that we established for defining the low intensity distribution shown in Fig. 9.

apparent polytropic index of the gas, but the sign of the trend is consistent with a slope of less than one for the CNM thermal equilibrium track near the minimum pressure shown in Fig. 1.

The central portion of the distribution of thermal pressures (for all  $T_{01}$ ) follows closely a lognormal distribution given by

$$dN(\text{H})/d\log(p/k) = 2.30 \times 10^{23} \exp\left[-\frac{(\log(p/k)-3.58)^2}{2(0.175)^2}\right] \text{cm}^{-2} \quad (3)$$

This lognormal relationship is shown by the smooth curve in Fig. 7 (and will be shown again later in a log-log representation by the smooth gray curve in Fig. 9). Outside the range  $3.2 < \log(p/k) < 4.0$  it understates the observed amount of material in the wings of the profile (this is not evident in Fig. 7, but is clearly shown later in Fig. 9).

Figure 8 shows that the outcomes for the starlight densities and the thermal pressures are

not independent of each other. In regions that are close to stars that emit UV radiation ( $I/I_0 \approx 10$ ), we find that with a few exceptions the average pressures increase to values in the general vicinity of  $\log(p/k) \sim 4$ . This enhancement supports the viewpoint that turbulent energies are greater in the general vicinity of young stars, a phenomenon that may be related to changes in the morphology of H I near stellar associations that were found by Robitaille et al. (2010).

In order to obtain a representation for the pressures in the general ISM somewhat removed from the bright stars, we will limit further study of the distribution to only those cases where  $I/I_0 < 10^{0.5}$ , a limit that is depicted by the dashed line in Fig. 8. We consider that any gas elements that are above that line represent localized regions that are exceptionally close to sources of mechanical energy and are thus not representative of the general, diffuse ISM.

Figure 9 shows in a log-log format the distribution of thermal pressures for  $I/I_0 < 10^{0.5}$  (black histogram) compared with the distribution for all intensities (gray histogram). In terms of  $\log(p/k)$  [and using a linear representation of  $dN(\text{H})/d\log(p/k)$ ], the distribution for the low-intensity results has a mean of 3.47, a standard deviation of 0.253, a skewness of  $-1.8$ , and a kurtosis<sup>10</sup> of 6.2. The influence of the excess of low pressure outcomes, as evidenced by the negative skewness, causes the standard deviation listed here to be larger than the value 0.175 given in Eq. 3, which would apply to just the central portion of the profile.

For the convenience of those who wish to reproduce a reasonably good representation of the low-intensity data in analytical form, we supply an empirical polynomial fit,

$$dN(\text{H})/d\log(p/k) = 1.16 \times 10^{23} \exp(-0.0192z - 0.00387z^2 + 2.39 \times 10^{-5}z^3 + 6.24 \times 10^{-7}z^4 - 6.77 \times 10^{-9}z^5) \text{cm}^{-2}, \quad (4)$$

where the dimensionless quantity  $z = (p/k)^{\frac{1}{2}} - 60$  (for  $p/k$  expressed in terms of  $\text{cm}^{-3}\text{K}$ ). This em-

<sup>10</sup>Our definition of kurtosis includes a subtraction of 3 from the fourth moment divided by  $\sigma^4$ , thus making the kurtosis of a Gaussian distribution equal to zero. Sometimes in the literature, e.g. Federrath et al. (2010), this “-3” term is omitted.

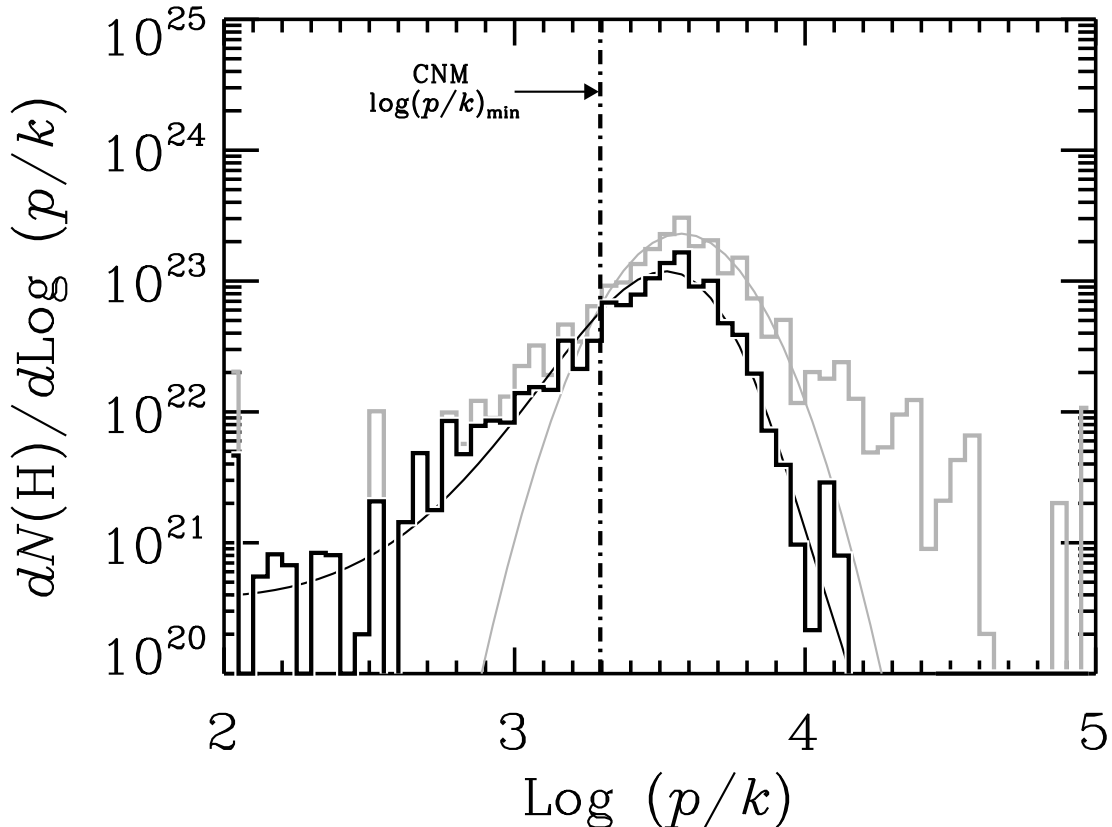


Fig. 9.— Log-log presentations of the distribution of thermal pressures for two cases: all of the gas sampled by C I is shown by the gray histogram, while a subset of the material for which  $I/I_0 < 10^{0.5}$  is shown by the black histogram. This intensity cutoff limits the sample to all of the outcomes that appear below the dashed line in Fig. 8. The thin curves show how well the analytical expressions given in Eqs. 3 (gray) and 4 (black) fit the results. The vertical dot-dash line labeled CNM  $\log(p/k)_{\min}$  corresponds to the minimum pressure that is allowed for a static CNM, as shown by a similar line with the same designation in Fig. 1.

pirical fit is shown by the thin, black curve in Fig. 9. If this distribution function is converted into a linear representation, i.e.,  $N(H)$  as a function of  $p/k$ , we find that for  $p/k < 5500 \text{ cm}^{-3} \text{ K}$  it does not differ appreciably from a Gaussian function with mean value of  $p/k = 3700 \text{ cm}^{-3} \text{ K}$  and a standard deviation of  $1200 \text{ cm}^{-3} \text{ K}$ . The distribution is somewhat higher than this Gaussian function above  $5500 \text{ cm}^{-3} \text{ K}$ .

Our mean value quoted above is 0.22 dex higher than the value  $2240 \text{ cm}^{-3} \text{ K}$  that we listed earlier (JT01). There are three independent reasons that can account for nearly all of this difference. First,

we used revised rates for the collisional excitation and radiative decay of the upper fine-structure levels of C I, as discussed in §A.3. This accounts for an elevation of typical determinations of pressures of about 0.05 dex. Second, our new estimate for the strength of the optical pumping of the levels has been reduced (§A.4), with the result that a typical pressure measurement should be raised by another 0.05 dex. Third, our earlier specification for the mean value of  $p/k$  was for a temperature (40 K) that gave the lowest inferred pressure for a given level of C I excitation, while the present result uses either actual temperatures

measured from the  $\text{H}_2$  rotational excitations or a median value of 80 K if an explicit measurement for a sight line is not available. Under most circumstances, the inferred pressure at 80 K is about 0.1 dex higher than that for 40 K. Taken together, these three effects can account for an elevation of our new pressures over the old ones by 0.2 dex.

As a final point, we add a cautionary note that the errors in our determinations for  $\log(p/k)$  become much larger than usual when their values fall below 3.0. The reason for this is that the changes in  $f1$ , the major discriminant for pressures, become very small at low pressures, as shown by the shrinkage in the spacing between the 0.1 dex markers in Figs. 2 and 4.

## 9.2. Volume-Weighted Distributions

Up to now, the distribution functions that we have shown (Figs. 7–9) have been weighted in proportion to our calculated hydrogen column densities, which is equivalent to a sampling by mass. In many cases, investigators showing results of computer simulations of ISM turbulence express their outcomes according to the counts of volume cells having different pressures. In order to make a conversion from a mass-weighted distribution to a volume-weighted one, we must make a simplifying assumption that we are viewing an ensemble of gases that has internal random pressure fluctuations that change with time, but that is otherwise approximately uniform in nature and that can be characterized as having an equation of state with a single value for the polytropic index  $\gamma$  (equal to the slope of  $\log p$  vs.  $\log n$  or the ratio of specific heats  $c_p/c_v$ ). In this situation, the changes in pressure cause the volumes of mass parcels to change in proportion to  $p^{-1/\gamma}$ , and this factor must be applied to the mass-weighted distribution function to obtain the volume-weighted one.

The smooth curves in Fig. 10 show how the mass-weighted distribution in  $\log(p/k)$  for the low starlight intensities would appear after being converted to volume weighted ones for three different assumed values of  $\gamma$ . These three examples illustrate the behavior of the gas under the conditions (1)  $\gamma = 0.7$ , which is a good approximation of the slope of thermal equilibrium curve for the CNM shown in Fig. 1, (2) the relationship for  $\gamma = 1.0$  that corresponds to an isothermal gas, and (3) a condition  $\gamma = 5/3$  that indicates that the

gas is undergoing adiabatic compressions and expansions (and assuming that the gas has a purely atomic composition). The divergent behavior of the curves at the far left portion of this diagram probably arises from either deviations caused by small number statistics for the samples at the extremely low pressures or the fact that the errors in  $\log(p/k)$  become larger than usual at the low pressure extreme. It is important to emphasize that in a turbulent cascade the notion that the gas has a single polytropic index on all length scales is an oversimplification; we will explore this issue in more detail in §10.3.

## 9.3. Pileup in Velocity Bins

As we discussed in §3, any outcomes for  $f1$  and  $f2$  at a particular velocity may represent a composite result for two or more regions that are seen in projection along the line of sight. In §5 we explained how we separated contributions from small amounts of gas at extraordinarily large pressures, well away from the dominant regime of low pressures. However, we have yet to address the possibility that two or more regions at somewhat different pressures along the lower, nearly straight portion of the  $f1 - f2$  equilibrium curve can create an apparent outcome that represents a proper C I-weighted mean, but without revealing the true dispersion of pressures from the contributors. If such superpositions are taking place frequently, they will tend to decrease the width of our observed overall distribution shown in Figs. 7–9.

One way to gain an insight on this possibility is to examine how deviations from the mean  $\log(p/k)$  scale with the corresponding amounts of C I. If we imagine a simple picture where all of the C I exists within independent parcels, each with some single, representative value  $N_0(C \text{ I}_{\text{total}})$ , we would expect to find that the dispersion of any collection of measurements having some multiple  $n$  times  $N_0(C \text{ I}_{\text{total}})$  would show us a standard deviation equal to  $\sigma_{\text{true}}/\sqrt{n}$ , where  $\sigma_{\text{true}}$  is the real dispersion in  $\log(p/k)$  for the individual packets that are seen in projection.

The upper panel of Figure 11 shows the apparent outcomes for values of  $\log(p/k)$  as a function of  $N(C \text{ I}_{\text{total}})^{-0.5}$ ; it is clear that as the column densities decrease (i.e., moving toward the right of the plot), the vertical dispersions increase. For data segregated within successive bins having a

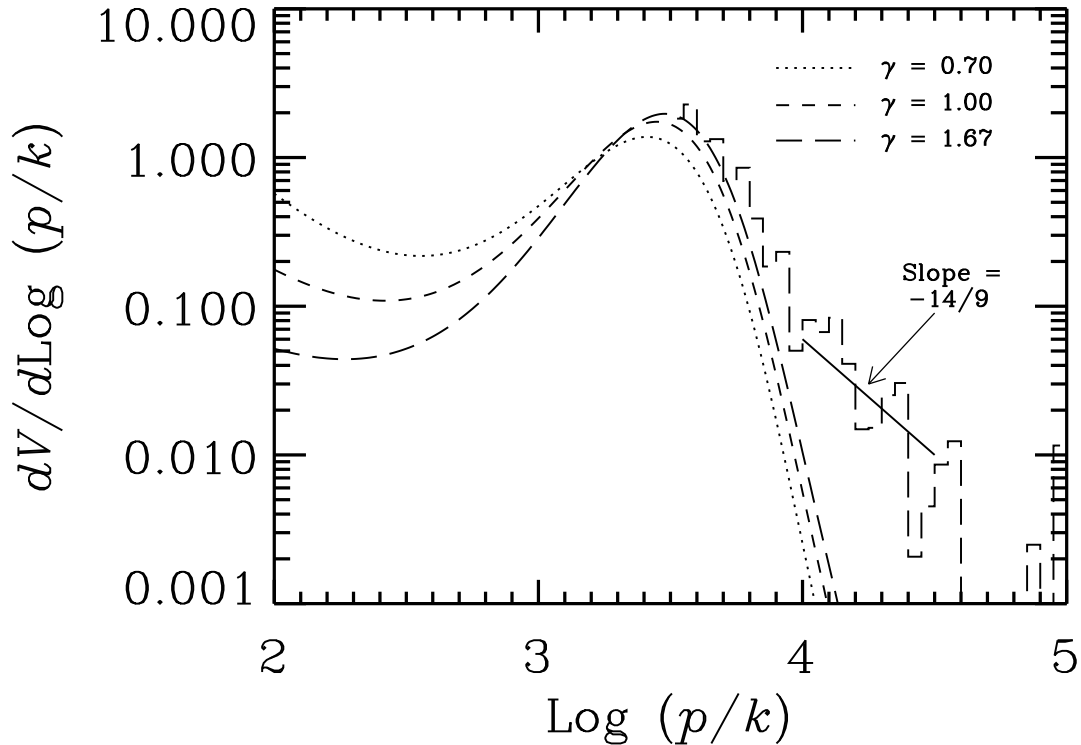


Fig. 10.— (*three smooth curves:*) The results of a conversion of the mass-weighted distribution curve for starlight intensity levels  $I/I_0 < 10^{0.5}$  (the black, smooth curve shown in Fig. 9) to volume weighted ones for three assumed values for  $\gamma$ , corresponding to cases where the gas behaves as if it were in thermal equilibrium ( $\gamma = 0.70$ ), isothermal ( $\gamma = 1.0$ ) and adiabatic ( $\gamma = 1.67$ ). (*Histogram-style trace:*) The volume-weighted distribution for all intensity levels for  $\log(p/k) > 3.5$ , assuming  $\gamma = 1.67$ . This distribution is relevant to a discussion that is presented in §10.4 about the possible creation of higher than normal pressures by expanding supernova remnants. In all four cases, the curves are normalized such that their integrals over all  $\log(p/k)$  equal 1.0.

width of  $\sqrt{2} \times 10^{-7}$  cm, the lower panel indicates that the *rms* dispersion indeed seems to scale in direct proportion to  $N(C I_{\text{total}})^{-0.5}$ , but only up to about  $N(C I_{\text{total}})^{-0.5} = 5\sqrt{2} \times 10^{-7}$  cm (indicating that  $N_0(C I_{\text{total}}) \approx 2 \times 10^{12} \text{cm}^{-2}$ ). Thus, on the one hand, one could imagine that  $\sigma_{\text{true}}$  could be as large as around 0.5, instead of our overall measured value of 0.253. On the other hand, the proposed model for superpositions may be only a product of our imagination: perhaps coherent regions with larger values of  $N(C I_{\text{total}})$  have a real tendency to be less easily perturbed by various external forces that cause pressure deviations away from some mean value. In essence, the

trend shown in Fig. 11 may reflect a real physical effect rather than a trend caused by random superpositions of unrelated, small gas clouds.

In principle, a trivial explanation for the effect shown in Fig. 11 might be that as  $N(C I_{\text{total}})$  decreases the measurement errors in  $\log(p/k)$  increase. However, as we explain later in §A.2.3, the  $1\sigma$  errors in  $f_1$  and  $f_2$  should be equal to 0.03 or less for the measurements to be accepted. At normal pressures this amount of error is equivalent to a change in  $\log(p/k)$  equal to only 0.1 dex, far smaller than the observed dispersion that is shown for low column density cases in Fig. 11. One reason that we are able to maintain small errors



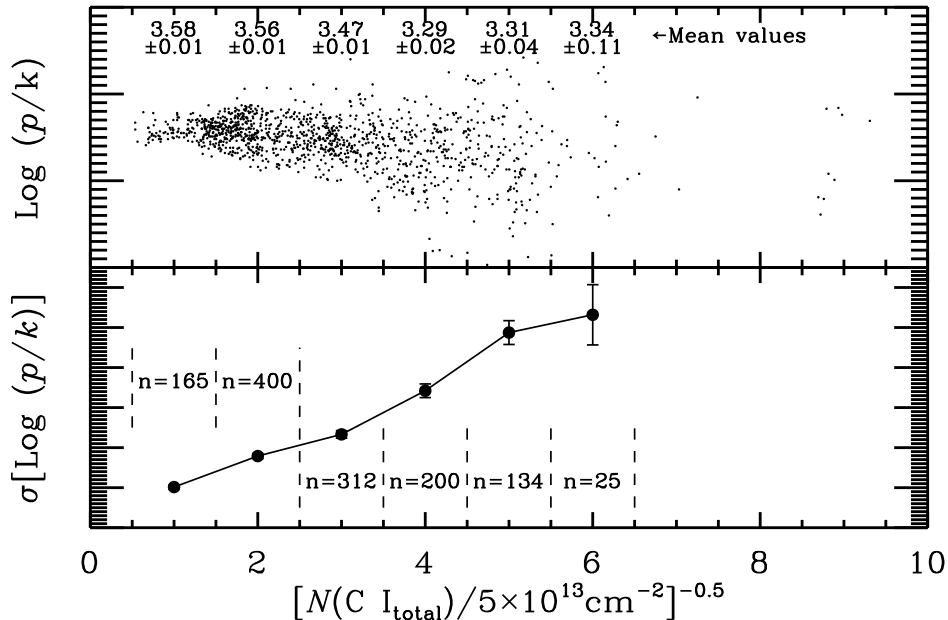


Fig. 11.— *Top panel:* Individual measurements of  $\log(p/k)$  in the low pressure regime as a function of the inverse square-root of the column density of C  $I_{\text{total}}$  for all velocity channels of width  $0.5 \text{ km s}^{-1}$  that had  $\log I/I_0 < 10^{0.5}$ . The mean values of  $\log(p/k)$  are listed near the top of the panel for successive intervals centered on integral values of  $[N(\text{C } I_{\text{total}})/5 \times 10^{13} \text{ cm}^{-2}]^{-0.5}$ . *Lower panel:* The standard deviations  $\sigma[\log(p/k)]$  for measurements within the intervals, showing an almost linear progression up to a value  $\sigma[\log(p/k)] \approx 0.5$ , at which point the column density of independent packets of gas have characteristic values  $N_0(\text{C } I_{\text{total}}) = 2 \times 10^{12} \text{ cm}^{-2}$ . The “ $n =$ ” designations show the number of points that were used to evaluate  $\sigma[\log(p/k)]$  in each bin.

for lower column densities is that our system of weighting the measurements causes a shift of emphasis from weak atomic transitions to stronger ones as  $N(\text{C } I_{\text{total}})$  decreases.

## 10. Discussion

### 10.1. Distribution Width and Shape

#### 10.1.1. Overall Shape

The highly symmetrical appearance of our distribution for all of the material that we sampled in the regime of ordinary pressures (which we identified as the “low pressure component” in §5) is an illusion that arises from the projection of the irregularly shaped distribution depicted in Fig. 8 onto the  $x$ -axis that represents  $\log(p/k)$ . The distribu-

tion function reverts to one with a strong negative skewness when we limit our consideration to conditions where  $I/I_0 < 10^{0.5}$  (below the dashed line in Fig. 8). This behavior is inconsistent with turbulence in an isothermal gas, which should show a pure lognormal density (and pressure) volume-weighted distribution function (Vázquez Semadeni 1994; Nordlund & Padoan 1999; Kritsuk et al. 2007).

#### 10.1.2. Deviations to Low Pressures

A substantial fraction of the material (29%) – that which is depicted to the left of the vertical dash-dot line in Fig. 9 – is detected at pressures below those permissible for a static CNM,  $(p/k)_{\text{min}} = 1960 \text{ cm}^{-3} \text{ K}$ , as defined by the “standard model” for the thermal equilibrium curve

presented by Wolfire et al. (2003) that we show in Fig. 1.<sup>11</sup> From this we conclude that either their curve does not apply to the media we are viewing or else that rarefactions caused by turbulence create momentary excursions below the curve. The recovery toward normal pressures for regions that reach anomalously low pressures in some cases might be inhibited by temporary, locally high values of magnetic pressure (Mac Low et al. 2005).

A valid question to pose is whether or not we could understand the existence of low pressures by large changes in some of the parameters that influence the value of  $(p/k)_{\min}$  within some localized regions. Wolfire et al. (2003) expressed a simple equation [their Eq. (33)] that gives some guidance on this possibility. We restate their equation terms of our variables by substituting  $0.674(I/I_0)$  for their normalized ISM intensity  $G'_0$  at a Galactocentric distance of 8.5 kpc. The reason for this substitution is that we have adopted a more recent measure of a standard intensity  $I_0$  (Mathis et al. 1983) that is lower than the one they chose to use [taken from Draine (1978)]. Also, we set their parameter for the total ionization rate (multiplied by  $10^{16}\text{s}^{-1}$ )  $\zeta'_t = 2.0$ , since we have adopted a cosmic ray ionization rate  $\zeta_{\text{CR}} = 2 \times 10^{-16}\text{s}^{-1}$  (see §4.4) and assumed that the x-ray and EUV ionization rates are very small in comparison. Our restatement of their equation takes the form,

$$(p/k)_{\min} = 5730(Z'_d I/I_0) \frac{Z'_g}{1 + 2.08(Z'_d I/I_0)^{0.365}}, \quad (5)$$

where  $Z'_d$  is equal to the normalized ratio of interstellar dust grains to polycyclic aromatic hydrocarbons (PAH), and  $Z'_g$  is the normalized gas phase abundance of heavy elements that are responsible for radiative cooling of the gas (chiefly C and O). The two quantities  $Z'_d$  and  $Z'_g$  are generally assumed to be equal to 1.0 for conditions in our part of the Galaxy. If  $\log(I/I_0) = -0.35$ , we find from Eq. 5 that  $(p/k)_{\min} = 1000\text{cm}^{-3}\text{K}$ . However, the distribution of outcomes shown in Fig. 8 indicate most of our pressure measurements apply to regions with  $\log(I/I_0) > -0.35$ . Another way to reduce  $(p/k)_{\min}$  to  $1000\text{cm}^{-3}\text{K}$  would be

to have  $I/I_0 = 1.0$  but with either a ratio of the dust grain to the PAH concentration  $Z'_d$  as low as 0.45 times the normally assumed value or a reduction of  $Z'_g$  to 0.54 times the normal amount. Even with the possible deviations discussed here that would make  $(p/k)_{\min}$  reach as low as  $1000\text{cm}^{-3}\text{K}$ , we still have measurable amounts of gas below the pressure threshold for a stable CNM.

### 10.1.3. Comparisons with Expectations of the Effects of Turbulence

The magnitude and skewness of the fluctuations in thermal pressure give an indication of the strength and character of the turbulence in the ISM (Padoan et al. 1997b). For instance, the one-dimensional simulations of Passot & Vázquez-Semadeni (1998) illustrated how  $\gamma$  changes the sign of the skewness of the distribution:  $\gamma < 1$  makes the distribution shallower on the high pressure side of the peak and steeper on the low pressure side, while the opposite is true for  $\gamma > 1$ . The influence of the polytropic index on the shape of the distribution can also be seen in the results of three-dimensional simulations performed by Li, et al. (2003) and Audit & Hennebelle (2010). Studies of turbulence in an isothermal medium by Federrath et al. (2008) indicated that the shape of the distribution may also be governed by the character of the driving force: solenoidal (divergence-free) driving forces result in a symmetrical distribution (close to lognormal), while compressive (curl-free) driving can create a negative skewness. In short, the appearance of our pressure distribution seems to favor either  $\gamma > 1$  (i.e, somewhere between isothermal and adiabatic behavior), turbulence that is compressive in nature, or some combination of the two.

One important application of our determination of the dispersion of thermal pressures is to estimate the strength of the turbulence using a quantitative comparison based on computer MHD simulations. Padoan et al. (1997a, b) introduced a scaling relation between the rms dispersion  $\sigma_s$  for a log-normal distribution of the quantity  $s = \ln p$  in terms of a simple function of the Mach number  $M$ ,

$$\sigma_s = [\ln(1 + b^2 M^2)]^{0.5}. \quad (6)$$

Investigators that have adopted this formalism generally find that their simulations seem to sup-

<sup>11</sup>With a parametric formulation discussed in the next paragraph using our value for  $I/I_0 = 1.0$  and  $\zeta_{\text{CR}} = 2 \times 10^{-16}\text{s}^{-1}$ ,  $(p/k)_{\min}$  decreases very slightly to  $1860\text{cm}^{-3}\text{K}$ .

port the validity of a scaling with  $M$  shown in Eq. 6, but values for the constant  $b$  appear to vary from one study to the next. Federrath et al. (2008, 2010) and Brunt (2010) have summarized the outcomes for  $b$  for many different cases reported in the literature: extremes in  $b$  have ranged from 0.3 to 1.0, depending on the conditions in the computations. Simulations carried out by Federrath et al. (2008, 2010) indicate that whether or not the forcing of the turbulence is solenoidal or compressive can have a strong influence on  $b$ . Lemaster & Stone (2008) have shown that magnetic fields have only a small effect on the relationship between  $\sigma_s$  and  $M$ .

We can derive a characteristic turbulent Mach number for the C I-bearing gas by taking our dispersion for  $\ln p$ , adopting a value for  $b$ , and solving for  $M$  in Eq. 6. Here, it is appropriate to use a volume weighted distribution of pressures, since that is the conventional way of describing the outcomes of the simulations. A best-fit of a log-normal distribution to the portion  $\log(p/k) > 3$  of the isothermal curve for low  $I/I_0$  shown in Fig. 10 yields  $\sigma_s = 0.46$ . From the analysis of the possible effects of averaging in velocity bins that we presented in §9.3, we acknowledge that the true dispersion of  $\log(p/k)$  could be as large as 0.5, leading to  $\sigma_s = 0.5 \ln 10 = 1.2$ . For our choice of  $b$ , we adopt the finding by Brunt (2010) that  $b = 0.48^{+0.15}_{-0.11}$ , which was based on the observed density and velocity variances in cold gas with large turbulent Mach numbers in the Taurus molecular cloud. This value is near the middle of the range of those derived from computer simulations of MHD turbulence mentioned in the above paragraph. With this value for  $b$ , we solve for  $M$  in Eq. 6 and derive  $M = 1.0^{+0.3}_{-0.2}$  for our lower value of  $\sigma_s$  and  $M = 3.7^{+1.1}_{-0.9}$  for the larger one. For our representative values  $f(\text{H}_2) = 0.60$  (§4.3) and  $T = 80 \text{ K}$  (§4.2), the isothermal sound speed  $c_s = 0.50 \text{ km s}^{-1}$ . For the smallest value of  $M$  minus its error, we expect the velocity dispersion  $\sigma_v = 0.8c_s = 0.40 \text{ km s}^{-1}$ , and for the largest  $M$  plus its error we expect that  $\sigma_v = 4.8c_s = 2.4 \text{ km s}^{-1}$ .

Over a wide dynamic range in linear separations, the velocity differences for packets of material in the ISM have been observed to scale in proportion to these separations to a fixed power (Larson 1979, 1981; Heithausen 1996; Brunt & Heyer

2002a; Brunt & Kerton 2002). We can factor in our values of  $\sigma_v$  into this relationship to estimate the largest characteristic scales for the turbulent motions, which in turn indicate the largest cloud sizes (or energy injection scales). For the power-law relationship, we adopt the recent finding of Heyer & Brunt (2004),

$$\sigma_v = (0.96 \pm 0.17)r_{\text{pc}}^{0.59 \pm 0.07}, \quad (7)$$

where  $r_{\text{pc}}$  is the linear separation in pc. Solving for  $r_{\text{pc}}$  using our velocity dispersions in this equation yields  $r_{\text{pc}} = 0.23^{+0.04}_{-0.02}$  for  $\sigma_v = 0.40 \text{ km s}^{-1}$  and  $r_{\text{pc}} = 4.7^{+3.7}_{-1.6}$  for  $\sigma_v = 2.4 \text{ km s}^{-1}$ .

In Fig. 5 we showed the distribution of thicknesses of our C I-bearing clouds for the different lines of sight in our survey. The median of all the values for the entire collection is 5.5 pc. On the one hand, this median value is close to the upper end of our range of  $r_{\text{pc}}$ , which may indicate that our larger value of  $\sigma_s$ , i.e., the largest possible dispersion found in §9.3, represents the correct value for the deviations of thermal pressures. On the other hand, the smaller dimensions that apply to the direct measurement  $\sigma_s = 0.46$  may simply indicate that we are usually viewing a superposition of many independent, smaller clouds along each line of sight. We caution that the trend expressed in Eq. 7 is evaluated from  $^{12}\text{CO } J = 1-0$  emission-line data for molecular clouds, which may differ from the relationship for the more diffuse regions that we have sampled.

## 10.2. Time Constants

Since fluid elements in a turbulent medium have physical properties that change with time, it is important to establish the time intervals that are required for various measurable quantities to converge nearly to their equilibrium values. There are three different contexts where we compare two (or more) states of any particular constituent: (1) the ratio of C I fine-structure populations, (2) the balance between neutral and ionized forms of the carbon atoms and (3) the  $J = 0$  to 1 rotational temperature  $T_{01}$  of  $\text{H}_2$ . A fourth time-variable quantity of interest is the kinetic temperature of the gas, which not only influences the other three quantities that we measure but also the manner in which the gas responds to disturbances. We will compute the characteristic  $e$ -folding times for

these processes in the following subsections, and later we will compare them to the eddy turnover times for different size scales.

In a general context, we can imagine atoms or molecules in two possible states with equilibrium number densities  $n_{0,\text{eq}}$  in some lower level and  $n_{1,\text{eq}}$  in an upper one. In equilibrium,

$$R_{01}n_{0,\text{eq}} = R_{10}n_{1,\text{eq}} , \quad (8)$$

where  $R_{01}$  and  $R_{10}$  are the upward and downward conversion rates, respectively. We can propose a solution for the time behavior of the lower level,  $n_0$ , to take the form

$$n_0(t) = n_{0,\text{eq}} + (n_{0,i} - n_{0,\text{eq}})e^{-\gamma t} \quad (9)$$

as the concentration of  $n_0$  adjusts itself from some initial density  $n_{0,i}$  to its equilibrium value  $n_{0,\text{eq}}$ . This form must agree with the condition

$$\begin{aligned} \frac{dn_0(t)}{dt} &= n_1(t)R_{10} - n_0(t)R_{01} \\ &= n_{\text{tot}}R_{10} - n_0(t)(R_{10} + R_{01}) , \end{aligned} \quad (10)$$

where  $n_{\text{tot}} = n_0(t) + n_1(t)$  is the (constant) sum of the number densities of the two levels. If we insert the proposed time behavior (Eq. 9) into the  $n_0(t)$  term of Eq. 10 and compare it to an explicit differentiation of Eq. 9 with time, we can equate the  $e^{-\gamma t}$  terms to reveal that

$$\gamma = R_{10} + R_{01} . \quad (11)$$

(The sum of the remaining terms without  $e^{-\gamma t}$  equals zero.) In essence, any departure from the equilibrium level distribution, either positive or negative in sign, will decay to the equilibrium condition in an exponential fashion with an  $e$ -folding time constant given by Eq. 11. In the following three subsections, we apply this rule to population ratios discussed in items (1) to (3) at the beginning of this section.

#### 10.2.1. *C I Fine Structure Levels*

As a simplification, we consider only the first two levels and ignore the existence of the third (highest) one. Here,  $R_{01}$  equals the sum of the upward rate constants for various collision partners times their respective densities.  $R_{10}$  equals the sum of the downward rate constants times the

densities plus also the spontaneous decay probability  $A_{10}$ . If  $f1$  is small,  $A_{10} = 7.93 \times 10^{-8}\text{s}^{-1}$  (Galavís et al. 1997) dominates over the collisional excitation (and de-excitation) terms. The inverse of  $A_{10}$  equals 146 days. If  $f1$  is not small, the collisional terms make  $R_{10} + R_{01}$  even larger and thus reduce the time constant to less than 146 days. Clearly, even for the more complex situation for the interactions with the highest of the three fine-structure levels, the time constants are extraordinarily short ( $A_{21}^{-1} = 44$  days).

#### 10.2.2. *The Photoionization and Recombination of Carbon Atoms*

Since the equilibrium concentrations of neutral carbon are much smaller than the ionized forms in all cases that we consider, as is evident from Fig. 1, it is clear that the ionization rate  $R_{01} = (I/I_0)\Gamma_0$  dominates over the various recombination terms shown in Eq. 1 that make up  $R_{10}$ . Figure 8 shows us that  $I/I_0 = 1$  is about the lowest value of the radiation density that we encounter. Hence, the longest time constant that we expect to apply is simply  $\Gamma_0^{-1} = 5 \times 10^9\text{s} = 160\text{yr}$ , and this time shortens in proportion to the increase in  $I$  above the reference value  $I_0$ .

#### 10.2.3. *The $J = 0$ to 1 Rotation Temperature $T_{01}$ of $\text{H}_2$*

Cecchi-Pestellini et al. (2005) have performed detailed calculations of the time-dependent  $\text{H}_2$  level populations in turbulent media that have short-lived pockets of hot gas that can leave an imprint on the rotation temperatures. Here, we focus on a much simpler discussion for  $T_{01}$  of the two lowest rotational levels, since they are relevant to our determinations of kinetic temperatures. We evaluate the characteristic time for changes in the population ratio of  $J = 0$  to that of  $J = 1$  when there is a sudden change in the kinetic temperature, but we neglect any of the effects of repopulating the lower levels from cascades from higher levels of excitation.

The rate coefficient for ortho-para transitions caused by neutral hydrogen impacts onto  $\text{H}_2$  is extremely low at the temperatures that we consider [for  $T < 300\text{K}$ ,  $k_{01} < 10^{-16}\text{cm}^3\text{s}^{-1}$  (Sun & Dalgarno 1994)]. For protons, however, the rate constants are much larger:  $k_{10} = 2.0 \times 10^{-10}\text{cm}^3\text{s}^{-1}$

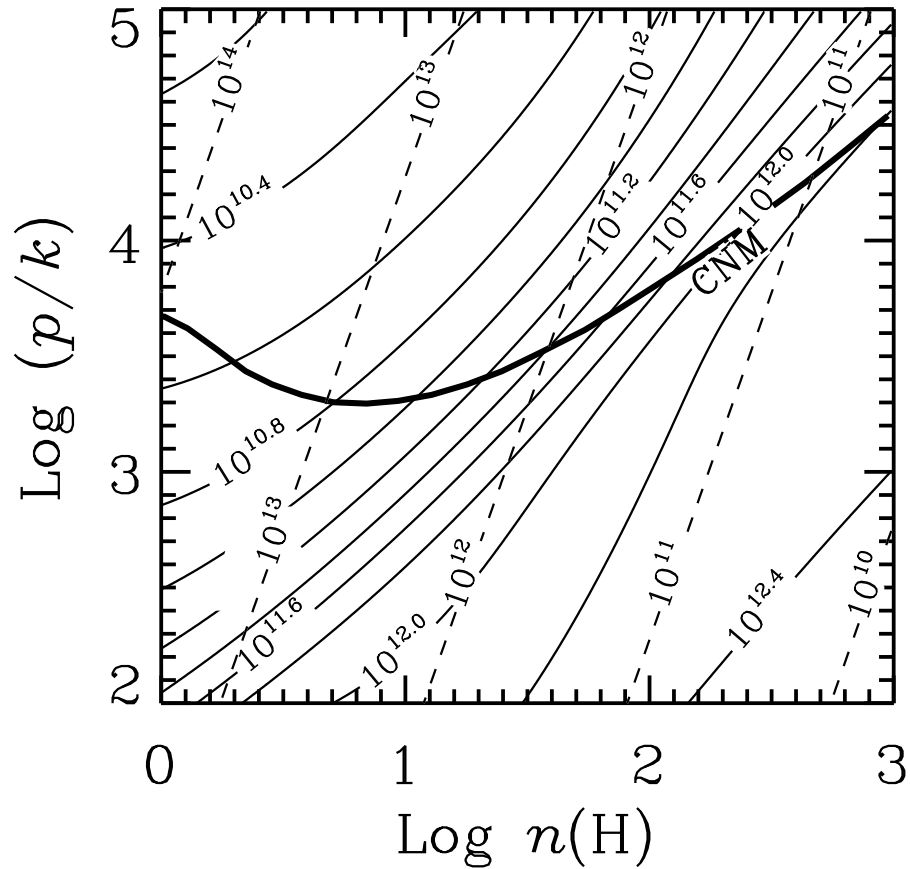


Fig. 12.— Time constants (in seconds) for (1) the relaxation of the  $T_{01}$  rotation temperature of  $H_2$  to the local kinetic temperature (solid contours), as a result of ortho-para conversions of the lowest two levels due to collisions with protons and (2) cooling times  $t_{cool}$  as given in Eq. 12 (dashed lines). The thermal equilibrium curve for the CNM that appears in Fig. 1 is shown by the thick curve. This diagram was constructed assuming that the gas has  $f(H_2) = 0.6$  and  $He/H=0.09$  (see §4.3).

(Gerlich 1990), and  $k_{01} = 9 \exp(-171/T)k_{10}$ . The solid contours in Fig. 12 show how the time constants vary over the  $\log(p/k)$  vs.  $\log n(\text{H})$  diagram when we combine the rate constants with determinations of  $n(p)$  using Eq. 2.

#### 10.2.4. The Kinetic Temperature

Unlike the cases that we considered in §§10.2.1-10.2.3, for the kinetic temperature we must work with a continuous variable instead of a population ratio of two states of some constituent. Thus, a somewhat different tactic is needed to assess the characteristic relaxation time. Wolfire et al. (2003) have evaluated the isobaric cooling time for the ISM and find that

$$t_{\text{cool}} = 7.40 \times 10^{11} \left( \frac{T}{80 \text{ K}} \right)^{1.2} \left( \frac{p/k}{3000 \text{ cm}^{-3} \text{ K}} \right)^{-0.8} \text{ s}. \quad (12)$$

They state that this formula is valid to within a factor 1.35 over the temperature range  $55 < T < 8500 \text{ K}$ . By itself, the coefficient in Eq. 12 applies to conditions very close to our median temperature and pressure in the survey ( $T_{01} = 80 \text{ K}$  and  $p/k = 3000 \text{ cm}^{-3} \text{ K}$ ), and it is not much different from the relaxation time for  $T_{01}$  ( $3.95 \times 10^{11} \text{ s} = 12,500 \text{ yr}$ ) at the same temperature and pressure. We depict values of  $t_{\text{cool}}$  by the nearly straight, dashed contours in Fig. 12.

### 10.3. Turbulent Eddy Crossing Times

As the length scales become smaller, the dwell times for conditions become shorter. It then follows that these shortened durations could curtail physical stasis in certain respects. To estimate the time scales  $\Delta t = r/\Delta v$  for changes to occur in a turbulent eddy with a characteristic radius  $r$ , we can once again make use of the power-law relationship between velocity shears  $\Delta v$  and length scales  $r_{\text{pc}}$  (as we did in §10.1.3), but this time we adopt the findings taken from observations at smaller scales. A slight reduction of the slope seems to occur for these shorter length scales: Falgarone et al. (1992) conclude that  $\Delta v \approx r_{\text{pc}}^{0.4}$  for  $10^{-2} < r_{\text{pc}} < 1$ , and their result agrees with that of Brunt & Heyer (2002b) and Heyer & Brunt (2004) at a common scale  $r_{\text{pc}} = 1$ . This velocity trend for the shorter lengths is consistent with the theoretical study of turbulence by Boldyrev et al. (2002), and we will adopt it for our investiga-

tion of time scales. We recognize, however, that there are isolated observations, such as those carried out by Sakamoto (2002), Sakamoto & Sunaka (2003) and Heithausen (2004, 2006), that show some specific regions where the velocity differences measured over  $r_{\text{pc}} \sim 10^{-3} - 10^{-1}$  are almost one order of magnitude above this velocity-size relationship; see Fig. 10 of Falgarone et al. (2009). Also, observations of CO emission by Hily-Blant et al. (2008) demonstrate that isolated concentrations of turbulent energy over small scales create occasional, large velocity deviations that go well beyond the tails of a Gaussian distribution. Finally, Shetty et al. (2010) indicate that projection effects in the position-position-velocity (PPV) data overestimate the power-law slope (by one to a few tenths) and underestimate the velocity amplitudes (by about a factor of two) in a 3D physical position-position-position (PPP) representation of a turbulent medium. With these points in mind, we make an extrapolation of the trend  $\Delta v = r_{\text{pc}}^{0.4} \text{ km s}^{-1}$  toward very small scales to yield  $\Delta t = r_{\text{pc}}^{0.6} \text{ Myr}$ , but acknowledge that in some circumstances this form for  $\Delta t$  may significantly overestimate the time span for rapid changes in conditions.

For a length scale  $r_{\text{pc}} = 0.00046$  (or 95 AU), we expect that  $\Delta t = 0.01 \text{ Myr}$  (i.e.,  $10^{11.5} \text{ s}$ ). Along the CNM equilibrium curve shown in Fig. 12, this time equals  $t_{\text{cool}}$  at  $\log(p/k) = 3.85$ . The crossing time is about equal to the  $e$ -folding time for  $T_{01}$  at a slightly lower pressure,  $\log(p/k) = 3.6$ . Thus, in short, for scale sizes smaller than about 100 AU (but perhaps a few thousand AU for some of the more active regions) we can expect that turbulent fluctuations at the pressures that we are considering will depart from the CNM thermal equilibrium curve ( $\gamma \approx 0.7$ ) and exhibit an effective  $\gamma$  that is somewhere between 0.7 and the adiabatic value of  $5/3$  (for a pure atomic gas). Over smaller scales (or lower pressures)  $T_{01}$  may depart from the local kinetic temperature. Over all of the practical size scales, the equilibrium results for the C I fine-structure excitations and C ionization should apply, but with the provision that their outcomes depend on the instantaneous temperature.

#### 10.4. Possible Effects from Coherent, Large Scale Disturbances

Up to now, we have considered the effects of compressions and rarefactions caused by random turbulent motions. However, the injection of mechanical energy over macroscopic scales in the Galactic disk can also create deviations in pressure. Supernova blast waves constitute a principal source of this energy in the ISM. We know that there are strongly elevated pressures inside clouds that have recently been overtaken by a supernova blast wave, as shown by the enhanced C I fine-structure excitations that appear in the spectra of stars within and behind the Vela supernova remnant (Jenkins et al. 1981, 1984, 1998; Jenkins & Wallerstein 1995; Wallerstein et al. 1995; Nichols & Slavin 2004). We have good reason to expect that pressure increases with somewhat smaller amplitudes should persist even within remnants that are no longer identifiable because they are so old or disrupted.

In a more general context, at random locations in the disk of the Galaxy the outcomes for the thermal pressure enhancements arising from the effects of supernovae are expected to be appreciably different for the various broad temperature regimes in the ISM, as shown by several different computer simulations (de Avillez & Breitschwerdt 2005a; Mac Low et al. 2005). The simulations have many free parameters that influence the properties of the average pressures and the shapes of the distribution functions. For this reason, we will restrict our attention to a very simple test of the plausibility that, beyond the limited range of fluctuations caused by turbulence, there is a broader, underlying spread of pressures caused coherent, large scale mechanical disturbances arising from supernova explosions.

We can adopt a tactic similar to one developed by Jenkins et al. (1983) in their comparison of C I pressures to a prediction based on the theory of the three-phase ISM advanced by McKee & Ostriker (1977). Small, neutral clouds that are overtaken by an expanding supernova blast wave should rapidly (and adiabatically) adjust their internal thermal pressures to equal that of the hot medium well inside the remnant's boundary. We can now make a simple prediction of what would happen if these clouds actually defined the trend

of the pressure distribution well above the mean pressure and then compare this outcome with our observations.

If the radius  $r$  of any remnant in the adiabatic phase grows in proportion to  $t^\eta$  and its volume-weighted average internal pressure  $p$  is proportional to  $r^\alpha$ , we find that

$$dp/dt = (dp/dr)(dr/dt) \propto r^{\alpha-1+(\eta-1)/\eta}. \quad (13)$$

A time-averaged occupation volume  $V(p)$  is then given by

$$V(p) \propto r^3/(dp/dt) = r^{3-\alpha+1/\eta}, \quad (14)$$

which gives an overall volume filling factor per unit  $\log p$  that is proportional to  $V(p)p = p^{-14/9}$  for  $\alpha = -3$  and  $\eta = 3/5$  (McKee & Ostriker 1977), as long as the remnants do not overlap each other, which should be true at pressures well above the median pressure.

The histogram-style trace in Figure 10 shows our thermal pressure distribution on the assumption that the overtaken clouds contract adiabatically, i.e., with  $\gamma = 5/3$ . Unlike the smooth curves shown in this figure, this distribution represents our entire dataset, i.e., not just the instances where  $I/I_0 < 10^{0.5}$ . Our reason for this choice is that we wish to avoid a bias against regions of higher than normal starlight intensity, because the locations of supernova remnants are correlated with those of associations of early-type stars. As Fig. 10 shows, the pressure distribution has a slope that is roughly consistent with  $dV/d \ln p \propto p^{-14/9}$ .

#### 10.5. High Pressure Component

In §5 we proposed that some small fraction of all of the gas that we observed has an extraordinarily high pressure ( $p/k \gtrsim 3 \times 10^5 \text{ cm}^{-3} \text{ K}$ ,  $T > 80 \text{ K}$ ), in order to nudge the  $f2$  outcomes to locations above the normal equilibrium tracks shown in Fig. 2. We now explore various explanations for the excesses in  $f2$ , starting with ones that do not imply the presence of small amounts of gas at high pressures. Later, on the premise that the existence of the high pressure material is indeed real, we review some suggestions made by other investigators on its possible origin.

##### 10.5.1. A Misleading Conclusion?

Before we fully accept our interpretation that the anomalously high  $f2$  measurements imply the

existence of small amounts of high pressure material, well separated from the main pressure distribution function presented in §9.1, we should briefly investigate possible errors in the interpretation of the outcomes in  $f1$  and  $f2$ . One possibility is that the excitation cross sections or the decay rates for the excited levels have systematic errors that underestimate the populations in the  $^3P_2$  state (C I\*\*) relative to those in the  $^3P_1$  level (C I\*). We feel that this is unlikely, since earlier calculations of these quantities that appeared in the literature (i.e., the ones adopted by JT01<sup>12</sup>) did not yield outcomes that predicted greater values of  $f2$  for their respective  $f1$  counterparts. However, on more fundamental grounds we do not feel qualified to comment on the accuracy of the atomic physics calculations, so we will not pursue this issue further.

Another possibility for misleading results could be errors in our determinations of  $f1$  and  $f2$ . Two possibilities for the origin of such errors could either be errors in the adopted  $f$ -values for the C I transitions or our under-appreciation of the effects of misleading apparent optical depths caused by unresolved, saturated substructures in the absorption line profiles. For the former of the two, we feel that our investigation discussed in Appendix B provides some assurance that we are not experiencing systematic errors in the relative strengths of weak multiplets versus the strong ones. However, our derived  $f$ -values rely on the correctness of the published relative line strengths within multiplets. These relative strengths have a direct influence on our derived values of  $N(\text{C I}^*)$  and  $N(\text{C I}^{**})$ , relative to each other and to  $N(\text{C I})$ .

As for the possibility that we are being misled by incorrect optical depth measurements, we feel that the precautions that we discuss in §A.2.4 for screening out such cases provide adequate safeguards. Moreover, it is reassuring to see that for individual determinations of the apparent fraction of C I in the high pressure component,  $g_{\text{high}}$ , in each velocity bin (i.e., not the overall averages shown in Table 3), there is no trend with  $N(\text{C I}_{\text{total}})$ , an effect that we would have expected to see if the phenomenon were driven by the strengths of the absorption lines.

<sup>12</sup>Appendix A.3 discusses our current updates for the atomic parameters.

Still another effect to examine is the possibility that there is an anomalous means for exciting the fine-structure levels. Positively charged collision partners will give proportionally stronger excitations of the second excited level of C I, as indicated by the differences in cross sections for protons compared to neutrals – see Fig. 1 of Silva & Viegas (2002). If ambipolar diffusion (ion-neutral slip) created by MHD shocks and Alfvén waves create enough suprathermal protons (and heavy element ions) to further excite the C I, they might help to explain the larger outcomes for  $f2$ . While this is a qualitatively attractive explanation, in a quantitative sense it seems to fail: the required fractional concentration of the positively charged collision partners, greater than about 30%, seems to be unreasonably large (e.g., the conditions  $n(\text{H I}) = 2 \text{ cm}^{-3}$ ,  $T(\text{H I}) = 600 \text{ K}$ ,  $n(p) = 0.6 \text{ cm}^{-3}$ ,  $T(p) = 20,000 \text{ K}$  should give  $f1 = 0.23$  and  $f2 = 0.066$ , which is not far from our measured average shown by the white  $\times$  in Fig. 2. Smaller ion fractions fail to do so however).

#### 10.5.2. *The Amount of the High Pressure Component*

We now move on to the premise that we advocated earlier in §5 that the anomalously large values of  $f2$  arise from a small admixture of high pressure gas in virtually all of the cases that we examined. In terms of  $N(\text{C I})$ , the overall fraction  $g_{\text{high}}$  is usually about 5%. However it is important to note that, except in the presence of exceptionally strong ionization field strengths, this outcome must arise from much smaller proportions of H I because the neutral fraction of carbon increases with pressure, making small amounts of high pressure gas far more conspicuous. For instance, we can expect a factor 100 enhancement in fractional amount of C I,  $n(\text{C I}_{\text{total}})/[n(\text{C II}) + n(\text{C I}_{\text{total}})]$ , when the gas is at  $\log(p/k) = 6$ ,  $T = 300 \text{ K}$  over that which would apply to material with more conventional physical conditions  $\log(p/k) = 3.6$ ,  $T = 80 \text{ K}$ . On average, this makes the fractional mass contribution of H I in the high pressure component only about  $g_{\text{high}}/100$ , a 0.05% mass fraction. We add a caution, however, that this fraction could be larger if the actual pressure of the high-pressure component is lower than the value stated above.



### 10.5.3. Radiation from the Excited Levels of Carbon Atoms

Radiative decay of the upper fine-structure level of C II is an important cooling mechanism for the ISM. The rate of this cooling per unit mass can be monitored by either directly observing the emission at 1900 GHz (157.7  $\mu\text{m}$ ) (Stutzki et al. 1988; Langer et al. 2010; Pineda et al. 2010; Velusamy et al. 2010) or by viewing the C II\* absorption features at 1037.018 and 1335.708  $\text{\AA}$ , as has been done for both the ISM of our Galaxy (Lehner et al. 2004) and the distant, damped  $L\alpha$  systems in quasar spectra (Wolfe et al. 2003a, b). It is worthwhile to ask the question: could the regions that we view with enhanced pressures make an important contribution to either the absorption or emission measurements? It is difficult to formulate a precise answer, since we do not fully understand the nature of these regions. On the one hand, the factor 100 diminution in the H I content mentioned in the previous section is approximately offset by a factor 100 enhancement in the collision rate for exciting the upper level of C II. In this circumstance, as long as we are still below the critical density for establishing the C II\* population, our typical value of  $g_{\text{high}}$  of 5% would be approximately the correct answer for the enhancement of the emission intensity (in the optically thin limit) or for the increase in  $N(\text{C II}^*)$  over that from the gas at normal pressures. On the other hand, if the high pressure regions are located at sites where the photoionizing radiation level is much higher than elsewhere, then the H I concentration is not strongly diminished but the population of the upper C II levels is still very high. Here, the column densities of C II\* could be considerably higher than 5% of the total and the regions that hold this material could emit a substantial amount of radiation.

It is much easier for us to make a quantitative assessment of the enhancement of radiation from the excited levels of C I because the populations of the two upper levels are exactly what we observe. The value of  $f_1$  within the high pressure gas should be about twice that of the normal gas; hence we can expect that the radiation at 492 GHz (609  $\mu\text{m}$ ) seen toward most of the translucent clouds (Heithausen et al. 2001; Bensch et al. 2003) should only be increased by about 10%. We estimate that the value of  $f_2$  in the high pressure gas is about 15 times as large as that in the

low pressure gas, so about 44% of the radiation at 809 GHz (371  $\mu\text{m}$ ) could arise from the high pressure regions.

### 10.5.4. Possible Origins of the High Pressure Gas

As we pointed out in §5, in order to obtain the composite  $f_1$  and  $f_2$  values that we found for the entire survey, the high pressure component had to be a distinct population whose distribution in pressure was well removed from the low pressure material. We demonstrated in Fig. 3 that it could not be a diminishing tail resembling a power law that extends away from the main, low pressure distribution. In the context of turbulence theory, this poses a challenge in the interpretation of the high pressure gas, unless one could propose an explanation for the absence of intermediate mass fractions at pressures between the two extremes.

In order to justify the presence of certain molecules in the ISM that require endothermic reactions for their production, such as  $\text{CH}^+$ , Joulain et al. (1998) proposed the existence of hot gas concentrations within highly confined dissipation regions created by turbulence. From a computer simulation, Pety & Falgarone (2000) found that extraordinary physical conditions could arise in regions that were selected to have special dynamical conditions, such as larger than normal amounts of vorticity or negative divergence. Further studies from theoretical or observational perspectives have been presented by Godard et al. (2009) and Hily-Blant et al. (2008). These investigators concluded that the volume filling factors for these regions are small (a few percent), but not as small as the mass fractions that we reported in §10.5.2. While the intermittent emergence of extreme conditions within highly confined dissipation regions in a turbulent regime is an attractive prospect for explaining our high pressure gas, it must nevertheless satisfy our requirement for a distinct separation from the pressure fluctuations arising from regular turbulent disturbances instead of a continuous, low level extension thereof.

In §8 we showed evidence that the greatest extremes in pressure occurred for gases at unusually large negative velocities, and this interpretation fits in well with the concept that the target stars (and their neighboring stars) play a role. Indeed, an inspection of Table 3 shows that in some di-

rections, several adjacent sight lines all show elevated pressures compared to the typical pressures derived from the full sample. Two prominent examples are stars near or within the Carina and Orion Nebulae. These are dynamically disturbed regions, and they are also regions of significantly enhanced starlight density. This supports the notion that the stars somehow raise the pressures in their surroundings and that high values of  $I/I_0$  indicate both recent, enhanced star formation and a more highly pressurized ISM.

Figure 13 indicates that the quantities  $g_{\text{high}}$  and  $I/I_0$  also seem to be connected to each other. Generally, we can see that cases where  $g_{\text{high}} > 0.2$  appear to require that  $\log(I/I_0) > 0.5$  and that there were very few outcomes that had  $g_{\text{high}} < 0.2$  that had  $\log(I/I_0) > 1.5$ . It is unclear whether the dominant cause for pressurization is from interactions with mass-loss ejecta, small clouds experiencing a photoevaporation “rocket effect” (Bertoldi 1989; Bertoldi & McKee 1990; Bertoldi & Jenkins 1992), or the sudden creation of an H II region, all of which can compress the ambient material and accelerate it toward us. An additional possibility is that H I gas near the stars is heated more strongly by the photoelectric effect from grains (Weingartner & Draine 2001b), which could cause a short-term spike in pressure. While these effects (or combinations thereof) may be the dominant cause for the isolated cases that show large values for  $g_{\text{high}}$ , we still find significant amounts of high pressure material at large positive velocities and even small admixtures of high pressure material at all velocities. These outcomes indicate that other mechanisms unrelated to the target stars may play role as well.

Field et al. (2009) have proposed that the recoil of H atoms following the photodissociation of  $\text{H}_2$  at the edge of a molecular cloud can create an external pressure that helps to confine the cloud. They estimated that at locations where ambient UV field intensity reaches  $I/I_0 \approx 60$  the recoil pressure can be approximately  $1.3 \times 10^5 \text{cm}^{-3} \text{K}$ . (Our  $I/I_0$  is approximately the same as their  $\chi$  intensity parameter.) If this mechanism could increase the thermal pressure in the outer portions of translucent clouds that still have reasonable concentrations of  $\text{H}_2$  and explain the existence of the high pressure component that we observe, we would indeed expect to see a positive relationship

between  $g_{\text{high}}$  and  $I/I_0$ .

Even though the points in Fig. 13 at first glance seem to favor the recoil hypothesis as a possible explanation for the high pressure component, our enthusiasm for accepting this proposition must be tempered by two considerations: (1) our fiducial pressure  $\log(p/k) \gtrsim 5.5$  (a lower limit which is to some degree arbitrary and might be relaxed to a slightly lower level) requires a value for  $I/I_0$  considerably greater than 60, and (2) the correlation seen in Fig. 13 may be a byproduct of some other physical effect that responds to higher than normal intensities and generates the high pressures. For instance, we know from Fig. 8 that values of  $\log(p/k)$  in the low pressure regime are likewise correlated with the intensity of starlight, and the greater influence of intermittent dissipation effects in the more strongly driven turbulence may account for the more conspicuous presence of high pressure gas.

## 11. Summary

We have presented a comprehensive analysis of *HST* UV spectra stored in the MAST archive for 89 stars that were observed with the E140H mode of STIS, with the goal of measuring the populations of the three fine-structure levels of the ground electronic state of neutral carbon atoms in the ISM. The ultimate purpose of these measurements was to synthesize a distribution function for the thermal pressures in gases that mostly represent the cold neutral medium (CNM) in our part of the Galactic disk. This work builds upon a similar study of 21 stars in restricted portions of the sky carried out by JT01 in a special observing program dedicated to this purpose. We have repeated the basic analysis protocol developed by JT01 for unraveling the velocity profiles for carbon atoms in the separate fine-structure levels from the blended features in many different multiplets, but with a few improvements in methodology that are outlined in various subsections within Appendix A.

We interpret most of the variations in the outcomes for thermal pressures to arise from fluctuations caused by interstellar turbulence. Some additional pressure excursions that are large in magnitude but for small mass fractions probably arise from the the random passages of infrequent but strong shocks created by either stellar mass loss

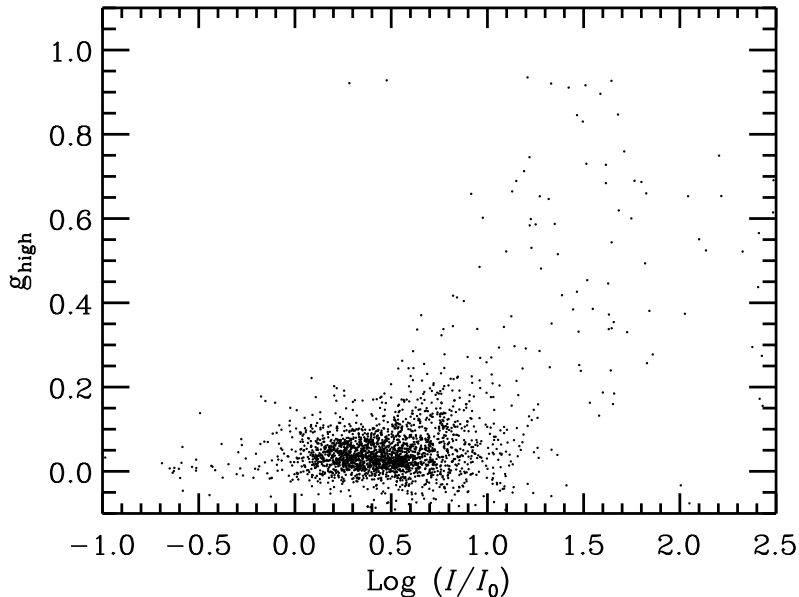


Fig. 13.— The relationship between the fractional amount of high pressure gas,  $g_{\text{high}}$ , and the starlight intensity relative to the Galactic average,  $I/I_0$ .

or supernova explosions.

The following conclusions have emerged from our study of C I fine-structure excitations:

1. The relative populations of the two excited fine-structure levels are influenced in different ways by the local physical conditions, since the levels have significantly different collisional rate constants and energies. This feature allows us to sense in any one velocity channel the presence of admixtures of gas that have markedly different conditions. While there is a multitude of possibilities for explaining any particular combination of level populations, we find that when the data are viewed as a whole, the most straightforward interpretation is that practically all of the gas in the normal range of pressures ( $10^3 \lesssim p/k \lesssim 10^4 \text{cm}^{-3} \text{K}$ ) is accompanied by very small amounts (of order 0.05%) of gas at anomalously large pressures and temperatures ( $p/k > 10^{5.5} \text{cm}^{-3}$ ,  $T > 80 \text{K}$ ). In a small fraction of cases, the proportion of the gas at high pressures is markedly higher

than this level, both because the amount of C I is greater and the local radiation density is high (which makes more of the carbon atoms singly ionized).

2. For a substantial number of our lines of sight, we can make use of molecular hydrogen rotation temperatures  $T_{01}$  between  $J = 0$  and 1 to define the local kinetic temperature. Such temperatures are useful in defining one of the free parameters in solutions for the level populations. As an added benefit, we can explore whether or not, in a general statistical sense, the pressure outcomes are related in some way with such temperatures. We find only a weak anticorrelation, which indicates that pressure fluctuations do not appear to be the dominant cause for temperature changes from one place to the next.
3. Excluding the small amounts of high-pressure gas mentioned earlier, the pressures of most of the CNM material show some correlation with the local radiation densities, as sensed

by the observed ratio of O I (or sometimes S II) to C I followed by an application of the equation of ionization equilibrium with plausible values for O/C and S/C to derive  $N(\text{C II})$ . We interpret this trend as arising from the fact that the stars that create this radiation are sources of enough mechanical energy to make the pressures higher than normal.

4. The main part of the mass-weighted distribution of pressures in our complete sample approximately follows a lognormal distribution with a mean value for  $\log(p/k)$  equal to 3.58 and a standard deviation of 0.175 dex. However, for  $\log(p/k) < 3.2$  or  $> 4.0$  the amount of material is greater than a continuation of the lognormal distribution.
5. In order to sense the distribution of pressures in regions well removed from the sources of mechanical disturbance (i.e., the stars that emit large amounts of radiation), we have isolated for study only those cases where the radiation density is less than  $10^{0.5}$  times the overall average level. Under these circumstances, the tail on the high pressure side of the distribution becomes suppressed, and the remaining distribution develops a negative skewness. We supply a polynomial expression that fits this distribution (Eq. 4) that is shown in Fig. 9. About 23% of the material in this distribution is below the minimum pressure for the thermal equilibrium curve of a static CNM in our part of the Galaxy, suggesting that short-term fluctuations in pressure can occur without the gas being transformed to a stable warm neutral medium (WNM).
6. The thicknesses of the regions that we were able to probe, as measured by the hydrogen column densities divided by their space densities, are generally less than 20 pc. The filling fractions for the sightlines are generally less than 1%. The remaining 99% of a typical sightline is filled with much hotter gas having densities that are far too low to create enough C I for us to measure.
7. We recognize that even with the over-determination of conditions provided by the

two fine-structure levels, we can still underestimate the dispersion of pressures because we are viewing at each velocity an average pressure for the superposition of regions that could have vastly different pressures. We have studied how the dispersions scale in proportion to  $N(\text{C I}_{\text{total}})^{-0.5}$  and find that the ISM could conceivably be composed of independent packets of gas with a true *rms* dispersion in  $\log(p/k)$  that could be as large as 0.5 dex, which is considerably wider than the distribution that we constructed directly from the data. The characteristic column density of each packet would be about  $N(\text{C I}_{\text{total}}) = 2 \times 10^{12} \text{cm}^{-2}$ . However, an alternate interpretation, and one that is quite plausible, is that small volumes of gas have intrinsic pressure variances that are larger than for coherent, larger volumes that might be more resistant to perturbations from turbulent forces. This phenomenon could conceivably produce the same linear scaling of pressure dispersions against  $N(\text{C I}_{\text{total}})^{-0.5}$  that we observed.

8. On the basis of our findings reported in items 4 and 7 above, we derive characteristic turbulent Mach numbers for the C I-bearing gas to range between 0.8 and 4.8. Since the speed of sound is about  $0.5 \text{ km s}^{-1}$  if  $T = 80 \text{ K}$ , we expect that the 3-dimensional velocity dispersion  $\sigma_v$  to range between  $0.40$  and  $2.4 \text{ km s}^{-1}$ . If we equate these numbers to observations of velocity structure functions in the ISM, we find that the characteristic size  $r$  of the clouds or the outer driving scale of the turbulence is probably in the range of approximately  $0.2 < r < 4.7 \text{ pc}$ .
9. Gas with radial velocities well outside the range of motions expected for differential galactic rotation is more likely than usual to exhibit exceptionally large pressures. This link of pressures with kinematics helps to support the interpretation that shocks and turbulence play an important role in creating the positive excursions in pressure. Packets of C I moving at negative velocities show larger pressure excursions than for those at positive velocities. We explain this difference in terms of an observational bias that

favors our viewing the near sides of pressurized shells that are expanding away from our target stars.

10. There is a broad range of time scales that are needed to reach equilibrium values for various quantities and physical processes that are relevant to our study. From the shortest to the longest they are as follows: (1) C I fine-structure level populations (of order 100 days), (2) the balance between C I and C II established by the competition between photoionizations and various means of recombination (160 yr, or shorter if the radiation density is larger than average), (3) the coupling of the  $J = 0$  to 1 rotation temperature of  $\text{H}_2$  to the local kinetic temperature ( $10^4$  yr for typical conditions:  $\log(p/k) = 3.5$  and  $T = 80$  K), and (4) the cooling time for the ISM ( $3 \times 10^4$  yr for the same conditions). We compute the eddy turnover times for turbulent eddies having a radius  $r$  using a relation  $\Delta t = r/\Delta v$  with an extrapolation to small scales  $\Delta v = r_{\text{pc}}^{0.4} \text{km s}^{-1}$ , and we find that the only items of consequence for  $r$  smaller than about 100–1000 AU are (3) and (4). Over these extremely small scales, delays in the adjustments of  $\text{H}_2$  rotation temperatures will give misleading readings for the local kinetic temperatures, but the differences in the two temperatures should be minor, especially since we can use  $T_{01}$  only to indicate an average temperature over many small volumes. Likewise, any lag in the thermal response of the gas will make its polytropic index  $\gamma$  closer to the adiabatic value, rather than matching the slope of the thermal equilibrium curve for the CNM ( $\gamma \approx 0.7$ ). The fact that this may be happening is supported by the negative skewness of our distribution in  $\log(p/k)$ , which indicates that the turbulent fluctuations are consistent with  $\gamma > 1$ .
11. For  $\log p/k$  above 4.0, we find a slope in the relationship between the logarithms of the volume fractions of the gas and  $\log(p/k)$  to be consistent with a power-law slope of  $-14/9$  that is expected for random penetrations of expanding supernova remnants in various stages of development.

This research was supported by program number HST-AR-09534.01-A which was provided by NASA through a grant from the Space Telescope Science Institute (STScI), which is operated by the Association of Universities for Research in Astronomy, Incorporated, under NASA contract NAS5-26555. All of the C I absorption line data that were analyzed for this paper were taken with the NASA/ESA *Hubble Space Telescope* and were downloaded from the Multimission Archive at STScI (MAST). *Facilities:* HST(STIS)

## A. Improvements in the Analysis over that of JT01

Over the time since the publication of our initial survey of thermal pressures (JT01), we have had the benefit of some extra opportunities to recognize various ways to improve our data reduction and analysis methods. In the following subsections, we discuss these new features in our more refined treatments, and we also cover a number of improvements in some basic atomic data that have emerged since the earlier study. We refrain from discussing here all of the fundamentals of how the analysis was carried out; JT01 explained this in some detail.

### A.1. Available Transitions and Minor Modifications of Some $f$ -Values

The observing program of 21 stars carried out by JT01 had a wavelength coverage that included all of the multiplets out of the ground electronic state of C I at wavelengths longward of 1188 Å, except for Multiplet<sup>13</sup> 3 centered at 1561 Å. Their analysis was based on intensity profiles recorded for all of these multiplets, except for a few cases where either the lines were too weak to be useful or suffered interference from other atomic species (see Table 3 of JT01). They adopted a revised set of  $f$ -values for the transitions that gave internally consistent outcomes for their analysis, based on comparisons of optical depths described in §5.3 of their paper.

Some of the observations used in the current study have exceptionally high signal-to-noise ratios. We have made use of these results to further revise (or determine for the first time) the  $f$ -values for some transitions that were too weak to evaluate accurately in the earlier study, again by implementing the analysis of JT01. We list in Table 5 our newly adopted  $f$ -values for the current study. For lines not listed in this table, we used the values given by JT01. New  $f$ -values were also determined for Multiplet 3, which was covered by observations in the archived data but not in our original survey. New  $f$ -values determined here are very similar to those derived by JT01; both sets differ appreciably from ones published in the literature. In Appendix B we describe a special study that supports the validity of both our new and older  $f$ -values.

### A.2. Improved Quantitative Estimates of the Uncertainties

A critical aspect of our study of the thermal pressures is the proper understanding and control of errors, since, if they are large enough, they can mislead us into thinking the distribution function is broader than reality. For this reason, we have instituted a number of improvements in developing quantitative estimates for various sources of error so that we can more reliably screen out measurements of inferior quality and have a better confidence that the remaining errors are inconsequential. The discussions in the following subsections build upon the concepts presented by JT01 (see their Sections 4 and 5).

#### A.2.1. Relative Errors in the Observed Optical Depths

For absorption features that are moderately or very strong, the principal source of uncertainty in any intensity measurement is that produced by random noise fluctuations in the counts of photoevents. In the study of JT01, the effects of these errors were propagated through the analysis, serving as a guide on the most appropriate weight factors for intensities recorded in different multiplets. JT01 also recognized the existence of uncertainties in the adopted background level by using a formula (their Eq. 7) that reduced or eliminated the relative weights of stronger features that came close to zero intensity. For very weak lines, however, systematic uncertainties in the establishment of the continuum level are also important.

In the current study, we now add the continuum uncertainties to the noise errors in quadrature. This has practically no effect for moderately strong features, but it now decreases the relative importance of very weak multiplets in the final solutions. As did JT01, we adopted best fitting Legendre polynomials for the continua at locations somewhat removed from the features. To construct the probable errors in these continua, we evaluate the expected errors in the polynomial coefficients, as described by Sembach & Savage (1992), and

---

<sup>13</sup>Multiplet numbering system from Moore (1970), also adopted by Morton (2003).

TABLE 5  
NEW  $f$ -VALUES<sup>a</sup>

Multiplet <sup>b</sup>	$\lambda$ (Å)	$\log (f\lambda)$
2 .....	1656.267	2.012 <sup>c</sup>
	1656.928	2.392 <sup>c</sup>
	1657.008	2.266 <sup>c</sup>
	1657.379	1.788 <sup>c</sup>
	1657.907	1.914 <sup>c</sup>
	1658.121	1.789 <sup>c</sup>
3 .....	1560.309	2.312
	1560.682	2.187
	1560.709	1.710
	1561.340	1.488
	1561.367	0.311
	1561.438	2.236
7.01 .....	1277.190	-0.021
12 .....	1192.451	0.711
	1192.835	0.129
14 .....	1189.447	1.006
	1189.631	1.246

<sup>a</sup>Changes from values adopted by JT01

<sup>b</sup>Multiplet numbering system from Moore (1970), also adopted by Morton (2003).

<sup>c</sup>Adopted from Morton (2003).

then we multiply them by two in order to make an approximate allowance for additional uncertainties caused by the arbitrariness in selecting the most appropriate polynomial order. From the sizes of residual errors that seem to be extended over broad ranges of velocities where no absorption is evident, this global increase in the estimates for the continuum errors seems to be appropriate.

#### A.2.2. Error Estimates for $N(C I)$ , $N(C I^*)$ , and $N(C I^{**})$

In their Section 5, JT01 discussed the various sources of both random and systematic errors in column densities. They estimated the combined magnitudes from most of these errors by measuring the amplitudes of fluctuations in  $N$  at velocities well removed from obvious C I features. These empirical determinations should be satisfactory for velocities where the amplitudes of the absorptions are small, but they underestimate the errors at locations where the intensity levels are well below the continuum. In these circumstances, noise deviations can create much larger uncertainties in the combined optical depths for different lines within a multiplet, and these enhanced uncertainties propagate their way through to the solutions for the column densities.

We have now implemented evaluations of errors that should apply equally well to both the weak and strong portions of the absorptions. Eq. 6<sup>14</sup> of JT01 was used to construct a design matrix from which least-squares solutions would emerge for the three column densities at each of the different velocities. The inverse of this matrix gives the expected variances and covariances of these variables, as long as there is a proper scaling of the rms errors in all of the optical depths that contribute to the matrix terms. By incorporating the error derivations discussed in the above section (§A.2.1), we believe that our evaluations of the uncertainties in the optical depths  $\sigma_{\tau(i)}$  properly include all effects except for some that are unquantifiable, such as possible detector artifacts, distortions in optical depths caused by unresolved saturated structures (discussed in §A.2.4 below), and errors in the adopted  $f$ -values of the transitions. The magnitudes of the covariances are much smaller than the variances, so the squares of the errors can be extracted simply from the terms in the main diagonal of the inverse matrix.

In order to obtain an approximate validation that the error calculations give reasonable results, we can draw upon three observations of the star HD 219188 taken at different epochs. If we exclude the velocity component that has been identified by Welty (2007) to vary with time, we find that for the expected errors that were calculated according to the prescription given above, the dispersion about the weighted mean of individual observations of column densities at different velocities yielded a  $\chi^2 = 750$  for 536 degrees of freedom. This evaluation was performed after the outcomes with a spacing of  $0.5 \text{ km s}^{-1}$  had been binned by a factor of 3, so that the samples were approximately commensurate with the velocity widths of the detector's pixels. One can surmise from this study that our error calculations probably underestimate the true errors by a factor of approximately  $(536/750)^{\frac{1}{2}} = 0.85$ . There were no obvious differences between the magnitudes of individual  $\chi^2$  outcomes within strong C I absorptions as opposed to those outside the features.

Over velocity intervals where we sense that there is no C I absorption, we detect some very low level, smooth deviations that are still present and that add to the random short-scale noise caused by photon counting statistical variations. These deviations are probably caused by slight inadequacies in the fitting of Legendre polynomials to the true continuum levels, which can exhibit troublesome variations for stars with low projected rotational velocities. These deviations have a relatively minor influence on column densities at specific velocities, but they can contribute nonnegligible errors in  $N(C I_{\text{total}})$  integrated over all velocities, since these errors are coherent from one velocity to the next and thus can build up in a linear fashion. In computing the errors associated with the values of  $N(C I_{\text{total}})$  listed in Table 3 we took such errors into account (by direct addition across velocity channels rather than quadrature sums). We also allowed for the fact that the smaller scale statistical errors were coherent over contiguous stretches of 2.6 velocity channels, which represent the width of a pixel on the STIS ultraviolet detector.<sup>15</sup>

<sup>14</sup>The constant A in this equation should actually be C, where C was defined on the preceding page (and used in Eq. 3).

<sup>15</sup>This channel width should not be confused with the line spread function of the spectrograph, which is about twice as large.



### A.2.3. Errors in $f1$ and $f2$

JT01 used their own judgment in making the choices for velocity ranges over which the C I absorptions were deemed to be strong enough to include in the presentations of  $f1$  and  $f2$ . The existence of a few errant  $f1$  and  $f2$  points in Fig. 7 of JT01 shows that this selection was not ideal. We have thus introduced a more rigorous and quantifiable selection criterion for data which are to be regarded as acceptable.

If we re-express the column densities for C I in the three fine-structure levels as  $N_0 \equiv N(\text{C I})$ ,  $N_1 \equiv N(\text{C I}^*)$ , and  $N_2 \equiv N(\text{C I}^{**})$ , along with a designation for the total column density  $N_{\text{tot}} \equiv N_0 + N_1 + N_2$ , then the uncertainties  $\sigma(N_0)$ ,  $\sigma(N_1)$ ,  $\sigma(N_2)$  contribute to an overall error in  $f1$  in the following manner:

$$\begin{aligned} \sigma(f1) &= \left\{ \left[ \sigma(N_0) \frac{\partial f1}{\partial N_0} \right]^2 + \left[ \sigma(N_1) \frac{\partial f1}{\partial N_1} \right]^2 + \left[ \sigma(N_2) \frac{\partial f1}{\partial N_2} \right]^2 \right\}^{\frac{1}{2}} \\ &= N_{\text{tot}}^{-2} \left\{ \sigma(N_1)^2 [N_{\text{tot}} - N_1]^2 + N_1^2 [\sigma(N_0)^2 + \sigma(N_2)^2] \right\}^{\frac{1}{2}}. \end{aligned} \quad (\text{A1})$$

Likewise,

$$\sigma(f2) = N_{\text{tot}}^{-2} \left\{ \sigma(N_2)^2 [N_{\text{tot}} - N_2]^2 + N_2^2 [\sigma(N_0)^2 + \sigma(N_1)^2] \right\}^{\frac{1}{2}}. \quad (\text{A2})$$

For a determination of  $f1$  and  $f2$  at any particular velocity, we insisted that in order to be considered, both of their  $1\sigma$  errors had to be less than 0.03.

### A.2.4. Sensing Possible Distortions Caused by Unresolved Saturated Portions of the Absorption Profiles

Even though the spectra considered here had a minimum wavelength resolving power  $R = \lambda/\Delta\lambda = 114,000$  for the E140H grating with the standard entrance slit<sup>16</sup> (Proffitt et al. 2010), there remains a possibility that for some cases we will encounter collections of unresolved, saturated absorption features. In such situations, the apparent optical depths will underestimate the true optical depths after instrumental smoothing. One can normally detect this condition by noting that strong lines show smaller column densities than weaker ones and then applying a correction scheme proposed by Jenkins (1996). Here, however, the correction is no longer straightforward because the individual apparent optical depths lose their identity after they have undergone the transformations that are needed to unravel the overlaps of C I, C I\*, and C I\*\* absorptions in each multiplet.

While we were unable to perform corrections to restore the apparent optical depths to their true (but smoothed) values, we could nevertheless detect circumstances where the representations are likely to be inaccurate. The implementation of Eq. 7 of JT01 serves to limit the influence of stronger lines that have low residual intensities. By varying the threshold intensity parameter  $I_t$  in this equation, we can shift the response of the solutions for the column densities either toward or away from the stronger lines. In so doing, if we find that the column density solutions change, we can surmise the outcomes are not stable and that distortions are indeed happening. For adopting or rejecting a set of column densities at any given velocity, we adopted the following test: If any column density derived using twice the standard value for  $I_t$  (see JT01 §5.2.1) came out to be more than 1.2 times that derived from the standard  $I_t$ , we considered the distortion to be unacceptably large and the result for the particular velocity was rejected. Otherwise, deviations less than the factor of 1.2 were deemed to be acceptable. Stars for which the optical depth distortions seemed to be evident are identified in Table 3 (see note *a* of the table for details).

## A.3. New Atomic Physics Parameters

With the passage of time, re-evaluations of atomic parameters are carried out (and we presume that they are better than the older ones). Since the time of publication of our earlier results (JT01), new reaction rates

<sup>16</sup> $R = 200,000$  for the narrow entrance slit and half-pixel intensity sampling used for the stars observed by JT01.

for the excitation of the excited fine-structure levels of C I and O I by atomic hydrogen have been published by Abrahamsson et al. (2007). We have incorporated these new rates into our interpretations of densities and temperatures from the C I level populations. (The O I excitations are discussed in Appendix B.) Rates for other collision partners are the same as those adopted by JT01. Also, we have now replaced the old spontaneous radiative decay rates for the excited levels of the two neutral species by those given by Galavís et al. (1997).

The effect of these changes is that for the representative conditions  $\log(p/k) = 3.6$  and  $T = 80$  K the derived values of the thermal pressure increase by 0.05 dex above what we would have obtained from the older numbers used by JT01.

#### A.4. Revised Optical Pumping Rates

As pointed out by de Boer & Morton (1974), the ultraviolet transitions from the C I electronic ground state that can be used to measure the column densities of this atom also act to populate the upper fine-structure levels through optical pumping by the ambient starlight radiation field. While this effect is usually small compared to the excitations by collisions, it nevertheless is a process that should not be ignored since there are occasions when the starlight field can be found to be considerably above average. Jenkins & Shaya (1979) calculated the rates of optical pumping for the average level of starlight radiation computed by Jura (1975a, b) and Witt & Johnson (1973). These rates were used by JT01.

Our current analysis of the effects of starlight presented in §4.1 adopts as a standard the more recent average radiation intensity  $I_0(\lambda)$  specified by Mathis et al. (1983). Here, we used our ionization equilibrium calculations for carbon atoms to determine the local starlight intensities in terms of a multiplier  $I/I_0$  times this field strength. In order to make our analysis consistent with the new standard intensity, and also to be consistent with our new  $f$ -values for the C I transitions, we have recomputed the matrix for the pumping rates between the different fine-structure levels. This new matrix, presented in Table 6 [cf. Table 3 of Jenkins & Shaya (1979)], expresses the transition rates expected for the standard field density. For every measurement of C I and its fine-structure populations, we adjusted the pumping rates in proportion to the corresponding value of  $I/I_0$  – see §6.

Our application of the new pumping matrix overlooks two effects that can modify the the pumping rates in opposite directions. First, we have ignored weak C I transitions at wavelengths shorter than 1188 Å. An approximate compensation for this is our neglect of the self shielding of the stronger transitions deep inside some of the most strongly absorbing clouds.

The overall effect in implementing the revised pumping rates is to raise the median pressure by about 0.05 dex for most of the C I data. For measurements that apply to cases where  $I/I_0 < 10^{0.5}$ , as shown in Fig. 9, the change is almost negligible.

## B. A Validation of our Previous Determinations of the C I $f$ -Values

One aspect of our earlier study (JT01) of interstellar C I that is highly relevant to the work done here was our re-evaluation of the relative  $f$ -values of the C I lines (for all three fine-structure levels) from one multiplet to the next. Initially, we found that the  $f$ -values given in the literature did not yield self consistent outcomes for the predicted line strengths, after we had derived preliminary values of the C I, C I\* and C I\*\* column densities. As a result, we derived a new set of  $f$ -values that gave the best internal consistencies for the strengths of the lines for all of the targets collectively. These relative  $f$ -values were based on the 1656 Å multiplet as a calibration, in our belief that theoretical calculations of the strength of lines in this strong multiplet were probably the most reliable.

TABLE 6  
 NEW OPTICAL PUMPING RATES BETWEEN THE C I FINE-STRUCTURE LEVELS ( $10^{-10}\text{s}^{-1}$ )<sup>a</sup>

Initial $J$	Final $J$		
	0	1	2
0.....	...	5.06	3.99
1.....	1.69	...	5.23
2.....	0.08	3.14	...

<sup>a</sup>Computed for an optically thin medium in the presence of an average ultraviolet radiation field density in the ISM at a Galactocentric radius of 10 kpc, as specified by Mathis et al. (1983).

Our revised  $f$ -values showed a steady divergence from the earlier, published ones as the lines became successively weaker. For each  $-1$  dex change in a published line strength  $\log f \lambda_{\text{pub.}}$ , the discrepancy  $\log f \lambda_{\text{JT01}} - \log f \lambda_{\text{pub.}}$  increased by about  $+0.3$  dex (see Fig. 3 of JT01). More recent determinations of C I  $f$ -values have been compiled by Froese Fischer & Tachiev (2004) (henceforth FT04). A plot of these newer values against those derived by JT01 still shows the divergence seen in Fig. 3 of JT01, but with less scatter in the individual points representing the weakest lines. Henceforth, we will adopt the values of FT04 as a proxy for  $f$ -values determined by investigators other than JT01.

In our earlier study, we recognized that the sense of the divergence was consistent with the possibility that we could have been misled by the underrepresentations of smoothed optical depths for the most saturated portions of the strong lines (while at the same time, optical depths of the weak absorptions would be properly measured). Such an effect can occur when the lines have very narrow component structures that are saturated and unresolved by the spectrograph (Savage & Sembach 1991; Jenkins 1996), and indeed this seems to happen in some cases – see note *a* in Table 3.

To overcome our worry about these possible distortions in the apparent optical depths, we carried out a number of investigations that indicated that they were unlikely to be the explanation for the divergence that we found (see the discussion in Section 5.3.2 of JT01). Nevertheless, it is still troubling that theoretical and experimental derivations of the C I  $f$ -values by different investigators, such as those cited by Morton (Morton 2003), consistently gave results that disagreed with the values derived by JT01. Recent evidence that interstellar absorption features arising from neutral atoms can occasionally exhibit extraordinarily low turbulent velocity dispersions (Dunkin & Crawford 1999; Price et al. 2001; Knauth et al. 2003; Meyer et al. 2006) reinforces our concerns about possible misrepresentations of averaged true optical depths. If nearly all of the C I absorptions that we observed consisted of clusters of needle-like features that had velocity dispersions  $b \lesssim 0.4 \text{ km s}^{-1}$  created by low temperatures and low turbulent (or shear) velocities, and they are separated<sup>17</sup> by more than about  $2.5b$ , we could have in principle erroneously introduced systematic errors that could explain the observed differences between our  $f$ -values and the published ones, even though the lines were observed at a wavelength resolving power  $R = 200,000$  (see Appendix A of JT01). This phenomenon would have had to operate in a consistent fashion from one case to the next, since we almost always found reconstructed profiles (using our  $f$ -values) to show good agreement with the observations of both strong and weak lines. The uniform persistence of this misrepresentation effect seems rather unlikely, but we have no grounds for saying that it is completely impossible.

We now present a single example that disproves the proposition that our results were incorrect because we were continually misled by narrow substructures in the profiles. The substance of our argument is that for one special case we can compare the observed and predicted absorption features from a velocity complex for which the values of  $b$  caused by thermal Doppler broadening for any subcomponents must not be very much less than the resolution of the STIS spectrograph.

A cluster of absorption profiles with a peak at about  $-34 \text{ km s}^{-1}$  toward HD 210839 ( $\lambda$  Cep) is unusual because it shows exceptionally strong features from O I\* and O I\*\*, as shown in Fig. 14, and the C I fine-structure excitation indicates that it is at an unusually high pressure. The ratio  $n(\text{O I}^*)/n(\text{O I}^{**})$  is a good indicator of the local kinetic temperature of the gas. Figure 15 shows how this ratio should vary with temperature. This relationship follows from solutions for the equilibrium equation based on the H I collision rate constants as a function of temperature given by Abrahamsson et al. (2007)<sup>18</sup> and the radiative decay rates of Galavís et al. (1997). We find from the absorptions produced by the  $1304.86 \text{ \AA}$  and  $1306.03 \text{ \AA}$  transitions that over the velocity interval  $-40 < v < -20 \text{ km s}^{-1}$ ,  $\log N(\text{O I}^*) = 13.410 \pm 0.018$  and  $\log N(\text{O I}^{**}) = 13.359 \pm 0.023$ . The nominal value of 1.12 for the ratio of the two is shown by the lower of the two horizontal dashed lines in Fig. 15, while the other dashed line just above it indicates our

<sup>17</sup>Narrow features that have small separations and thus are partly blended are of no concern, since they behave much like features with much larger  $b$  values.

<sup>18</sup>Abrahamsson et al. did not list rates for  $T > 1000 \text{ K}$ . The collision rate constants that we needed for  $T$  somewhat above  $1000 \text{ K}$  are simply extrapolations from their values just below  $1000 \text{ K}$ .

estimate of 1.35 for an upper limit based on the  $+2\sigma$  error for  $N(\text{O I}^*)$  and  $-2\sigma$  limit for  $N(\text{O I}^{**})$ . It follows that our favored value for  $T$  is 390 K, and our most conservative (i.e., low) value is 200 K, both of which are substantially lower than an upper limit  $T < 660$  K based on a fit that gave  $b = 0.53 \text{ km s}^{-1}$  for the strongest component of the K I line in this same velocity complex observed at a resolving power of  $0.56 \text{ km s}^{-1}$  (FWHM) by Welty & Hobbs (2001). (The weaker K I component at a more positive velocity yielded a  $b$  value that indicated that  $T < 1550$  K.) Since the thermal Doppler broadening for  $T = 390$  K is expected to yield a value for  $b$  of only  $0.41 \text{ km s}^{-1}$ , there is either some extra broadening due to turbulence or the profiles might be split into even smaller separate components that were not resolved by Welty & Hobbs.

One might argue that the near agreement of the O I\* and O I\*\* column densities could arise from these features themselves being strongly influenced by unresolved, saturated absorption spikes within the velocity complex. Extreme saturations of this sort would tend to deceive us into deriving nearly the same column densities for the two species. However, we can test for this by examining weaker features from the 1040 Å multiplet covered by the *Far Ultraviolet Spectroscopic Explorer* (*FUSE*). One such spectrum of HD 210839 is available in the MAST archive. No absorption by the O I\* 1040.94 Å transition is readily apparent in the spectrum; a formal measurement of the equivalent width over the appropriate velocity range yields  $0.8 \pm 1.3 \text{ mÅ}$ . For the column density of O I\* that we derived, one would have expected to find  $W_\lambda(1040.94 \text{ Å}) = 2.2 \pm 0.1 \text{ mÅ}$ . If we had underestimated  $N(\text{O I}^*)$  because the 1304.86 Å feature had hidden saturation, the equivalent width of the weaker feature in the *FUSE* spectrum would have been larger than this expectation. We are unable to perform the same test for O I\*\* because the 1041.69 Å feature suffers from interference from the Lyman 6–0 R(6) transition of H<sub>2</sub> at nearly the same wavelength.

A separate argument that disfavors a strong internal saturation of the 1304.86 Å feature and a less strong effect with the 1306.03 Å feature is that the shapes of the two absorptions do not differ from each other appreciably. If anything, the O I\* absorption seems more strongly peaked in the center, an effect opposite

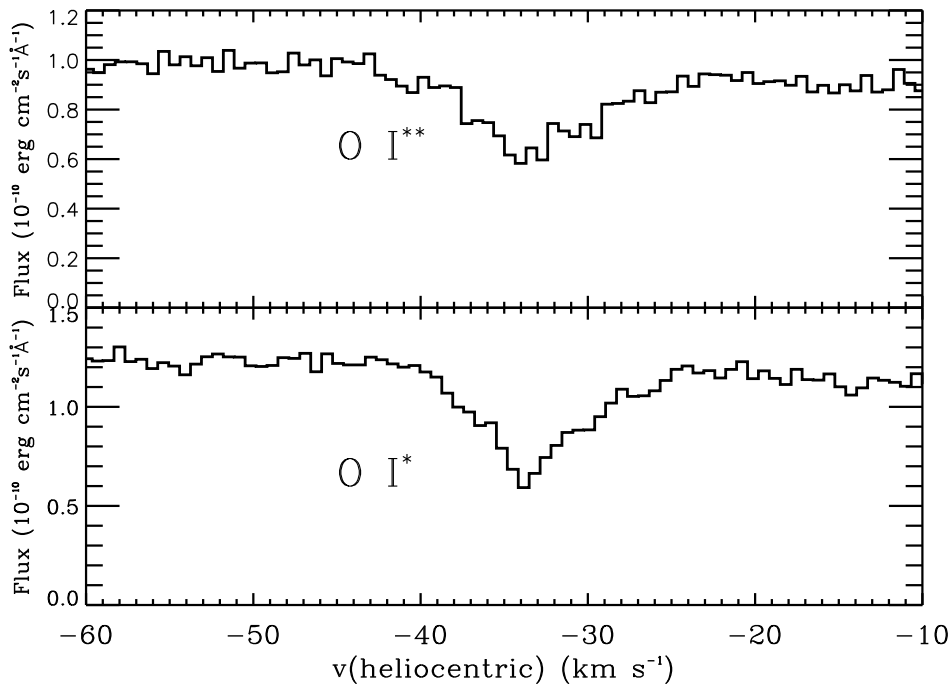


Fig. 14.— Absorption profiles (unnormalized) of O I\*\*  $\lambda 1306$  (*top panel*) and O I\*  $\lambda 1304$  (*bottom panel*) in the spectrum of HD 210839.

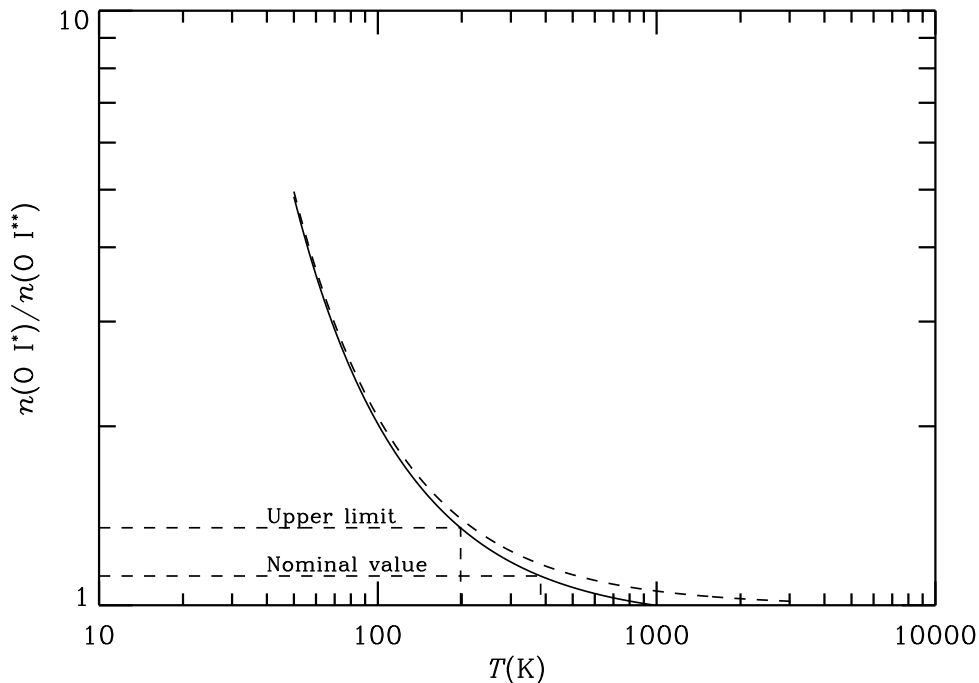


Fig. 15.— The expected ratio of  $n(\text{O I}^*)/n(\text{O I}^{**})$  for collisions in an environment where  $n(\text{H I}) \leq 100 \text{ cm}^{-3}$  (*solid curve*) and  $n(\text{H I}) = 1000 \text{ cm}^{-3}$  (*dashed curve*). For the velocity component at  $-34 \text{ km s}^{-1}$  in front of  $\lambda$  Cep, our nominal value and upper limit for  $N(\text{O I}^*)/N(\text{O I}^{**})$  are indicated by the horizontal dashed lines, and the temperatures  $T = 200$  and  $390 \text{ K}$  that apply to these values are shown by the vertical dashed lines.

to an expectation that saturation could be occurring in the strongest part of the profile. This effect might indicate the presence of slightly cooler gas at velocities very near the central velocity of  $-34 \text{ km s}^{-1}$  (the ratio of apparent optical depths at this central point is 1.42, which would indicate  $T \approx 120 \text{ K}$  if we were to use the curve shown in Fig. 15).

Returning to the topic of subcomponents within the C I, C I\* and C I\*\* profiles, for our conservative lower limit  $T = 200 \text{ K}$  we expect the Doppler broadening to produce a  $b$  value for carbon atoms of at least  $0.53 \text{ km s}^{-1}$ , which is somewhat less than the STIS instrumental profile function with  $b = 0.90 \text{ km s}^{-1}$  (if its shape is Gaussian). We can build a model of this complex composed of separate components, each with  $b = 0.53 \text{ km s}^{-1}$ , on top of a low amplitude, broad shoulder. This model has been tailored such that, after it has been smoothed by the STIS instrumental spread function, it duplicates exactly the shape of the C I\* profile that we derived. It also creates structures that are consistent with the 3 K I component parameters derived by Welty & Hobbs (2001), after we acknowledge the fact that the thermal broadening of the K I should be less than that for C I.

If we could have resolved the partly blended complex of profiles perfectly, we would have found that the apparent optical depth  $\tau_a(v)$  [in this case equal to the true optical depth  $\tau(v)$ ] divided by  $f\lambda$  of the transition should remain constant for different transitions at all velocities  $v$ , regardless of line strength. However, after the profile function has been smoothed by the instrumental profile, there can in principle be some violation of this equality. Our model was constructed in a manner to create the worst conceivable situation that would aggravate this violation, i.e., we adopted the lower limit for  $T$  instead of the nominal one, and we assumed the measurable broadening of profiles seen in the C I and K I spectra, beyond the instrumental smoothing,

was created by clusters of narrow profiles rather than a smooth turbulent broadening. This conservative model indicates that as the value of  $f\lambda$  increases by one order of magnitude from 5 to 50, which corresponds to peak values of  $\tau(v)$  equal to 0.24 and 2.4, respectively, the average discrepancy in  $\tau_a/f\lambda$  over the strongest portions of the profile ( $-36 < v < -28 \text{ km s}^{-1}$ ) is only 0.041 dex. This is only about 13% of the observed rate of divergence between our  $f$ -values and those that have been published elsewhere.

We have demonstrated the expected insignificance of misrepresentations reflected by  $\tau_a$  when progressing from very weak absorptions to absorptions of moderate strength (10 times stronger), where we consider  $\tau_a$  to be simply an instrumentally smoothed version the real optical depth  $\tau$ . Moving on, we are now in a position to interpret comparisons between the observed absorption features and ones that are reconstructed from our derived column densities vs. velocity, on the assumption that the computed values of  $\tau_a$  give the correct residual intensities (to within about 0.041 dex). The different displays in Fig. 16 show this comparison for the complex at  $-34 \text{ km s}^{-1}$  for both the  $f$ -values derived by JT01 and those listed by Froese Fischer & Tachiev (2004) (FT04). We have restricted the choices in this display to transitions of C I\*, and we have rejected cases where there was interference from other transitions that had absorptions from other, less negative velocity components that were overlapping. It is clear that as the lines become weaker, the disparity between the observations and the predictions using the FT04  $f$ -values increases, while those using the JT01  $f$ -values match the observations to within the noise levels in each case.

It is important to emphasize that the investigation discussed here addresses the accuracy of the relative  $f$ -values from one multiplet to the next and not the correctness of all of the multiplets taken together. Had we adopted a multiplet other than the strongest one at  $1657 \text{ \AA}$  as a standard, all of our derived  $f$ -values would have been lower by some constant factor.

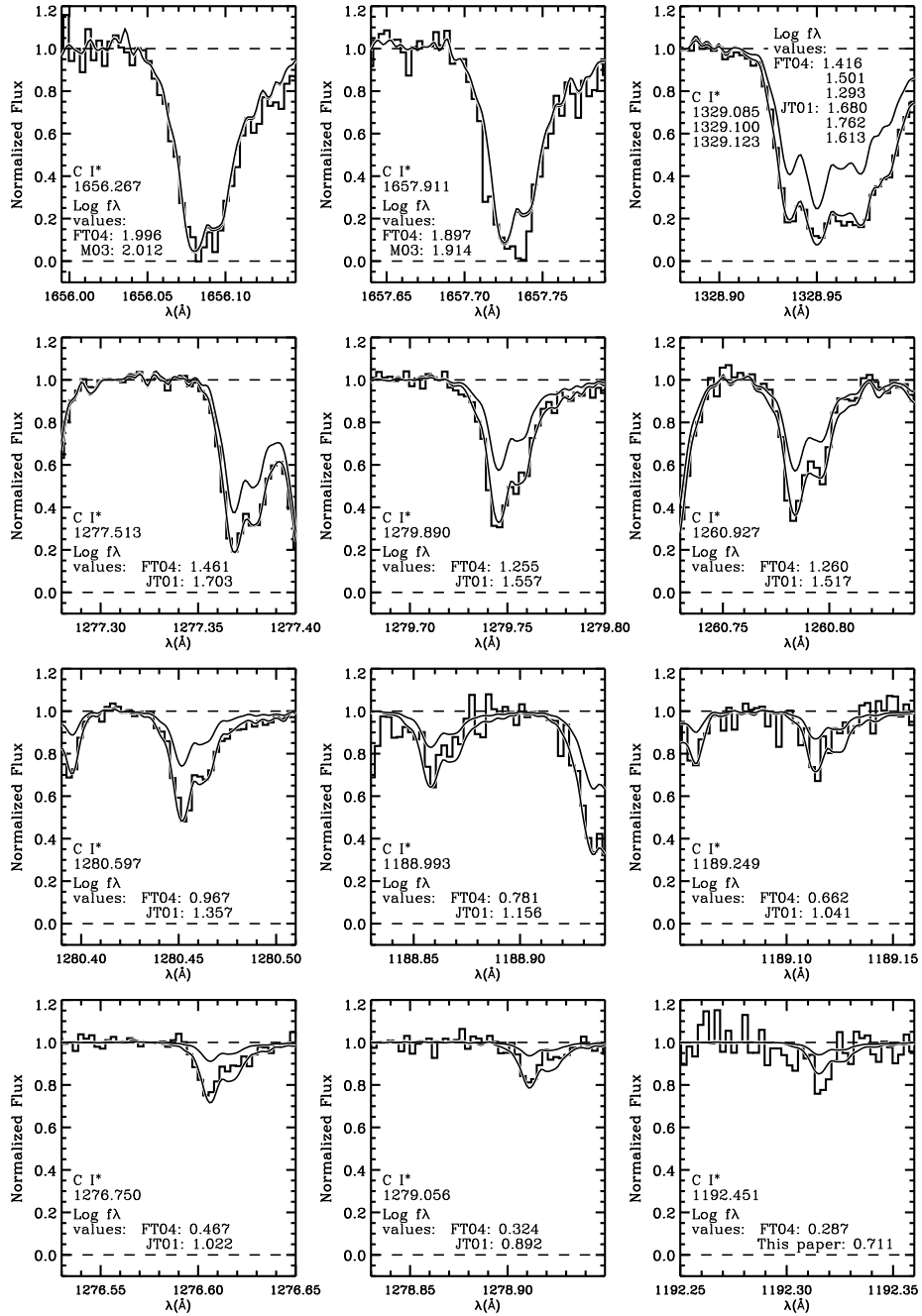


Fig. 16.— Selected absorptions from the  $-34 \text{ km s}^{-1}$  C I\* component in the spectrum of HD 210839 ( $\lambda$  Cep) that are not contaminated by overlapping features created by the components between  $-20$  and  $0 \text{ km s}^{-1}$ . The observed fluxes (*histogram-style traces*) have been normalized to our best estimate for the continuum level in each case. The different panels are ordered in a sequence of decreasing values of  $\log(f\lambda)$  determined by JT01. The upper smooth curve in each panel represents a reconstruction of the profile using the published  $f$ -value, while the lower curve arises from the  $f$ -value derived by JT01. [Key to published  $f$ -value sources: M03 = Morton (2003), FT04 = Froese Fischer & Tachiev (2004).]



## REFERENCES

- Abbott, D. C. 1982, *ApJ*, 263, 723
- Abrahamsson, E., Krems, R. V., & Dalgarno, A. 2007, *ApJ*, 654, 1171
- André, M., et al. 2003, *ApJ*, 591, 1000
- Audit, E., & Hennebelle, P. 2005, *A&A*, 433, 1  
— 2010, *A&A*, 511, A76
- Ballesteros-Paredes, J., Vázquez-Semadeni, E., & Scalo, J. 1999, *ApJ*, 515, 286
- Bally, J. 2007, *Ap&SS*, 311, 15
- Bensch, F., Leenhagen, U., Stutzki, J., & Schieder, R. 2003, *ApJ*, 591, 1013
- Bergin, E. A., Hartmann, L. W., Raymond, J. C., & Ballesteros-Paredes, J. 2004, *ApJ*, 612, 921
- Bertoldi, F. 1989, *ApJ*, 346, 735
- Bertoldi, F., & Jenkins, E. B. 1992, *ApJ*, 388, 495
- Bertoldi, F., & McKee, C. F. 1990, *ApJ*, 354, 529
- Bohlin, R. C., Savage, B. D., & Drake, J. F. 1978, *ApJ*, 224, 132
- Boldyrev, S., Nordlund, A., & Padoan, P. 2002, *ApJ*, 573, 678
- Boulares, A., & Cox, D. P. 1990, *ApJ*, 365, 544
- Bowen, D. V., et al. 2008, *ApJS*, 176, 59
- Brandenburg, A., Korpi, M. J., & Mee, A. J. 2007, *ApJ*, 654, 945
- Brunt, C. M. 2010, *A&A*, 513, A67
- Brunt, C. M., & Heyer, M. H. 2002a, *ApJ*, 566, 276  
— 2002b, *ApJ*, 566, 289
- Brunt, C. M., & Kerton, C. R. 2002, *ApJ*, 567, L41
- Burgh, E. B., France, K., & McCandliss, S. R. 2007, *ApJ*, 658, 446
- Burgh, E. B., France, K., & Jenkins, E. B. 2010, *ApJ*, 708, 334
- Burkert, A., & Lin, D. N. C. 2000, *ApJ*, 537, 270
- Castor, J. C., McCray, R., & Weaver, R. 1975, *ApJ*, 200, L107
- Cecchi-Pestellini, C., Casu, S., & Dalgarno, A. 2005, *MNRAS*, 364, 1309
- Chamblaud, G., Launay, J. M., Levy, B., Millie, P., Roueff, E., & Tran Minh, F. 1980, *J. Phys. B*, 13, 4205
- Chandrasekhar, S., & Münch, G. 1952, *ApJ*, 115, 103
- Chevalier, R. A. 1977, *ARA&A*, 15, 175
- Cox, D. P., & Smith, B. W. 1974, *ApJ*, 189, L105
- de Avillez, M. A., & Breitschwerdt, D. 2005a, *A&A*, 436, 585  
— 2005b, *ApJ*, 634, L65
- de Boer, K. S., & Morton, D. C. 1974, *A&A*, 37, 305
- Draine, B. T. 1978, *ApJS*, 36, 595
- Dunkin, S. K., & Crawford, I. A. 1999, *MNRAS*, 302, 197
- Elmegreen, B. G., & Scalo, J. 2004, *ARA&A*, 42, 211
- Falgarone, E., Pety, J., & Hily-Blant, P. 2009, *A&A*, 507, 355
- Falgarone, E., Puget, J.-L., & Pérault, M. 1992, *A&A*, 257, 715
- Federrath, C., Klessen, R. S., & Schmidt, W. 2008, *ApJ*, 688, L79
- Federrath, C., Roman-Duval, J., Klessen, R. S., Schmidt, W., & Mac Low, M.-M. 2010, *A&A*, 512, A81
- Field, G. B. 1965, *ApJ*, 142, 531
- Field, G. B., Blackman, E. G., & Keto, E. R. 2009, arXiv:0904.4077v3 [astro.ph.GA]
- Field, G. B., Goldsmith, D. W., & Habing, H. J. 1969, *ApJ*, 155, L149
- Field, G. B., & Steigman, G. 1971, *ApJ*, 166, 59
- Froese Fischer, C., & Tachiev, G. 2004, <http://atoms.vuse.vanderbilt.edu>
- Galavís, M. E., Mendoza, C., & Zeippen, C. J. 1997, *A&AS*, 123, 159
- Gerlich, D. 1990, *J. Chem. Phys.*, 92, 2377
- Godard, B., Falgarone, E., & Pineau des Forêts, G. 2009, *A&A*, 495, 847
- Heithausen, A. 1996, *A&A*, 314, 251  
— 2004, *ApJ*, 606, L13  
— 2006, *A&A*, 450, 193

- Heithausen, A., Weiss, A., Kerp, J., & Fritz, T. 2001, *ApJ*, 561, 238
- Heyer, M. H., & Brunt, C. M. 2004, *ApJ*, 615, L45
- Hily-Blant, P., Falgarone, E., & Pety, J. 2008, *A&A*, 481, 367
- Indriolo, N., Geballe, T. R., Oka, T., & McCall, B. J. 2007, *ApJ*, 671, 1736
- Inoue, T., Inutsuka, S., & Koyama, H. 2006, *ApJ*, 652, 1331
- Jenkins, E. B. 1996, *ApJ*, 471, 292
- 2002, *ApJ*, 580, 938
- 2009, *ApJ*, 700, 1299
- Jenkins, E. B., Jura, M., & Loewenstein, M. 1983, *ApJ*, 270, 88
- Jenkins, E. B., & Shaya, E. J. 1979, *ApJ*, 231, 55
- Jenkins, E. B., Silk, J., Wallerstein, G., & Leep, E. M. 1981, *ApJ*, 248, 977
- Jenkins, E. B., & Tripp, T. M. 2001, *ApJS*, 137, 297
- Jenkins, E. B., & Wallerstein, G. 1995, *ApJ*, 440, 227
- Jenkins, E. B., Wallerstein, G., & Silk, J. 1984, *ApJ*, 278, 649
- Jenkins, E. B., et al. 1998, *ApJ*, 492, L147
- Jensen, A. G., Snow, T. P., Sonneborn, G., & Rachford, B. L. 2010, *ApJ*, 711, 1236
- Joulain, K., Falgarone, E., Pineau Des Forêts, G., & Flower, D. 1998, *A&A*, 340, 241
- Jura, M. 1975a, *ApJ*, 197, 581
- 1975b, *ApJ*, 197, 575
- Kahn, F. D. 1969, *Physica*, 41, 172
- Kim, J., Balsara, D., & Mac Low, M.-M. 2001, *J. Korean Astr. Soc.*, 34, S333
- Kimble, R. A. et al. 1998, *ApJ*, 492, L83
- Knauth, D. C., Federman, S. R., & Lambert, D. L. 2003, *ApJ*, 586, 268
- Koyama, H., & Inutsuka, S. 2006, *astro-ph/0605528*
- Kritsuk, A., & Norman, M. L. 2002a, *ApJ*, 580, L51
- Kritsuk, A. G., & Norman, M. L. 2002b, *ApJ*, 569, L127
- Kritsuk, A. G., Norman, M. L., Padoan, P., & Wagner, R. 2007, *ApJ*, 665, 416
- Langer, W. D., Velusamy, T., Pineda, J. L., Goldsmith, P. F., Li, D., & Yorke, H. W. 2010, *A&A*, 521, L17
- Larson, R. B. 1979, *MNRAS*, 186, 479
- 1981, *MNRAS*, 194, 809
- Lasker, B. M. 1967, *ApJ*, 149, 23
- Lee, D.-H., Pak, S., Dixon, W. V., & van Dishoeck, E. F. 2007, *ApJ*, 655, 940
- Lehner, N., Wakker, B. P., & Savage, B. D. 2004, *ApJ*, 615, 767
- Lemaster, M. N., & Stone, J. M. 2008, *ApJ*, 682, L97
- Li, Y., Klessen, R. S., & Mac Low, M.-M. 2003, *ApJ*, 592, 975
- Lodders, K. 2003, *ApJ*, 591, 1220
- Mac Low, M.-M., Balsara, D. S., Kim, J., & de Avillez, M. A. 2005, *ApJ*, 626, 864
- Mac Low, M.-M., & Klessen, R. S. 2004, *RMP*, 76, 125
- Mac Low, M.-M., McCray, R., & Norman, M. L. 1989, *ApJ*, 337, 141
- Mathis, J. S., Mezger, P. G., & Panagia, N. 1983, *A&A*, 128, 212
- McCray, R., & Snow, T. P. 1979, *ARA&A*, 17, 213
- McKee, C. F., & Ostriker, E. C. 2007, *ARA&A*, 45, 565
- McKee, C. F., & Ostriker, J. P. 1977, *ApJ*, 218, 148
- McKee, C. F., Van Buren, D., & Lazareff, B. 1984, *ApJ*, 278, L115
- Meyer, D. M., Lauroesch, J. T., Heiles, C., Peek, J. E. G., & Engelhorn, K. 2006, *ApJ*, 650, L67
- Moore, C. E. 1970, *Selected Tables of Atomic Spectra*, (NSRDS-NBS, 3, Sec. 3), (Washington: U.S. Dept. of Commerce)
- Morton, D. C. 2003, *ApJS*, 149, 205
- Neufeld, D. A. et al. 2010, *A&A*, 521, L10
- Nichols, J. S., & Slavin, J. D. 2004, *ApJ*, 610, 285
- Nordlund, A., & Padoan, P. 1999, in *Interstellar Turbulence*, ed. J. Franco & A. Carramiñana (Cambridge: Cambridge Univ.), p. 218

- Oort, J. H., & Spitzer, L. 1955, *ApJ*, 121, 6
- Owocki, S. P. 1999, in *Interstellar Turbulence*, ed. J. Franco & A. Carraminana (Cambridge: Cambridge U. Press), p. 79
- Padoan, P., Jones, B. J. T., & Nordlund, A. P. 1997a, *ApJ*, 474, 730
- Padoan, P., Nordlund, A., & Jones, B. J. T. 1997b, *MNRAS*, 288, 145
- Pan, K., Federman, S. R., Sheffer, Y., & Andersson, B.-G. 2005, *ApJ*, 633, 986
- Passot, T., & Vázquez-Semadeni, E. 1998, *Phys. Rev. E*, 58, 4501
- Peters, T., Banerjee, R., & Klessen, R. S. 2008, *Physica Scripta*, T132, 014026
- Pety, J., & Falgarone, E. 2000, *A&A*, 356, 279
- Pineda, J. L., Velusamy, T., Langer, W. D., Goldsmith, P. F., Li, D., & Yorke, H. W. 2010, *A&A*, 521, L19
- Pinotek, R. A., & Ostriker, E. C. 2004, *ApJ*, 601, 905
- Prasad, S. S., & Huntress, W. T. 1980, *ApJS*, 43, 1
- Price, R. J., Crawford, I. A., Barlow, M. J., & Howarth, I. D. 2001, *MNRAS*, 328, 555
- Proffitt, C. et al. 2010, *STIS Instrument Handbook for Cycle 18*, (Baltimore: STScI)
- Rachford, B. L., et al. 2002, *ApJ*, 577, 221
- Rachford, B. L., et al. 2009, *ApJS*, 180, 125
- Reid, M. J., et al. 2009, *ApJ*, 700, 137
- Roberts, W. W., Roberts, M. S., & Shu, F. H. 1975, *ApJ*, 196, 381
- Robitaille, J.-F., Joncas, G., & Khalil, A. 2010, *MNRAS*, 405, 638
- Rodríguez-Gaspar, J. A., & Tenorio-Tagle, G. 1998, *A&A*, 331, 347
- Sakamoto, S. 2002, *ApJ*, 565, 1050
- Sakamoto, S., & Sunada, K. 2003, *ApJ*, 594, 340
- Santillán, A., Franco, J., Martos, M., & Kim, J. 1999, *ApJ*, 515, 657
- Santillán, A., Sánchez-Salcedo, F. J., & Franco, J. 2007, *ApJ*, 662, L19
- Savage, B. D., Bohlin, R. C., Drake, J. F., & Budich, W. 1977, *ApJ*, 216, 291
- Savage, B. D., & Sembach, K. R. 1991, *ApJ*, 379, 245
- Scalo, J. 1999, *ApJ*, 525C, 476
- Scalo, J., & Elmegreen, B. G. 2004, *ARA&A*, 42, 275
- Sembach, K. R., & Savage, B. D. 1992, *ApJS*, 83, 147
- Sheffer, Y., Rogers, M., Federman, S. R., Abel, N. P., Gredel, R., Lambert, D. L., & Shaw, G. 2008, *ApJ*, 687, 1075
- Shetty, R., Collins, D. C., Kauffmann, J., Goodman, A. A., Rosolowsky, E. W., & Norman, M. L. 2010, *ApJ*, 712, 1049
- Shull, J. M., & Van Steenberg, M. 1982, *ApJS*, 48, 95
- Silva, A. I., & Viegas, S. M. 2002, *MNRAS*, 329, 135
- Smith, A. M., Bruhweiler, F. C., Lambert, D. L., Savage, B. D., Cardelli, J. A., Ebbets, D. C., Lyu, C.-H., & Sheffer, Y. 1991, *ApJ*, 377, L61
- Sofia, U. J., Fitzpatrick, E. L., & Meyer, D. M. 1998, *ApJ*, 504, L47
- Sofia, U. J., Lauroesch, J. T., Meyer, D. M., & Cartledge, S. I. B. 2004, *ApJ*, 605, 272
- Sofia, U. J., Parvathi, V. S., Babu, B. R. S., & Murthy, J. 2011, *AJ*, 141, 22
- Stancil, P. C., Schultz, D. R., Kimura, M., Gu, J.-P., Hirsch, G., & Buenker, R. J. 1999, *A&AS*, 140, 225
- Stutzki, J., Stacey, G. J., Genzel, R., Harris, A. I., Jaffe, D. T., & Lugten, J. B. 1988, *ApJ*, 332, 379
- Sun, Y., & Dalgarno, A. 1994, *ApJ*, 427, 1053
- Tenorio-Tagle, G. 1979, *A&A*, 71, 59
- van Dishoeck, E. F., & Black, J. H. 1986, *ApJS*, 62, 109
- 1988, *ApJ*, 334, 771
- 1989, *ApJ*, 340, 273
- Vázquez-Semadeni, E. 1994, *ApJ*, 423, 681
- Vázquez-Semadeni, E., Gazol, A., & Scalo, J. 2000, *ApJ*, 540, 271
- Velusamy, T., Langer, W. D., Pineda, J. L., Goldsmith, P. F., Li, D., & Yorke, H. W. 2010, *A&A*, 521, L18

- Wakker, B. P., & van Woerden, H. 1997, *ARA&A*, 35, 217
- Wallerstein, G., Vanture, A., & Jenkins, E. B. 1995, *ApJ*, 455, 590
- Weaver, R., McCray, R., Castor, J., Shapiro, P., & Moore, R. 1977, *ApJ*, 218, 377
- Weingartner, J. C., & Draine, B. T. 2001a, *ApJ*, 563, 842
- 2001b, *ApJS*, 134, 263
- Welty, D. E. 2007, *ApJ*, 668, 1012
- Welty, D. E., & Hobbs, L. M. 2001, *ApJS*, 133, 345
- Welty, D. E., Hobbs, L. M., Lauroesch, J. T., Morton, D. C., Spitzer, L., & York, D. G. 1999, *ApJS*, 124, 465
- Witt, A. N., & Johnson, M. W. 1973, *ApJ*, 181, 363
- Wolfe, A. M., Gawiser, E., & Prochaska, J. X. 2003a, *ApJ*, 593, 235
- Wolfe, A. M., Prochaska, J. X., & Gawiser, E. 2003b, *ApJ*, 593, 215
- Wolfire, M. G., Hollenbach, D., McKee, C. F., Tielens, A. G. G. M., & Bakes, E. L. O. 1995, *ApJ*, 443, 152
- Wolfire, M. G., McKee, C. F., Hollenbach, D., & Tielens, A. G. G. M. 2003, *ApJ*, 587, 278
- Woodgate, B. E. et al. 1998, *PASP*, 110, 1183